



GOI ESKOLA  
POLITEKNIKOA

ESCUELA  
POLITÉCNICA  
SUPERIOR

**THESIS**

Submitted for the degree of EUROPEAN DOCTOR  
in MONDRAGON UNIBERTSITATEA

TITLE

**Relationship between Solidification, Microstructures and  
Mechanical Properties of Magnesium Cast Alloys**

by

**Gurutze ARRUEBARRENA**

**PhD Director: Iñaki HURTADO**

**January 2009**









## **ACKNOWLEDGMENTS**



## ACKNOWLEDGMENTS / ESKERRAK

Eskerrak ematen hasi behar, eta nondik hasi asmatzea ez da erraza.

Jarraian agertzen diren erakunde eta pertsonen laguntzarik gabe ezinezkoa izanen litzateke lan hau burutzea.

Lehenik eta behin Iñaki Hurtadori eskerrak eman nahi nizkioke bere zuzendaritzarengatik, zabaldu dizkidan ateengatik eta urte guzti hauetan erakutsitakoarengatik. Mondragon Goi Eskola Politeknikoari eta Fabrikazio departamentuari (gaur egun Mekanika eta Ekoizpen Industriala deiturikoari) ere eskerrak eman nahi nizkieke, bereziki departamentuko buru den Angel Orunari, eta gaur egun ikerkuntza buru den Carlos Garcinari.

Jarraian, Eusko Jaurlaritzako Hezkuntza, Unibertsitate eta Ikerketa sailburuari ikertzaileak prestatzeko beka programaren bidez nire finantziazioa lau urtez bermatzeagatik. Bestetik, programa honetako beka aplikatzekoaz besteko zentroetan egonaldi laburrak egiteko emandako diru laguntzengatik, bai profesionalki zein pertsonalki garrantzi handikoak izan baitira nire formazioa burutzeko.

The research work for this thesis was carried out in an EU project on magnesium: IDEA (Integrated Design and Product Development for the Eco-efficient Production of Low-weight Aeroplane Equipment) Project Number: FP6-503826. As well as the European Community, I want to thank all the people collaborating in the IDEA project. Special thanks to Achim Wendt, whose help was essential for this work, thanks both professionally and personally. I also want to thank Konrad and Anne Weiss for their availability and the opportunity to work with them. Another important person in this work is Menachem Bamberger. He encouraged me in looking for new techniques and he opened me the doors of his laboratories, his home, and lots more. Thanks also to Shaul Avraham, Boris Bronfin, John Townsend, Sajid Mahmood, Jukka Väinölä, Sandor Dévényi, Andreas Dietz, Caroline Juers, Emmanuel Rocca, Sándor Lukács, Balázs Sándor, Annelore Schröder and the others.

The texture measurements by neutron diffraction were supported by the European Commission under the 6th Framework Programme through the Key Action: Strengthening the European Research Area, Research Infrastructures. Contract n°: RII3-CT-2003-505925. I thank all the people who made the measurements possible: Ulf Garbe, Uwe Wasmuth, Christian Randau, Peter Spalthoff, Bianca Tonin-Schebesta, Joana Rebelo and Michael Hofmann.

Thanks to the Technion Israel Institute in Haifa, Israel, for receiving me for 3 months in 2005. Special thanks to George Levi for the TEM images and to the team of Prof. Menachem Bamberger.

Another institute to thank is the Magnesium Characterization Department (Magnesium Wrought Alloys, WZW) in the Magnesium Innovation Centre, MagIC, in GKSS. Thanks to Achim for giving me the opportunity to join WZW and to Dietmar Letzig for receiving me. I need to give special thanks to Volker Kree for his help in the preparation of the samples and to Sangbong Yi for his accessibility. Thanks also to the whole WZW for everything I learned with you, and it is much, and for the nice time I had there.

I also want to thank the tribunal members and the reviewers.

Los resultados que se presentan en este documento también provienen de otros proyectos aparte del europeo: IDEA (Diputación Foral de Guipúzcoa 2004-2006); FORMAG y FORMAG II (Saiotek 2006-2007 y 2007-2008); MICROMAG (Profit 2007-2009); INVAUT (Manunet 2008-2010).

Alfa IDElri ere eskerrak eman behar dizkiet euren kolaborazioagatik. Bereziki Pedro Pablo Rodriguez, Miren Oyarbide eta Unai Andresi.

Mil gracias a Foseco y en especial Santi Vallejo por proporcionarme material para poner en marcha el laboratorio de fundición de MGEP.

Nola ez, MGEPeko konformaketa saileko guztiei ere milesker. Bereziki Rafa Ortubay, Iñaki Urrutia, Arkaitz Garate eta Gotzon Arrizabalagari, zuen laguntzarik gabe esperimentazioko atala ezingo bainuke aurrera eraman. Nirekin proiektuetan lanean aritu direnei ere eskerrak eman nahi dizkiet: Ibai Gomez, Xabier Arrieta, Jon Arriaran, Asier Gorosarri, Nuria Herrero eta Haritz Sarriegiri. Bestalde, materialen arloko arazoekin lagundu izan didaten Idoia Urrutibeaskoa eta Xabo Gomezi ere eskerrik asko.

Azken urte hauetan nire inguruan lanean izan ditudanei esker mila, momentu txar eta onetan lagundu didazuelako: Ibai Ulaciari, nire gaia ulertzen saiatu zarelako eta azken urteetan kontsultarako ezinbesteko izan zaitudalako; Eneko Saenz de Argandoña, Edurne Otxoa (aupa fundi!), Andrea Aginagalde, Joseba Pujana, Jon Ander Esnaola, Amaia Torregaray, Lander Galdos, Natxo Marquinez, Mikel Zubieta eta gainontzeko guztiei ere bai.

Amaieran doaz laguntzarik garrantzizkoenak. Urte guzti hauetan inguruan izan zaituztedan lagun eta familiako guztiak ezinbestekoak izan zarete aurrera jarraitzeko. Milesker beraz.

En el último sprint, por haberme animado y empujando para que terminara lo empezado cuando todo era cuesta arriba y porque ha conseguido que el camino haya sido menos duro, eskerrik asko Rodolfo.

Eta azkenik, nire bizitzan eta ondorioz lan honetarako ezinbestekoak izan direnak. Etxekoak; nola ez! **Milesker ama, aita, Jose Luis eta Karmele horren luze egin diren urte hauetan hor izan zaretelako egiten nuena ezin ulertuz baina hala ere ni aguantatuz! Hemen aurkezturiko guztia zuen fruitua ere bada.**

ESKERRIK ASKO GUZTIO!!!!!!!!!!!!!!

## **TABLE OF CONTENTS**



## TABLE OF CONTENTS

<b>1</b>	<b>INTRODUCTION.....</b>	<b>25</b>
1.1	Motivation.....	25
1.2	Objectives .....	27
1.3	Structure of the document.....	29
1.4	Main contributions of this study.....	30
<b>2</b>	<b>LITERATURE REVIEW .....</b>	<b>35</b>
2.1	Introduction of casting. General aspects .....	35
2.2	The solidification and microstructural evolution of magnesium alloys .....	36
2.2.1	Nucleation mechanisms.....	36
2.2.2	Growth morphology .....	38
2.2.3	Primary and secondary arm spacing .....	42
2.3	Alloying Systems.....	45
2.3.1	Metallurgical background of the Mg-Al alloys .....	45
2.3.2	Metallurgical background of Mg-Zn-Zr-Nd-Gd-Y alloys.....	47
2.4	Heat Treatment of Mg-Alloys .....	52
2.5	Correlation between mechanical properties and microstructure .....	53
2.6	Fracture mechanisms .....	56
2.7	Deformation modes and texture development in Mg-Alloys .....	58
2.7.1	Deformation modes in magnesium and its alloys.....	59
2.7.2	Description of the texture.....	60
2.7.3	Development of texture in magnesium .....	62
2.8	Summary.....	65
<b>3</b>	<b>EXPERIMENTAL PROCEDURE.....</b>	<b>69</b>
3.1	Casting technology.....	69
3.2	Selected alloys.....	70
3.3	Selected geometries .....	71
3.4	Acquisition of cooling curves.....	74
3.5	Heat treatment .....	75
3.6	Microstructural analysis .....	76
3.7	Texture Analysis Using Neutron Diffraction .....	77
3.7.1	The utility of neutrons .....	78
3.7.2	Lattice Strain Determination .....	78
3.7.3	Experimental Set-Up.....	79
3.8	Mechanical characterisation .....	81
3.8.1	Tensile testing.....	81
3.8.2	Hardness measurements.....	81
<b>4</b>	<b>CASTING AND SOLIDIFICATION OF MAGNESIUM ALLOYS.....</b>	<b>85</b>
4.1	Casting of gravity Mg-parts .....	85
4.1.1	Casting of Mg-parts in the foundries.....	86
4.1.2	Investment-casting of Mg-parts in MGEP .....	87
4.2	Cooling curves in gravity-cast parts.....	89

4.3	Casting of HPDC tensile bars .....	93
4.4	Summary and outlook .....	94
<b>5</b>	<b>MICROSTRUCTURAL EVOLUTION.....</b>	<b>97</b>
5.1	Identification of microstructures .....	97
5.1.1	Gravity cast microstructures .....	97
5.1.2	High-pressure die-cast microstructures .....	100
5.2	Analysis of fracture zones .....	102
5.3	Analysis of grain size distribution in gravity cast alloys .....	104
5.4	Analysis of porosity distribution.....	108
5.5	Microstructure and texture generation in HPDC alloys during tensile testing.....	108
5.6	Summary and conclusions.....	112
<b>6</b>	<b>ANALYSIS OF MECHANICAL PROPERTIES .....</b>	<b>117</b>
6.1	Mechanical characterisation of the tensile bars .....	118
6.2	Mechanical characterisation of the test parts .....	120
6.3	Hardness measurements .....	121
6.4	Summary and conclusions.....	123
<b>7</b>	<b>CORRELATIONS BETWEEN SOLIDIFICATION TIME, MICROSTRUCTURE AND MECHANICAL PROPERTIES .....</b>	<b>127</b>
7.1	Correlation between solidification curves and microstructures.....	128
7.2	Correlation between microstructures and mechanical properties.....	133
7.3	Correlation between solidification times and mechanical properties .....	136
7.4	Conclusions.....	137
<b>8</b>	<b>SUMMARY AND CONCLUSIONS .....</b>	<b>141</b>
<b>9</b>	<b>SCIENTIFIC CONTRIBUTION.....</b>	<b>147</b>
9.1	Publications in journals .....	147
9.2	Publications and presentations in conferences .....	147
<b>10</b>	<b>REFERENCES .....</b>	<b>153</b>



## LIST OF TABLES

Table 1.1. Alloys used in each technology.....	29
Table 2.1. Parameters relating secondary arm spacing and solidification rate (Eq. 2.4) for the magnesium AZ91 alloy.....	44
Table 2.2. Phases detected by XRD after different thermal treatments in the MRI207S alloy ( $\alpha$ -Mg excluded) [AVR07]. .....	51
Table 2.3. Basic temper designations [AVE99]. .....	53
Table 2.4. Hall-Petch coefficients for several Mg-alloys for determining tensile yield strength. ....	55
Table 2.5. Misorientations between the matrix and primary or secondary twins commonly observed in Mg [NAV04]. .....	60
Table 2.6. Summary of the selected equations. ....	66
Table 3.1. Alloys used in each technology.....	70
Table 3.2. Composition (%wt.) of the AZ91E, AZ91D and AM50A alloys [AVE99]. .....	71
Table 3.3. Summary of the gravity cast samples and the utilised nomenclature. ....	72
Table 3.4. Metallographic etchants used for Mg alloys. ....	77
Table 4.1. Solidification temperatures and times of the sand, investment and gravity die-cast AZ91E test-parts produced in the foundries (average values; PSFA, PIFA and PGFA). .....	92
Table 4.2. Solidification temperatures and times of the sand, investment and gravity die-cast MRI207S test-parts produced in the foundries (average values; PSFM, PIFM and PGFM). .....	92
Table 4.3. Solidification temperatures and times of the sand, investment and gravity die-cast AZ91E tensile bars and components produced in MGEP (TIMA and CIMA). .....	93
Table 5.1. Phases present in AZ91E and MRI207S alloys in as-cast and T6 conditions. ....	97
Table 5.2. Phases present in the AZ91D, AM50 and AM50+Si+Sn HPDC alloys. ....	101
Table 5.3. Grain size distribution for AZ91E and MRI207S alloys in as-cast and T6 condition in tensile bars. ....	105
Table 5.4. Grain size distribution for the AZ91E and MRI207S alloys in as-cast and T6 condition in the control points defined in Figure 5.14. ....	106
Table 5.5. Grain size for the AZ91E alloy in as-cast condition in the control points for the investment-cast parts produced in MGEP (TIMA and CIMA). .....	107
Table 5.6. Porosity distribution in the test parts. ....	108
Table 6.1. Required mechanical properties in separately cast specimens for aeronautic applications defined by IAI [WEN05]. .....	117
Table 6.2. Mechanical properties of the new alloys vs. commercial alloys of separately cast bars. ...	118
Table 6.3. Mechanical properties of the new alloys vs. commercial alloys of test parts. ....	120
Table 6.4. Description and values of the indentations in the AZ91E alloy. ....	122
Table 2.6. Equations employed for the prediction of grain size and tensile yield strength. ....	128
Table 7.1. Solidification time, cooling rate and grain size of the sand, investment and gravity die-cast AZ91E test-parts produced in the foundries (average values). .....	128
Table 7.2. Solidification temperatures and times of the investment-cast AZ91E tensile bars and components produced in MGEP. ....	129
Table 7.3. Solidification temperatures and times of the sand, investment and gravity die-cast MRI207S test-parts produced in the foundries (average values). .....	129
Table 7.4. Mechanical properties and measured microstructural parameters. ....	134

---

<i>Table 7.5. Comparison of calculated TYS using Hall-Petch relationships and data collected in the literature with the measured TYS.....</i>	<i>135</i>
<i>Table 7.6. Hall-Petch parameters for the 0.2% proof stress for the MRI207S alloy. ....</i>	<i>136</i>
<i>Table 7.7. Equations relating the solidification time with the tensile yield strength.....</i>	<i>137</i>

## LIST OF FIGURES

Figure 1.1. Diagram highlighting the steps of the overall work plan. ....	28
Figure 1.2. Chart describing the structure of the thesis. ....	30
Figure 2.1. a) Nucleation rate and b) nucleation time as a function of absolute temperature. $T_f$ is the temperature of fusion, $I_m$ the maximal nucleation rate and $t_m$ is the minimum time for nucleation to form a crystal. Line 1 represents a solidification time leading to a crystalline structure and an amorphous material will be the result with the solidification marked by line 2 [KUR98]. ....	38
Figure 2.2. Evolution of the solid-liquid interface morphology with increasing velocity. a) Planar interface generally observed in single-crystal growth; b) cellular structures; c) dendrites observed in classical metallurgical processes; d) flat interface obtained in rapid solidification [PFE07]. ....	39
Figure 2.3. Magnesium unit cell crystal with hexagonal close packed structure; a) atomic positions b) basal plane, a face plane and principal planes of the $[1\bar{2}10]$ zone; c) principal planes of the $[1\bar{1}00]$ zone; d) principal directions [AVE99]. ....	39
Figure 2.4. a) The mechanism of branching of the dendrites to establish the long-range arrangement of the structure along the basal plane; b) Essential feature of a columnar dendrite in the magnesium AZ91 alloy [PET89]. ....	40
Figure 2.5. Types of binary eutectic morphology, fibrous, lamellar, regular or irregular. a) fibrous and regular; b) lamellar and regular; c) fibrous and irregular; d) lamellar and irregular [KUR98]. ....	41
Figure 2.6. a) Micrograph of fully developed dendrites in a Mg-15wt% Al alloy permanent mould casting [STJ03]; b) representation of the hexagonal morphology [FER06]. ....	41
Figure 2.7. a) Columnar dendrites and their schematic representation as hexagonal packing of ellipses. Primary arm spacing ( $\lambda_1$ ) is indicated, in this case being equal to grain size (d) [PFE07]; b) Illustration of secondary arm spacing ( $\lambda_2$ ) and grain size (d). ....	42
Figure 2.8. a) SDAS as a function of the cooling rate for the AZ91 alloy compared with data from the literature [DUB98, LAB97, and SEQ97 in CAC02a]; b) Effect of cooling rate upon the dendrite arm spacing for AM50 and AZ91 [KAM87, TEN92]. ....	44
Figure 2.9. Measured temperatures of the AZ91E magnesium alloy at different points of the mould in a gravity die-casting example [WEN06]. ....	44
Figure 2.10. Schematic composition paths during Mg-Al non-equilibrium solidification [CAR97]. ....	46
Figure 2.11. a) Lamellar, b) fibrous, c) partially divorced and d) fully divorced morphologies in Mg-Al alloys of various compositions [STJ03]. ....	46
Figure 2.12. Optical micrographs of as-cast alloys at two magnifications each; a) and b) Mg-5Zn-0.6Zr (wt.%); c) and d) Mg-5Zn-1Nd-0.6Zr (wt.%); e) and f) Mg-5Zn-2Nd-0.6Zr (wt.%); g) and h) Mg-5Zn-2Nd-0.5Y-0.6Zr (wt.%); i) and j) Mg-5Zn-2Nd-1Y-0.6Zr (wt.%) [LI07]. ....	49
Figure 2.13. TEM BFI showing lamellar eutectic W phase observed in Mg-5Zn-2Nd-1Y-0.6Zr (wt.%) alloy [LI07]. ....	49
Figure 2.14. Schematic illustration of the strengthening mechanism of yttrium in Mg-3%Nd. a) Mg-3%Nd in as-cast condition; b) Mg-3%Nd-2%Y in as-cast condition; c) Mg-3%Nd-2%Y after T6 heat treatment (all numbers relates to wt.%) [AGH08]. ....	50
Figure 2.15. Mg-2.8Nd-0.6Zn-0.46Zr-0.29Gd (wt.%) microstructures; a) as-cast; b) solution treated [GIL04]. ....	50
Figure 2.16. Optical micrographs of Mg-3Nd-0.2Zn-0.4Zr (wt.%) alloy: a) as-cast and b) solution treated at 540°C for 6 h [PEN08]. ....	51
Figure 2.17. a) BSE micrograph of alloy MRI207S-F; b) BSE micrograph of MRI207S-F after thermal exposure at 200°C for 32 days [AVR07]. ....	52
Figure 2.18. Relation between grain size and ductility for pure magnesium [EML66, data taken from HER36, CHA62]. ....	54

Figure 2.19. A Mg-8%Al-4%Zn alloy solution treated for 30 hr. at 365°C, showing a premature fracture in the residual $\gamma$ -Al <sub>12</sub> Mg <sub>17</sub> phase away from the main fracture. This cracking tendency disappeared after precipitation [FOX45].	57
Figure 2.20. Cross section of a die-cast test plate of alloy AM60. The arrowheads show the fine grained surface [KOC03].	58
Figure 2.21. Relevant hexagonal close packed crystal planes for slip and twinning in magnesium [AGN05].	59
Figure 2.22. Two methods for representing the crystallographic orientation g: a) Miller indices; b) Euler angles; a coordinate system is presented as Z-axis and its X-Y plane for the sample; Z' and X'-Y' plane for the crystal [YI05].	61
Figure 2.23. Stereographic projection construction of a cubic material [ALU08].	62
Figure 2.24. Representation of a) random and b) preferred texture in the pole figure [ALU08].	62
Figure 2.25. Schematic rolling textures in HCP metals with c/a ratios are approximately equal to the ideal like Mg (c-type) [TEN80].	63
Figure 2.26. (0002) pole figure illustrating the macrotexture of the AM60 alloy after one rolling pass at 375°C with a 80% thickness reduction. r-type texture is observed [PER04b].	63
Figure 2.27. a) (0002) pole figure of the 0° tensile sample. FN is the original normal direction after cutting of the sample and FT is the transverse direction of the extruded bar. $P_{max}=5.7$ m.r.d.; b) the flow curve during tensile test, indicating the in-situ measuring points of the texture. c) variation of the (0002) pole figure during tension of the 0° sample. Level = 1.0, 1.5 ... 5.5 in all the pole figures [YI05].	64
Figure 2.28. $\{10\bar{1}0\}$ and (0002) pole figures for the a) undeformed; b) compression in the rolling direction, and; c) compression in transverse direction samples. [JAI07].	65
Figure 3.1. The CAD model of the crucible and the crucible constructed and placed in the furnace. .	70
Figure 3.2. Configuration of High-Pressure Die-Cast specimens.	70
Figure 3.3. Different geometries cast by sand-casting: a) tensile bars; b) test-part.	72
Figure 3.4. a) Tensile bar for HPDC; b) for gravity die-casting; and c) for investment-casting; d) machined sand-cast tensile sample.	73
Figure 3.5. CAD model of the test part.	74
Figure 3.6. CAD model of the prototype.	74
Figure 3.7. Positions for the thermocouples placed inside the test part.	75
Figure 3.8. Positions for the thermocouples placed in the investment-cast parts: a) placements in the mould for casting tensile bars; b) placement of the thermocouples in the mould of the prototypes.	75
Figure 3.9. Schematic of concept of neutron diffraction according to Bragg's law; a) 1 <sup>st</sup> order reflection: $\lambda = 2d \sin \theta_1$ ; b) 2 <sup>nd</sup> order reflection: $2\lambda = 2d \sin \theta_2$ ; 3 <sup>rd</sup> order reflection: $3\lambda = 2d \sin \theta_3$ [BRU08].	79
Figure 3.10. Representation of the Stress-Spec instrument at FRM-II [FRM08].	80
Figure 3.11. The set up in the Stress-Spec instrument at FRM-II.	80
Figure 3.12. Tensile bars cast in this work by HPDC, sand, investment and gravity die-casting.	81
Figure 3.13. Positions for excising tensile bars from the test part.	81
Figure 3.14. Microstructure of the AZ91E alloy showing two main phases: $\alpha$ -Mg and lamellar $\alpha$ -Mg and $\gamma$ -Al <sub>12</sub> Mg <sub>17</sub> (TSFA).	82
Figure 4.1. Magnesium parts cast in this work: a) tensile bars; b) test part; c) prototype.	85
Figure 4.2. Pouring of MRI207S to an investment casting mould (TIFM).	86
Figure 4.3. Small visible defect area in a test-part (PIFM).	86

Figure 4.4. Porosity and internal oxidation encountered in some investment-casting test parts after fracture (TIFA).....	87
Figure 4.5. a) Incomplete filling of the mould in the first trials with the old crucible; b) Complete filling of the mould with the new crucible (TIMA).....	87
Figure 4.6. a) Isolated oxides in aluminium oxide moulds; b) Oxides distributed in the longitudinal area of the sample in moulds made by colloidal silica.....	88
Figure 4.7. Long dendrite arms encountered when no grain refiner was used.....	88
Figure 4.8. Needles of the brittle phase $\gamma$ -Al <sub>12</sub> Mg <sub>17</sub> distributed in the microstructure.....	89
Figure 4.9. Measured cooling curves at the indicated points in the AZ91E sand-cast test part (PSFA).....	89
Figure 4.10. Measured cooling curves at the indicated points in the MRI207S sand-cast test part (PSFM).....	90
Figure 4.11. Measured cooling curves at the indicated points in the AZ91E investment-cast tensile bars at MGEP (TIMA).....	90
Figure 4.12. Measured cooling curves at the indicated points in the AZ91E investment-cast components at MGEP (CIMA).....	91
Figure 5.1. Optical microscopy of investment-cast a) AZ91E-F; and b) AZ91E-T6 (TSFA).....	98
Figure 5.2. SEM micrographs showing microstructure of a) sand-cast AZ91E-F; and b) sand-cast AZ91E-T6 (TSFA).....	99
Figure 5.3. Lamellar eutectic detail of sand-cast AZ91E-T6 alloy (TSFA).....	99
Figure 5.4. a) BSE micrograph of alloy MRI207S-F; b) BSE micrograph of MRI207S-F after thermal exposure at 200°C for 32 days [AVR07].....	100
Figure 5.5. Optical micrographs of a) MRI207S-F; and b) MRI207S-T6 (TSFM).....	100
Figure 5.6. Microstructures of a) AM50; b) AM50+Si+Sn.....	101
Figure 5.7. Intermetallics in grain boundaries of the alloy AM50+Si+Sn.....	101
Figure 5.8. Fracture surfaces of a) AZ91E-F; b) AZ91E-T6; c) MRI207S-F and d) MRI207S-T6 (TSFA and TSFM).....	102
Figure 5.9. Dimple fracture zone in alloy AM50+Si+Sn.....	103
Figure 5.10. Presence of porosity in the fracture surface of high-pressure die-cast alloys: a) gas porosity; b) microshrinkage (AM50 alloy).....	103
Figure 5.11. MgSi <sub>2</sub> intermetallics after deformation next to the fracture area.....	103
Figure 5.12. Microstructures of the alloys for grain size measurement; a) solubilised AZ91E (TSFA); similar microstructure for as-cast and heat-treat conditions after solubilisation); b) MRI207S-F (TSFM); c) MRI207-T6 (TSFM).....	104
Figure 5.13. Positions for grain size measurement in the test part.....	105
Figure 5.14. Grain size ( $\mu\text{m}$ ) distribution in the: a) sand-cast AZ91E-F alloy (PSFA); b) sand-cast AZ91E-T6 (PSFA); c) sand-cast MRI207-F (PSFM); d) investment-cast MRI207-T6 (PIFM).....	106
Figure 5.15. Inhomogeneous grain size distribution in the MRI207S sand-cast test part after T6 heat treatment.....	107
Figure 5.16. Pole figures for the diffraction peak $(10\bar{1}0)$ ; a) AM50 before testing; b) AM50+Si+Sn before testing; c) AM50 after tensile testing; d) AM50+Si+Sn after tensile testing. The loading direction is perpendicular to the pole figures.....	109
Figure 5.17. Engineering tensile curve of the alloy AM50A, showing the points of deformation where texture was measured.....	110
Figure 5.18. Pole figures for the diffraction peak $\{10\bar{1}0\}$ (Loading direction perpendicular).....	111

Figure 5.19. TEM images of the AM50+Si+Sn alloy; a) presence of piles up of dislocations and twins (strain rate of $1.5 \cdot 10^{-4} \text{ s}^{-1}$ ); b) subcells in the matrix (strain rate of $0.1 \text{ s}^{-1}$ ). .....	112
Figure 6.1. Proposed parts for substitution of aluminium components with magnesium in aircraft applications; a) pedals; b) housing [ARR07]. .....	117
Figure 6.2. Tensile curves in sand cast magnesium alloys compared to aluminium A357 alloy. ....	119
Figure 6.3. Porosity in the HPDC AM50 test part (Position S3). .....	121
Figure 6.4. Vickers indentation in different areas of the AZ91E alloy. ....	122
Figure 7.1. Diagram highlighting the steps of the overall work plan. ....	127
Figure 7.2. Correlation between cooling and grain size or secondary arm spacing for AZ91E. Values taken from literature and from this work show the same tendency. This study refers to grain size and literature [CAC02a, DUB98, SEQ97 and LAB97] refers to secondary arm spacing.....	131
Figure 7.3. Relationship between solidification time and grain size for AZ91E and MRI207S alloys. 132	
Figure 7.4. Relationship between solidification rate and grain size for AZ91E and MRI207S alloys.. 132	
Figure 7.5. The 0.2% proof stress (TYS) as a function of $d^{-1/2}$ for AZ91E and MRI207S alloys in as-cast and T6 conditions. Tendencies taken from literature [COU66 and SAS96 in CAC02a] are marked for AZ91E and tendency lines for MRI207S are illustrated. ....	136

## LIST OF SYMBOLS

$A$	elongation (%)
$Al_m$	residual amount of Al in solution
$Al_{ppt}$	the proportion of Al atoms
$B_r$	strengthening coefficient for random solid solution
$B_s$	strengthening coefficient of short range order (SRO)
$D$	diameter of the indenter
$D_l$	diffusion coefficient in liquid
$DAS$	dendrite arm spacing
$E$	Young's modulus
$F$	force applied by the indenter
$G$	interface temperature gradient ( $dT/dz$ ; K/m)
	ASTM grain size number
$HV$	Vickers pyramid number
$I$	nucleation rate
$T$	temperature
$T_{liquidus}$	liquidus temperature
$T_{solidus}$	solidus temperature
$\dot{T}$	cooling rate ( $^{\circ}C/s$ )
$Q$	growth restriction parameter
UTS	ultimate tensile strength (MPa)
$V_f$	volume fraction
$V_f^{\max}$	maximum volume fraction
TYS	tensile yield strength, in this work every time it is mentioned equals to the offset yield strength at a strain of 0.2% ( $e = 0.002$ ) (MPa)
$b$	Burgers vector
$c$	concentration of an element in the alloy
$c_0$	solute content in the alloy melt

$d$	measured grain diameter or grain size
	lattice plane spacing (neutron diffraction, Bragg's law)
	length left by the indenter (hardness measurements)
$f$	solute concentration
$g$	orientation of the crystals
$(hkl)$	Miller indices
$k$	equilibrium partition coefficient
	segregation coefficient ( $k=c_S/c_L$ )
$k_B$	Boltzmann's constant
$m$	Taylor factor
$n$	hardening exponent (determination of elongation)
	reflection order (neutron diffraction, Bragg's law)
$r^*$	critical nucleus size
$t$	time
$t_s$	solidification time
$\Delta G_d$	activation free energy for diffusion across solid/liquid interface
$\Delta G_n^o$	activation energy for the nucleation of a critical number of clustered atoms
$\Delta G_v$	the change of free energy per unit volume from liquid to solid; $\Delta G_v = \Delta G_v^L - \Delta G_v^S$
$\Delta G_v^L$	the free energy per unit volume of liquid
$\Delta G_v^S$	the free energy per unit volume of solid
$\Delta T'$	dendrite tip-to-root temperature difference
$\Delta T_o$	liquidus-solidus range at co
$\Delta T_s$	non-equilibrium temperature range of solidification ( $T_{liquidus} - T_{solidus}$ )
$\Gamma$	Gibbs-Thomson coefficient
$\alpha$	proportionality coefficient
	entropy of fusion
$\varepsilon$	plastic strain
$\gamma_{SL}$	solid/liquid interfacial free energy



---

$\varphi_1, \phi, \varphi_2$	Euler angles
$\lambda$	neutron wavelength (Bragg's law)
$\lambda_1$	primary arm spacing
$\lambda_2$	secondary arm spacing
$\mu$	shear modulus
$v_i$	interface velocity
$\theta$	half the diffraction angle
$\rho$	density of dislocations
$\sigma_o$	friction stress
$\sigma_y$	tensile yield strength (TYS)
$\tau_b$	critical resolved shear stress (CRSS) of the basal system
$\tau_o$	critical resolved shear stress (CRSS) of the basal system for pure Mg.
$\tau_p$	critical resolved shear stress (CRSS) of the prism slip system



**SUMMARY / RESUMEN / LABURPENA**



## SUMMARY

This thesis analyses the solidification, the microstructure and the mechanical properties of several magnesium alloys. The objective is to establish correlations between them in order to predict the local mechanical properties of magnesium cast components. On one hand, the solidification times have been related to the grain sizes and on the other, the grain sizes to the tensile yield strength, as for example, using the Hall-Petch equation. These relationships are integrated into numerical models for the prediction of the local mechanical properties in castings. Moreover, the effect of the alloying elements in the mechanical properties and in the generation of the texture in HPDC magnesium alloys after uniaxial deformation has been analysed.

This work is aimed at the aeronautic sector, specifically to substitute aluminium alloys in applications for the interior of commercial aircrafts. Four casting technologies and four alloys have been selected. The casting technologies are sand, investment, gravity die and high-pressure die-casting. Two of the selected alloys are commercial, the AZ91 and AM50 alloys. The commercial alloys are reference alloys for two new alloys. Three alloys, including the two commercial alloys, are based in the Mg-Al system. The fourth alloy is a higher strength magnesium alloy based in the Mg-Zn-Zr-Nd-Gd-Y system and designated as MRI207S.

This investigation is divided into three sections. The first task is the production of magnesium castings and the acquisition of cooling curves. A variety of alloys have been cast obtaining several microstructures and consequently, different mechanical properties.

The second section relates to the microstructural characterisation in as-cast and heat treated conditions. The applied heat treatment is the solution heat treatment and artificial aging (T6). In this section the precipitates of each alloy are identified, as well as the grain sizes in different areas and the fracture mechanisms. Precipitates increasing the strength are present in the new alloys. Moreover, texture generation in uniaxial deformation is analysed in order to investigate the effect of the alloying elements on the deformation mechanisms. The basal plane (0001) is oriented parallel to the loading direction. The obtained intensity is smaller than that obtained in wrought alloys. It has been concluded that the alloying elements have not affected the generation of the texture.

The third section involves the mechanical characterisation. Tensile tests have been carried out in order to obtain the ultimate tensile strength, the tensile yield strength and the elongation of the material. The properties of the MRI207S alloy are close to the ones of the A357 aluminium alloy. Vickers microhardness tests have also been performed to see the influence of the kind of precipitates in mechanical properties. The morphology of the precipitates in the AZ91E alloy varies in the same zone, and, therefore, varying the local mechanical properties.

Correlating the results obtained in these three sections, relationships between solidification time, grain size and tensile yield strength have been established for the new MRI207S gravity-cast alloy (cast by sand, investment and gravity die-casting).

## RESUMEN

La presente tesis analiza la solidificación, la microestructura y las propiedades mecánicas de varias aleaciones de magnesio con el fin de establecer correlaciones entre ellas y predecir las propiedades mecánicas locales en piezas fundidas. Se han relacionado los tiempos de solidificación con los tamaños de grano por un lado y por el otro los tamaños de grano con el límite elástico a tracción, como por ejemplo mediante la ecuación de Hall-Petch. Estas relaciones se integran en modelos numéricos para la predicción de propiedades mecánicas locales en piezas de fundición. Así mismo, se ha analizado el efecto de los aleantes en las propiedades mecánicas y en la generación de la textura de las aleaciones de magnesio inyectadas tras deformación uniaxial.

El trabajo realizado se enmarca dentro del sector aeronáutico, concretamente con el fin de sustituir aleaciones de aluminio para aplicaciones del interior de aviones comerciales. Se han seleccionado cuatro tecnologías de fundición y cuatro aleaciones. Las cuatro tecnologías son el moldeo en arena, la cera perdida, el moldeo en coquilla por gravedad y la inyección. Entre las aleaciones seleccionadas, dos son comerciales, siendo estas la AZ91 y la AM50. Las aleaciones comerciales se han utilizado como referencia para las dos nuevas aleaciones. Tres aleaciones, incluyendo las dos comerciales, se basan en el sistema Mg-Al. La cuarta aleación es una aleación de magnesio de mayor resistencia basada en el sistema Mg-Zn-Zr-Nd-Gd-Y y denominada MRI207S.

Se han distinguido tres fases principales. La primera fase consta de la producción de fundiciones de magnesio y la adquisición de curvas de enfriamiento. Se ha fundido una diversidad de aleaciones con varias microestructuras y por consiguiente, con diferentes propiedades mecánicas.

La segunda fase trata de la caracterización microestructural antes y después del tratamiento térmico. El tratamiento térmico empleado ha sido el de solubilizado, temple y envejecimiento artificial (T6). En esta fase se han identificado los precipitados presentes en cada aleación, los tamaños de grano en diferentes zonas y los mecanismos de fractura. En las nuevas aleaciones se han detectado varios precipitados que mejoran la resistencia. Así mismo, se ha analizado la evolución de la textura durante la deformación uniaxial para analizar el efecto de los elementos de aleación en los mecanismos de deformación. En la deformación, el plano basal (0001) se orienta paralela a la dirección de carga, siendo la intensidad obtenida menor que la obtenida en las aleaciones forjadas. Así mismo, se ha detectado que los aleantes no han afectado a la evolución de la textura.

La tercera fase es sobre la caracterización mecánica. Se han realizado ensayos de tracción para el establecimiento del límite a rotura, el límite elástico y el alargamiento. La aleación MRI207S muestra propiedades mecánicas cercanas a las de la aleación de aluminio A357 fundidas. También se han efectuado ensayos de microdureza para establecer la influencia que tiene el tipo de precipitado en las propiedades mecánicas. La morfología de los precipitados en el caso de la aleación AZ91E varía en una misma zona, variando así sus propiedades mecánicas locales.

Relacionando los resultados obtenidos en estas tres fases, se han establecido correlaciones entre el tiempo de solidificación, el tamaño de grano y el límite elástico para la nueva aleación MRI207S fundida por gravedad (moldeo en arena, a la cera perdida y en coquilla por gravedad).

## LABURPENA

Hemen aurkezten den tesi honek hainbat aleazioen solidotzea, mikroegitura eta ezaugarri mekanikoak aztertzen ditu. Helburua euren arteko erlazioak ezarri eta galdatutako piezen ezaugarri mekanikoak igartzea da. Batetik solidotze denborak ale tamainarekin erlazionatu dira, eta bestetik ale tamainak trakzioko elastikotasun mugarekin, Hall-Petch ekuazioaren bidez adibidez. Lorturiko ekuazioak zenbakizko modeloetan sar daitezke galdaketako piezen lekuko ezaugarri mekaniko iragartzeko. Aleazio elementuek ezaugarri mekanikoetan duten eragina ere aztertu da. Bestalde, injekziozko magnesio aleazioen testura sorkuntza deformazio uniaxialean ere aztertu da.

Lan hau sektore aeronautikoan kokatzen da, hegazkin komertzialen barne aplikazioetan aluminio aleazioak ordeztuko asmoarekin. Lau galdaketa teknologia eta lau aleazio aukeratu dira. Lau teknologiak hondarrezko moldekatzea, argizari galduzkoa, maskorrezkoa eta injekzioa dira. Aukeraturiko aleazioen artean, bi komertzialak dira, AZ91 eta AM50 hain zuzen ere. Aleazio komertzialak erreferentzia moduan erabili dira beste bi aleazio berrirantz. Hiru aleazio, tartean bi komertzialak, Mg-Al aleazio sisteman oinarriturik daude. Laugarren aleazioa erresistentzia handiagoko magnesio aleazio bat da, Mg-Zn-Zr-Nd-Gd-Y sisteman oinarritua eta MRI207S deiturikoa.

Hiru etapa nagusi bereizi dira. Lehenengoa magnesio piezen galdaketa eta hozketa kurben neurketan oinarriturik dago. Etapa honetan hainbat aleazio galdatu dira mikroegitura desberdinak eta ondorioz, ezaugarri mekaniko desberdinak lortzearen.

Bigarren etapa karakterizazio mikroegituralaz arduratzen da. Aleazio bakoitzean agerturiko prezipitatuak, ale tamainak eremu desberdinetan eta haustura mekanismoak aztertu dira. Aleazio berrietan, materialaren erresistentzia hobetzen duten prezipitatuak aurkitu dira. Bestalde, testuraren garapena aztertu da deformazio uniaxialean. Helburua aleazio elementuek deformazio mekanismoetan duten eragina aztertzea izan da. (0001) plano karga norabideari paralelo orientatzen da eta lorturiko intentsitatea forja aleazioetan emandakoa baino txikiagoa da. Aleazio elementuek testura sorreran eraginik izan ez dutela ere erakutsi da.

Hirugarren fasea karakterizazio mekanikoari buruzkoa da. Trakzio saiakuntzak egin dira aleazio desberdinen haustura erresistentzia, elastikotasun muga eta luzapena ezagutzeko asmoz. MRI207S aleazioak A357 aluminio aleazioaren pareko ezaugarri mekanikoak ditu. Honenbestez, aluminio aleazioak ordezkatzeko posibilitate handiak ditu aleazio honek. Mikrogogortasun neurketak ere egin dira AZ91 aleazioan prezipitatu motek ezaugarri mekanikoetan duen eragina jakiteko asmoz. Prezipitatuaren morfologia aldakorra da eremu jakin batean, eta ondorioz, lekuko ezaugarri mekanikoak ez dira konstanteak.

Hiru etapa hauetan lorturiko emaitzak batuz, solidotze denboraren, ale tamainaren eta elastikotasun mugaren arteko erlazioak garatu dira MRI207 aleazio berriarentzat hondarrezko moldekatzeaz, argizari galdukoaz edo maskorrezkoaz galdatzen den kasuetarako.





## **CHAPTER 1 - INTRODUCTION**



## 1 INTRODUCTION

In this chapter the motivation leading to this research work, the defined objectives and the structure of the document are presented. The purpose of this introduction is to justify the interest of this thesis from a research point of view as well as from its use in industrial applications. This work is developed analysing components made for aircrafts, but the results are also applicable generally. Nevertheless, in some parts of the thesis, aviation requirements are considered.

### 1.1 Motivation

Since the 70s, the automotive industry has been working on the lightening of the vehicle for the reduction of fuel consumption [CAR97]. Common steels and iron are being replaced by high strength steels, aluminium, magnesium and polymers. In contrast, it takes longer to introduce changes in the aircraft industry because of strict regulations. The number of tests to go through is high before any change in the design of the aircrafts takes place. Furthermore, the aircraft industry has not been really conscious of the problem of weight until recently. Nowadays, due to the application of fuel emission taxes and the increase of fuel price, the introduction of light weight materials becomes important.

The reduction of pollution caused by air traffic has been a key target in recent years. It has been reported by the Commission of the European Communities [COM05, COM06] that air transport accounts for 3% of the total CO<sub>2</sub> emissions in the European Union, but the expected growth is high. EU emissions from international aviation grew by 87% between 1990 and 2004. In addition, air traffic is forecasted to more than double between 2005 and 2020. With this increase in traffic, it is essential to reduce the emissions, for example, by means of improvement in engine efficiency or by lightening the aircrafts.

Magnesium is a candidate for substituting other materials for the reduction of weight. Magnesium is the lightest structural metal with a density of 1.8 g/cm<sup>3</sup> compared to 2.7 g/cm<sup>3</sup> of aluminium and it has a specific strength comparable to steel [KAI03]. Traditionally, magnesium alloys have been considered for the substitution of aluminium alloys, but their lightness together with their metallic nature makes them a suitable candidate to substitute plastic components as well.

Although in recent years the efforts in magnesium technology have been concentrated in the automotive industry, the properties of magnesium alloys are also favourable for the aerospace industry. Benedyk [BEN08] states that in World War II, magnesium was a common material in aircrafts, but corrosion problems have reduced its use in aerospace. Currently, new high purity alloys show improved corrosion resistance, but the requirements of the aerospace industry make further developments necessary. This need is increased because of the limited quantity of the available Mg-alloys.

Magnesium alloys show some limitations when achieving the higher mechanical properties required for aviation. First of all, there are too few magnesium alloys with property ranges covering the requirements of aeronautics. Hence, there is a lack of quantity. Secondly, there is a lack of

understanding of the behaviour and properties of magnesium alloys, especially with regard to the correlations between alloy composition, process parameters and properties of the final component. Therefore, there is a lack of material and process knowledge. The development of this knowledge will allow the prediction of the component behaviour in service. Finally, these measures together will provide the basis for increasing the use of magnesium in aircrafts in a substantial way.

Present running R&D projects will probably define the future applications of magnesium in the aerospace industry. The 6<sup>th</sup> European Framework Program had three magnesium related projects in Aeronautic Priority: IDEA, AEROMAG and MagForming [OST07]. The first one is related to the development of magnesium castings and the other two to wrought magnesium alloys. This research work has been developed in the frame of the IDEA project: "Integrated Design and Product Development for the Eco-efficient Production of Low-weight Aeroplane Equipment", contract no. AST3-CT-2003-503826. The final aim of the IDEA project has been to develop new magnesium cast alloys mainly oriented to the aircraft industry.

In order to validate newly developed alloys, mechanical and microstructural characterisation is necessary. In addition, it is interesting to know local mechanical properties for designing a cast component. The mechanical properties in a cast part are defined by the material itself and by the local solidification conditions. Simulation tools can be employed for the prediction of local solidification conditions, and therefore, for the prediction of local mechanical properties. This leads to the possibility of an optimised design of the components that fulfil the requirements.

Improved and verified knowledge will allow a sound formulation of relationships between solidification rate, microstructure and tensile yield strength of cast magnesium alloys. An accurate prediction of the local mechanical properties will result in an optimised design of the components. A good design also leads to the reduction of weight, with less extra material. Since the main interest of magnesium is the lightening of components, this work could lead to an increase in the use of magnesium castings in aircrafts.

For a specific alloy, the solidification conditions define the microstructure. For example, long solidification times mean large grain sizes and precipitates closer to equilibrium. The solidification conditions of a component are not the same in all zones, so the microstructures and the mechanical properties differ from one area to another.

There are only few publications focusing on the prediction of properties in cast magnesium alloys. Most of them are dedicated to the Mg-Al system, which is the most used alloying system. A new developed cast alloy based on the Mg-Zn-Zr-Nd-Y-Gd system is analysed in this work. This kind of alloy is used when higher mechanical properties and creep resistance are required. For the validation of the results commercial AZ91E (Mg-Al system) is used as reference alloy. Solidification parameters, microstructures and mechanical properties are evaluated for these two alloys and correlations are established.

A complementary work leading to a better understanding of the deformation and fracture behaviour of magnesium castings is also presented in the microstructural characterisation. The evolution of texture

during tensile testing has been measured for high-pressure die-cast (HPDC) Mg-alloys in this issue. Commercial AM50 and an alloy based on AM50 and modified with Si and Sn are analysed. Several mechanisms can be the reason for increasing the mechanical properties of the alloys. This investigation leads to a better understanding of the deformation modes and of the effect of the alloying elements in the texture. There are few research works related to the creation of texture in magnesium cast alloys, and this study is an contribution to this area.

## 1.2 Objectives

In order to overcome the before mentioned obstacles (lack of quantity and lack of process and material knowledge) to a higher use of magnesium components, the following objectives for this thesis were formulated:

- To develop exploitable new knowledge on the influence of casting conditions on the mechanical behaviour of cast magnesium components.
- To enable the numerical simulation to predict local properties of cast magnesium components by provision of alloy and process specific data.
- To analyse the influence of the alloy composition and the precipitated intermetallics in the mechanical properties of magnesium alloys.

The present study was carried out to contribute to the establishment of the relationship between solidification conditions, microstructures and mechanical properties of magnesium cast alloys. This task will enable the prediction of the mechanical behaviour of magnesium casting and the optimisation of the alloy as well.

The mechanical properties of an alloy are defined by the obtained microstructure during casting and posterior heat treatments. In cast components, the mechanical properties will be different in each area because the solidification conditions depend on the casting parameters and on the geometry of the mould. With the help of casting simulation tools, as for example WinCast<sup>®</sup>, MagmaSoft<sup>®</sup> and Procast<sup>®</sup>, local solidification times can be predicted. It is then essential to increase the accuracy of the prediction of the microstructure from a local solidification time. Precise correlations between microstructures and mechanical properties may also be obtained. This will be possible due to the correlations between microstructure and mechanical properties established in this work.

The correlations between microstructure and tensile yield strength (TYS) are usually achieved using the grain size for a certain alloy cast in a specific casting technology. Hall Petch relation is used to correlate the grain size to the TYS. The influence of precipitates and the deformation modes are integrated as constants, and these factors should be modified when the casting technology or the alloy are changed. The performance of a further step has been decided upon in order to reach a better understanding of the deformation mechanisms. In order to analyse the effect of the precipitates in the deformation mechanism, the texture generation during tensile testing has been measured.

According to these considerations, the work plan for this thesis is structured into three steps. Figure 1.1 summarises the defined work plan to reach the main objective. The procedure starts casting

several parts with four casting technologies to obtain a variety of microstructures. Once the solidification conditions and microstructures are analysed, they are correlated with mechanical properties.

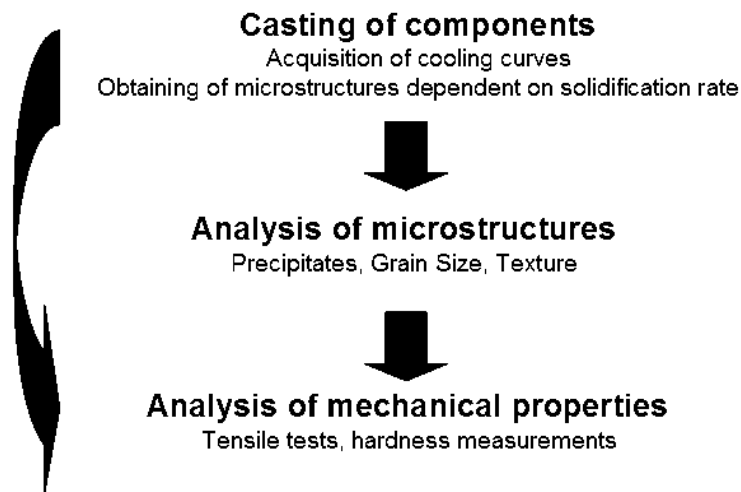


Figure 1.1. Diagram highlighting the steps of the overall work plan.

The three technical objectives represented in Figure 1.1 are detailed below:

1. **Casting of tensile samples and test parts. Acquisition of cooling curves.** This task allows us to obtain the samples for microstructural and mechanical characterisation. Furthermore, it leads to the obtainment of cooling curves at different points of the castings. The result is a variety of castings with different microstructures and mechanical properties with registered cooling curves.
2. **Microstructural characterisation.** Microstructures in as-cast and heat treated conditions are characterised by optical microscopy and SEM. Precipitates are identified. Grain sizes and porosity are measured to obtain a correlation between grain sizes and solidification curves. Fracture areas are also identified. The purpose is to define the effect of the alloy composition and the effect of precipitates in the fracture mode. Finally, for a better understanding of the deformability of Mg alloys, texture measurements are performed with the aim of defining the texture generation in uniaxially deformed magnesium castings. The effect of the alloying elements in the texture generation is analysed in this issue.
3. **Mechanical characterisation.** Tensile tests are carried out in separately cast tensile specimens and in specimens machined out from components. Mechanical properties are compared with microstructures. The final objective is to be able to predict the mechanical properties, especially the tensile yield strength, depending on cooling conditions. Hardness measurements on the other hand lead to the establishment of correlations between hardness and microstructures.

Three alloys from two families were chosen for this work and four casting technologies are used for the production of samples: three gravity casting technologies (gravity die-casting, investment-casting

and sand-casting) and high-pressure die-casting (HPDC). Table 1.1 summarises the alloys used in each technology. Three Mg-Al based alloys are used. AZ91 is used in each casting technology. AM50 and AM50+Si+Sn are only used in HPDC. MRI207S, a Mg-Zn-Zr-Nd-Gd-Y alloy, is only cast by gravity die-casting, investment-casting and sand-casting. At present, it is not possible to cast such alloys by HPDC due to their reduced castability.

*Table 1.1. Alloys used in each technology.*

<b>Technology</b>	<b>AZ91</b>	<b>AM50</b>	<b>AM50+Si+Sn</b>	<b>MRI207S</b>
<b>Sand-casting</b>	X			X
<b>Investment-casting</b>	X			X
<b>Gravity die-casting</b>	X			X
<b>HPDC</b>	X	X	X	

The results obtained from the tasks above lead to a better understanding of the effect of the precipitates and to the prediction of the tensile yield strength starting from the solidification conditions.

### **1.3 Structure of the document**

This work is divided into six chapters plus the introduction and conclusion.

The first chapter is a review which explains the theoretical basics and technological background. Firstly, an introduction to Mg castings is done. Next, the theory of solidification and alloying systems focused on the magnesium alloys of this study are discussed. Finally, heat treatments in magnesium, correlations between mechanical properties and microstructures and a short introduction to texture generation in Mg alloys are presented.

The second chapter is dedicated to the description of the adopted experimental procedure.

The third chapter describes the results of the casting trials and the acquisition of solidification curves. The results obtained in gravity die-casting, investment-casting, sand-casting and HPDC are shown. The difficulties and casting defects encountered during the casting of several parts, as well as the measured cooling curves are explained.

The fourth chapter is one of the main chapters of this work. First of all, it describes the microstructures obtained in each alloy in as-cast and heat treated conditions. Then, a short description of the fracture mechanisms is given, continuing with the grain size and porosity distribution in the castings. Finally, the texture generation of HPDC alloys during tensile testing is analysed using the neutron diffraction method.

The fifth chapter is dedicated to the mechanical testing of the separately cast tensile specimens and components. Hardness measurements of different phases in AZ91E alloy are also presented.

Finally, the sixth chapter puts together all the results obtained in the previous three chapters to apply correlations between them and to define the parameters that permit the prediction of the microstructures and mechanical properties from local solidification parameters.

Figure 1.2 shows a chart describing the structure of the thesis.

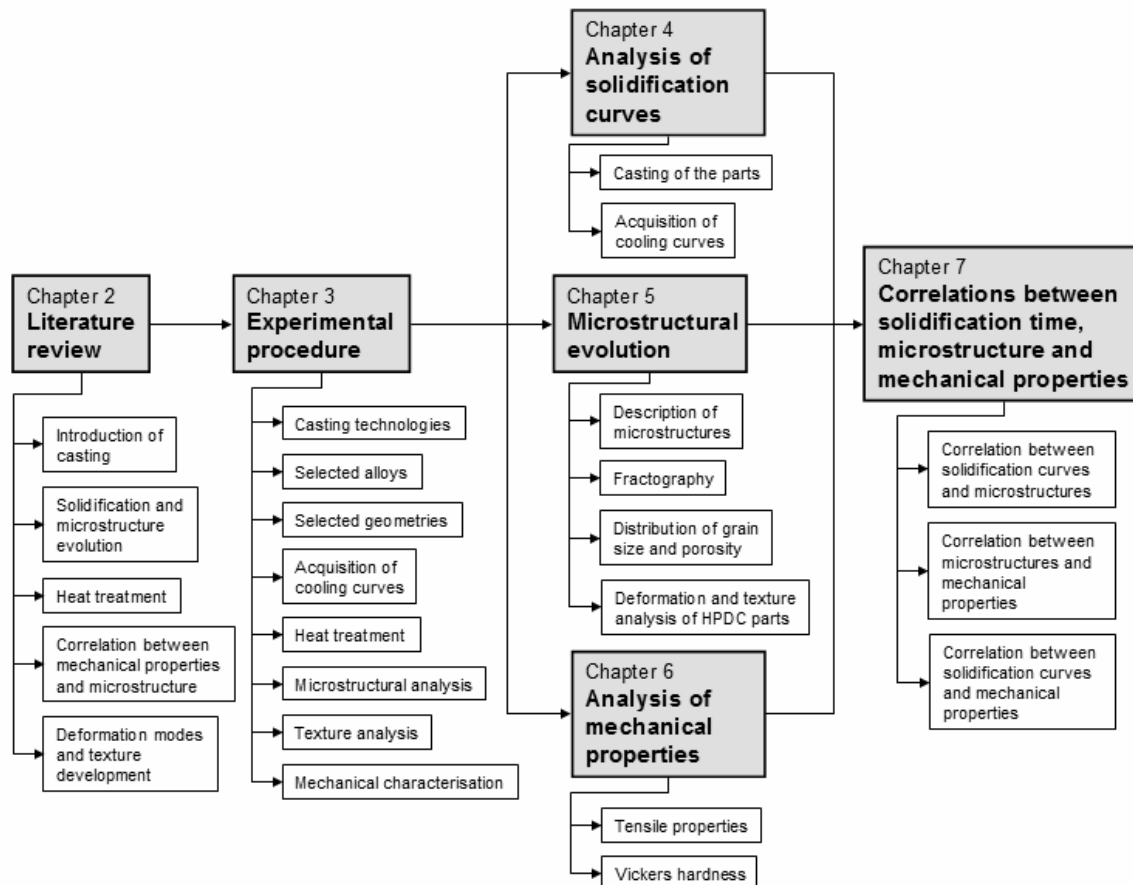


Figure 1.2. Chart describing the structure of the thesis.

#### 1.4 Main contributions of this study

The main results of this work are listed in this section.

The most important result is regarding the determination of mechanical and microstructural properties of two new magnesium alloys. In this work these properties are compared to commercial alloys. New alloys show promising results for future applications in commercial aircrafts. The new MRI207S alloy reaches the requirements established by Israel Aerospace Industries within the IDEA EC project for magnesium applications.

Moreover, this thesis is the first systematic investigation into new magnesium alloys for aeronautics that combines aspects of improved properties and component behaviour. The improved properties are achieved with the new alloys. On one hand, with the aim of increasing the knowledge about the newly developed magnesium alloys, the influence of precipitates and fracture mechanisms are described in as-cast and T6 heat treatment. On the other hand, the correlations between solidification times and microstructures for the new alloys are established to predict the component behaviour. Furthermore,



Hall-Petch parameters have been found for the first time for the gravity cast MRI207S alloy investigated in this work. Previously, only parameters for pure magnesium, for the Mg-Al system and for Mg-Zn binary alloys had been defined in literature.

Finally, for the first time, texture generation during uniaxial deformation is measured for magnesium high-pressure die-castings. Texture in high-pressure die-cast (HPDC) magnesium alloys is measured for a better understanding of deformation modes in different alloys. Neutron diffraction method is used for this task.



## **CHAPTER 2 - LITERATURE REVIEW**



## 2 LITERATURE REVIEW

In this chapter the literature review concerning the solidification of magnesium alloys, microstructure development and the relationship between microstructure and mechanical properties is presented.

First of all, the casting of magnesium is briefly introduced, giving an overview of the main factors to take into account when casting Mg.

Then, the microstructural evolution during solidification is explained. Nucleation events, morphology of the developed structure during solidification and methods for grain size calculation are discussed.

Subsequently, a review of the effect of alloying elements, the main intermetallics compounds in Mg alloys and the metallurgical background of the Mg-Al and Mg-Zn-Zr-Nd-Gd-Y alloys is presented. Typical heat treatments in Mg alloys are also mentioned.

Thereafter, different models for correlating microstructures with mechanical properties are discussed, focusing on the Hall-Petch equation. Fracture mechanisms are described for a better understanding of the effect of the alloying elements and grain size in the behaviour of the material.

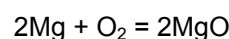
Finally, the literature review relating to the active deformation modes and the development of texture in polycrystalline magnesium and its alloys is presented.

### 2.1 Introduction of casting. General aspects

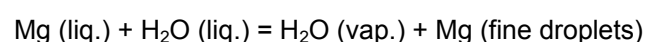
Magnesium alloys can be, in principle, cast by all known casting technologies. However, some precautions should be taken in comparison to other metals.

One of the mayor concerns in melting magnesium is its flammability. But in fact, magnesium only burns easily either in liquid state or in the form of powder or chips. For casting of Mg, Bach *et al.* [BAC04] recommend that the melting process should be performed under protective atmosphere or with the use of fluxes because of the high affinity to oxygen and the high vapour pressure of magnesium alloys. The more typically used protective methods are explained below in this section. When molten magnesium reacts with oxygen, a thin oxide layer is formed on the surface of the melt, but the oxide layer is porous and it is not sufficiently protective to prevent further oxidation [BAC04]. Hydro Magnesium [HYD06] summarises the exothermic reactions with oxygen and oxygen-containing materials as follows:

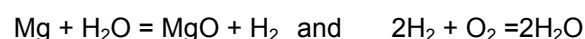
Burning/Oxidation



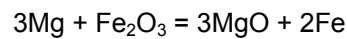
Rapid evaporation (expansion) of water entrapped by liquid magnesium



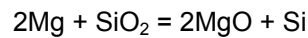
Water reaction/Hydrogen explosion



Thermite reaction



Silica reaction



Fluxes were traditionally used for alloys containing aluminium or manganese. Emley [EML66] gives the compositions of the typical fluxes. They are mainly composed of  $\text{MgCl}_2$ ,  $\text{CaCl}_2$ ,  $\text{NaCl}$ ,  $\text{KCl}$  and  $\text{BaCl}_2$ . The proper use of fluxes leads to good quality castings. Nevertheless flux can cause melt loss, inclusions, and flux disposal problems for example [ASM88], so fluxless melting was developed.

For fluxless melting protective gases has to be used. The first protective gas mixtures used contained sulphur dioxide ( $\text{SO}_2$ ) [ASM88], but due to its toxicity, in the 70s, mixtures of sulphur hexafluoride ( $\text{SF}_6$ ) became more common [CAS04]. This is a colourless, odourless and non-toxic gas, but since its greenhouse effect was discovered, alternatives to this gas are being analysed. It can trap heat in the atmosphere 23,900 times more effectively than  $\text{CO}_2$  [EPA06]. Nowadays, there are alternatives to  $\text{SO}_2$  and  $\text{SF}_6$ . Some examples are the HFC-134a gas and the Magshield system. Cashion *et al.* [CAS04] present the HFC-134a hydrofluorocarbon gas 1,1,1,2-tetrafluoroethane. They say that it releases the fluorine more readily than  $\text{SF}_6$ , being more efficient for melt protection than  $\text{SF}_6$  at typical molten metal temperatures. Revankar *et al.* [REV08] introduce the Magshield system, which work with the decomposition of  $\text{KBF}_4$  to obtain  $\text{BF}_3$ .

There are other precautions to be taken when melting magnesium. Molten magnesium reacts with water. Therefore, the ingots and tools, such as ladles, should be preheated to  $150^\circ\text{C}$  before placing them into molten Mg [HYD06]. Finally, silica crucibles should not be used due to their reaction with molten magnesium. Steel crucibles should be used instead [ASM88, AVE99, EML66, HYD06], as they are usually made of plain steel or nickel-free low alloyed steels.

## 2.2 The solidification and microstructural evolution of magnesium alloys

The key solidification processes that control the final microstructure are the initial nucleation events, the growth of these nuclei into primary dendrites and the eutectic solidification. Therefore, smaller grains can be achieved with the use of artificial nucleants or by elevated solidification rates. In this section, the nucleation mechanisms, the growth morphology and the obtained grain size are described.

### 2.2.1 Nucleation mechanisms

Solidification starts when the free energy of the liquid is higher than the free energy of the solid. This can, for example, be achieved by a decrease in temperature. The solid phase of metals is usually crystallographic and the liquid phase is non-crystallographic. For the change from liquid to solid, it is necessary to form stable regions of the solid phase. This becomes possible due to the nucleation of small clusters of ordered crystals in the melt. A minimum radius of the clusters is required to form a stable nucleus, smaller clusters being unstable. Kurz [KUR98] states that the smaller the difference

between the melting point and the temperature of the melt (undercooling), the larger the size of the equilibrium crystal will be. The equilibrium crystal is the stable generated cluster which will not melt.

The critical nucleus size to form stable clusters is given by Eq. 2.1 [POR81]

$$r^* = \frac{2\gamma_{SL}}{\Delta G_v} \quad \text{Eq. 2.1}$$

where  $r^*$  is the critical nucleus size,  $\gamma_{SL}$  the solid/liquid interfacial free energy and  $\Delta G_v$ , the change of free energy per unit volume from liquid to solid.

On the other hand, the rate of nucleus formation is given by Eq. 2.2 [KUR98],

$$I = I_o \exp\left[-\frac{\Delta G_n^o + \Delta G_d}{k_B T}\right] \quad \text{Eq. 2.2}$$

where  $I$  is the number of nuclei created per unit volume and time,  $I_o$  a pre-exponential factor,  $\Delta G_n^o$  the activation energy for the nucleation of a critical number of clustered atoms forming an stable nucleus,  $\Delta G_d$  the activation free energy for diffusion across the solid/liquid interface,  $k_B$  the Boltzmann's constant and  $T$  the temperature.

The maximum value of  $\Delta G_n^o$  varies with  $1/\Delta T$ .  $\Delta T$  is the undercooling of the material where the solidification starts. Therefore, the number of clusters depends on the undercooling of the material. There is a maximum in the nucleation rate at a critical temperature. This maximum is situated between the melting point ( $\Delta T = 0$ ) and the point where there is no longer any thermal activation ( $T=0$ ). This is illustrated in Figure 2.1a [KUR98]. At low undercoolings, the energy barrier for nucleus formation is very high and the nucleation rate is very low. As the undercooling increases, the nucleus formation rate increases before again decreasing due to a lower rate of atomic migration (diffusion) with decreasing temperature. Therefore, the result is a maximum in the nucleation rate. Figure 2.1b is plotted in a TTT (time-temperature-transformation) diagram, which gives the time required for nucleation. This time is inversely proportional to the nucleation rate, and, therefore, the inverse of diagram a) for a given alloy volume. When usual cooling rates are applied, a crystalline structure is obtained, but for very high cooling rates, an amorphous solid is the result via a continuous increase in viscosity.

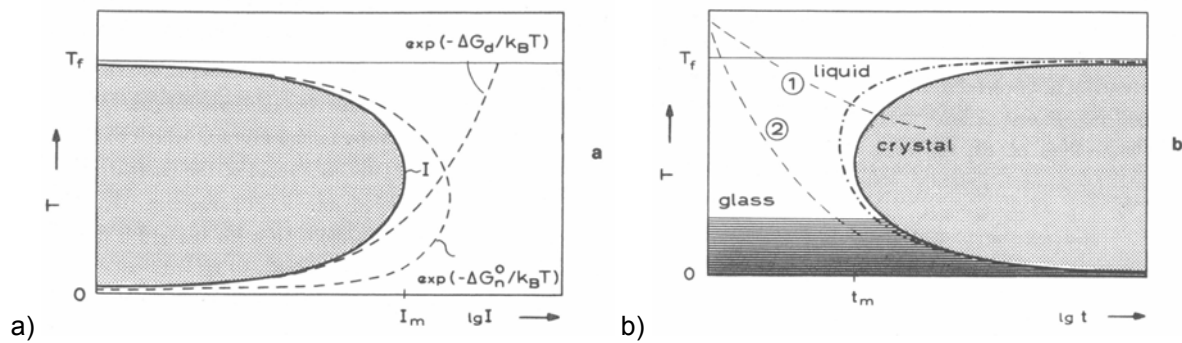


Figure 2.1. a) Nucleation rate and b) nucleation time as a function of absolute temperature.  $T_f$  is the temperature of fusion,  $I_m$  the maximal nucleation rate and  $t_m$  is the minimum time for nucleation to form a crystal. Line 1 represents a solidification time leading to a crystalline structure and an amorphous material will be the result with the solidification marked by line 2 [KUR98].

The value of  $\Delta G_n^0$  and, therefore, of the nucleation rate can be increased by adding foreign crystalline materials or by increasing the undercooling [KUR98]. The most effective nucleating agent for grain size reduction in magnesium is Zr. Nevertheless, the presence of elements such as Al and Mn dramatically reduces the liquid solubility of Zr, eliminating its grain refining effect in common Mg-Al alloys [AGH04]. Other grain refining methods used in Mg alloys are increased cooling rates, superheating, carbon or Sr additions, the addition of ferric chloride (Elfinal process) and agitation [EML66, LEE00, WAL03].

The initial nucleation is an important factor in determining final grain size. Difficulty arises when giving values to Eq. 2.2. For example,  $\Delta G_n^0$  is not constant for an alloy as previously explained, and it changes with artificial agents and undercooling. In practice, equations based on the growth mechanisms are used for the prediction of the microstructure in casting simulation models.

### 2.2.2 Growth morphology

The solidification of a liquid in metals can lead to different structures depending on the cooling rate, from a planar structure to a cellular one, then to a dendritic structure and finally to the rapid solidification structure. Figure 2.2 shows how the morphology changes when the solidification rate increases. Planar interface is then obtained when high thermal gradients are present. When reducing the thermal gradient, first protrusions will be generated and solute will be rejected laterally and piled up at the root of the protrusion. This will cause the lowering of the equilibrium solidification and eventually the protrusions develop into long arms or cells growing parallel to the direction of heat flow. Next comes the dendritic structure. It is the most common structure for all metallurgical processes. Porter and Easterling [POR81] explain that it is not fully understood why cells become dendrites. They say that it is probably associated with the creation of constitutional supercooling in the liquid between the cells causing interface instabilities in the transverse direction. Finally, rapid solidification is used to obtain very small microstructures and amorphous material [PFE07].



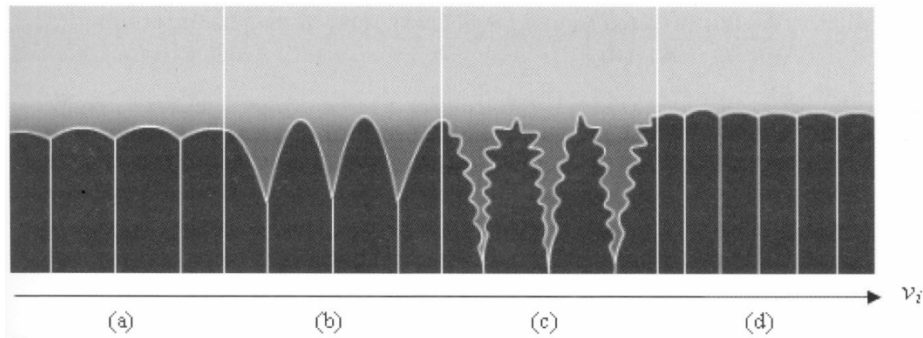


Figure 2.2. Evolution of the solid-liquid interface morphology with increasing velocity. a) Planar interface generally observed in single-crystal growth; b) cellular structures; c) dendrites observed in classical metallurgical processes; d) flat interface obtained in rapid solidification [PFE07].

Figure 2.3 introduces the main planes and directions present in hexagonal materials for the explanation of the principal direction of the dendritic growth in magnesium.

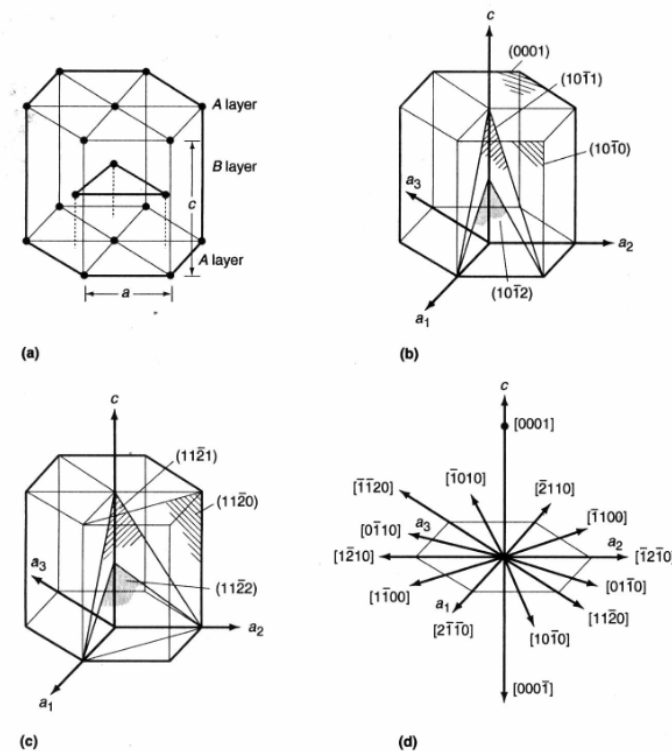


Figure 2.3. Magnesium unit cell crystal with hexagonal close packed structure; a) atomic positions b) basal plane, a face plane and principal planes of the  $[1\bar{2}10]$  zone; c) principal planes of the  $[1\bar{1}00]$  zone; d) principal directions [AVE99].

It is usually accepted that the  $\langle 10\bar{1}0 \rangle$  direction is the one for dendrite growth in hexagonal materials such as Mg [CHA54, CHA64, FLE74, REE64], although this has been established only for high purity Zn [WEI52]. Other directions have been reported for non-metallic materials, as the  $\langle 0001 \rangle$  direction for  $\text{Co}_{17}\text{Sm}_{12}$  [KUR98]. The general principle for faceted materials is that the direction of dendritic growth is the axis of a pyramid whose sides are the closest packed planes with which a pyramid can be formed [FLE74, CHA54, CHA64]. This is based on Bravais's law, which states that the directions normal to the most closely packed planes are the slowest growing directions [PET90]. Magnesium

crystals grown from the vapour form faces which are parallel to the  $(0001)$ ,  $\{10\bar{1}0\}$  and  $\{10\bar{1}1\}$  planes [STR35, VAN71].

Pettersen *et al.* [PET89, PET90] analyse the growth directions of the dendrites of magnesium alloy AZ91. In a first study [PET89], they conclude that the main growth direction was the  $\langle 11\bar{2}0 \rangle$ , with six secondary arms around the primary dendrite stalk. Two lie in the basal plane and four in  $(10\bar{1}1)$ -type planes (Figure 2.4). In a later article [PET90], they find that for a high temperature gradient to growth velocity ratio, the stem direction is  $\langle 22\bar{4}5 \rangle$  and secondary arms grow in three directions from the stem; two arms grow in the  $\langle 22\bar{4}5 \rangle$  directions at  $35^\circ$  from the stem direction, while the third arm grows in the  $\langle 11\bar{2}0 \rangle$  direction, at  $54^\circ$  from the stem direction. For a lower gradient to velocity ratio, the stem direction is  $\langle 11\bar{2}0 \rangle$ . Secondary arms are growing in six directions from the stem, two  $\langle 11\bar{2}0 \rangle$  directions at  $60^\circ$  from the stem direction and four  $\langle 22\bar{4}5 \rangle$  directions at  $73^\circ$ .

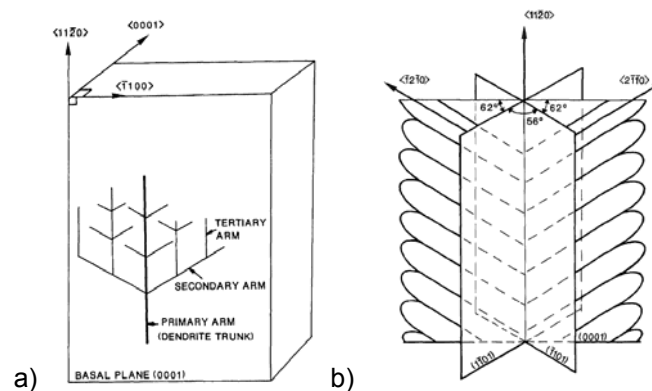


Figure 2.4. a) The mechanism of branching of the dendrites to establish the long-range arrangement of the structure along the basal plane; b) Essential feature of a columnar dendrite in the magnesium AZ91 alloy [PET89].

However, when more than one phase is being generated simultaneously in the transition from liquid to solid, eutectic structures will be obtained as well as the monophasic structures explained above. When solidifying in dendritic structures, solute elements are rejected into the liquid. Therefore, the concentration of solid and liquid phases is not the same, and segregation occurs. The liquid can also reach the eutectic composition, and eutectic phases can form in the grain boundaries and/or between dendrite branches.

A high variety of eutectic structures can be created. The most common eutectic structures are composed of two phases, which can be regular or irregular (Figure 2.5). When there is a high volume of both phases ( $0.25 < f < 0.5$ , where  $f$  is the solute concentration) the eutectic tends to be lamellar. For small concentrations of a phase ( $f < 0.25$ ), there is a tendency to form fibres of that phase [KUR98]. Furthermore, these structures can be regular or irregular, being regular when both phases have a low entropy of fusion ( $\alpha < 2$ , where  $\alpha$  is the entropy of fusion of the phases).

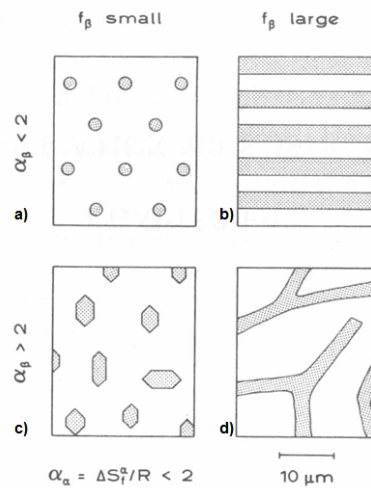


Figure 2.5. Types of binary eutectic morphology, fibrous, lamellar, regular or irregular. a) fibrous and regular; b) lamellar and regular; c) fibrous and irregular; d) lamellar and irregular [KUR98].

The growth of magnesium dendrites occurs according to the usual principles of primary phase solidification: solute elements with a distribution coefficient less than unity are rejected in front of the dendrites during growth and this causes changes in the microstructure. For example, a small addition of aluminium to pure magnesium leads to a morphological change of the primary phase. It changes from a cellular to a dendritic structure [STJ03].

Figure 2.6 shows a typical dendrite in Mg-Al alloys. It has a six-fold symmetry as explained in Figure 2.4. In this figure, A shows secondary arms of magnesium dendrites, B is the  $\gamma\text{-Al}_{12}\text{Mg}_{17}$  phase and C shows the  $\alpha\text{-Mg}$  solid solution rich in aluminium.  $\gamma\text{-Al}_{12}\text{Mg}_{17}$  equilibrium phase precipitates in Mg-Al alloys in interdendritic spaces. It is a hard phase suitable for increasing strength at room temperature. Nevertheless, it is not suitable because it reduces ductility and creep resistance significantly.

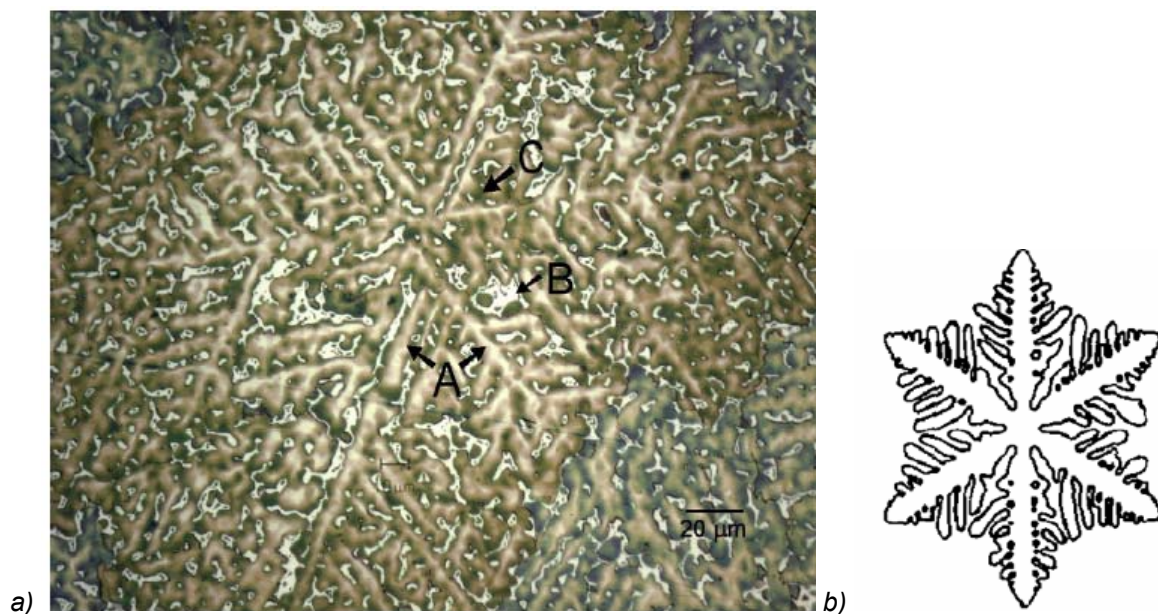


Figure 2.6. a) Micrograph of fully developed dendrites in a Mg-15wt% Al alloy permanent mould casting [STJ03]; b) representation of the hexagonal morphology [FER06].

### 2.2.3 Primary and secondary arm spacing

Firstly, definitions of grain size ( $d$ ), primary arm spacing ( $\lambda_1$ ) and secondary arm spacing ( $\lambda_2$ ) are given for metallic materials to clarify each concept and to avoid misunderstandings.

Grain size is equal to the diameter of a grain. A grain is the domain of solid-state matter that has the same structure as a single crystal. In a grain, the atoms are arranged in an orderly repeating pattern extending to all three spatial dimensions and it constitutes a single phase. However, grains are not always spherical and not every grain is the same size. Furthermore, average values are usually given. Besides, if the size depends on the direction, for example in wrought materials or directional solidification, grain size is given for each direction.

When dendritic structure is present, apart from grain size, primary and secondary arm spacing can be defined. Primary arm spacing is the distance between two adjacent primary dendrite arms. In columnar grains, for example, primary arm spacing and grain size is usually equivalent to the direction perpendicular to the trunk. Secondary arm spacing is similar, but in this case, it is the distance between the centers of two adjacent secondary dendrite arms.

Kurz and Fischer [KUR98] report that the dendrite arm spacing is defined by the solidification time, which is the time needed to go from liquidus to solidus temperature. The primary spacing develops during nucleation and is fixed during growth. It is directly related to the grain size. However, the secondary spacing can increase with long contact times between the highly-curved, branched structure and the melt. Once nucleation events are completed, growth continues until the primary dendrite arms meet the diffusion boundary of the neighbouring branches, at which point the grain size is fixed. The remaining time is left for the thickening of the secondary arms. This occurs by diffusion along the surface of the cylindrical arms as a result of a concentration gradient. The thin arms will be in a liquid high in solvent. Thus, the thin arms will dissolve as a result of diffusion of the solvent along the surface to the thicker arms as shown for Al-4.5% Cu by Kattamis [KAT67].

For a better understanding of the three definitions given above,  $d$ ,  $\lambda_1$  and  $\lambda_2$  are represented in Figure 2.7.

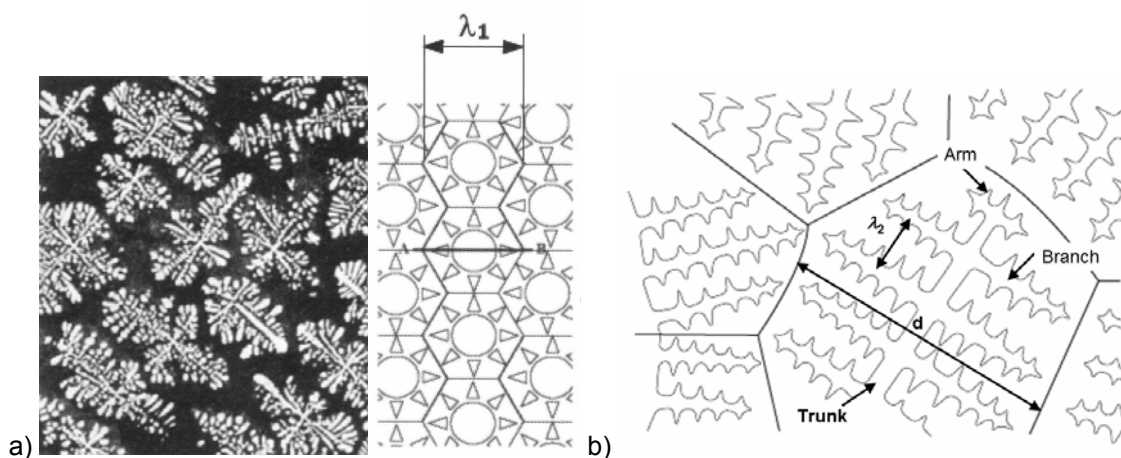


Figure 2.7. a) Columnar dendrites and their schematic representation as hexagonal packing of ellipses. Primary arm spacing ( $\lambda_1$ ) is indicated, in this case being equal to grain size ( $d$ ) [PFE07]; b) Illustration of secondary arm spacing ( $\lambda_2$ ) and grain size ( $d$ ).

Kurz [KUR98] computes the characteristic dimensions of the dendrites for the most important range of dendritic growth at commonly used parameters. The primary dendrite spacing or the periodicity,  $\lambda_1$ , (Figure 2.7) is given by Eq. 2.3. In this equation it is assumed that the dendrite tip-to-root temperature is similar to the liquidus-solidus range, so,  $\Delta T \cong \Delta T_o$ .

$$\lambda_1 = \frac{4.3}{\sqrt{G}} \sqrt[4]{\frac{\Delta T_o D_l \Gamma}{k v_i}} \quad \text{Eq. 2.3}$$

$\lambda_1$  is the primary arm spacing,  $G$  is the interface temperature gradient,  $\Delta T_o$  is the liquidus-solidus range at a solute concentration  $c_o$ ,  $D_l$  is the diffusion coefficient of the solute in liquid,  $\Gamma$  is the Gibbs-Thomson coefficient,  $k$  is the segregation coefficient ( $k=c_S/c_L$ ) and  $v_i$  is the interface velocity. Similar equations are also given for secondary arm spacing by Kurz [KUR98] or by Pfeiler [PFE07]. Nevertheless, all these equations are difficult to use due to the high amount of variables to be taken into account. In the commonly used multicomponent alloying systems, the usage of these equations becomes even more complicated.

Kurz [KUR98] states that dendrite arm spacing will not obey the simple relationship which is often proposed, as for example, by Flemings [FLE74] (Eq. 2.4). However, even if this equation is very simplified, it is useful due to its ease of application. Regarding Mg alloys, it allows an easy way to relate the microstructure with the cooling curves as reported by Caceres [CAC02a] and Wendt [WEN06].

$$d = a \cdot t_s^n = b \left( \frac{\Delta T_s}{t_s} \right)^{-n} \quad \text{Eq. 2.4}$$

In this equation  $d$  can represent either the dendrite arm spacing or the grain size.  $a$  and  $b$  are constants to be defined for each alloy and  $n$  is an exponent. Flemings [FLE74] reports without any explanation that the exponent  $n$  is in the range of  $\frac{1}{3}$  and  $\frac{1}{2}$  and generally very close to  $\frac{1}{2}$  for primary spacing.  $t_s$  is the solidification time and  $\Delta T_s$  is the non-equilibrium temperature range of solidification.

The relationship between  $\Delta T_s$  and  $t_s$  is defined by the solidification rate or the cooling rate  $\left( \left| \dot{T} \right| \right)$  in the next equation (Eq. 2.5).

$$\left| \dot{T} \right| = \frac{\Delta T_s}{t_s} = \frac{(T_{liquidus} - T_{solidus})}{t_s} \quad \text{Eq. 2.5}$$

$T_{liquidus}$  is the liquidus temperature and  $T_{solidus}$  the solidus temperature.

Caceres *et al.* [CAC02a] make an analysis of this relationship for AZ91E alloy and compared their data with data taken from the literature [DUB98, LAB97, SEQ97]. Values for  $b$  and  $n$  (Eq. 2.4) are given in Table 2.1 for the calculation of secondary arm spacing. Those values are also represented in Figure 2.8a. Kamado *et al.* [KAM87] and Tensi and Rosch [TEN92] also analyse the effect of the cooling rate in the dendrite arm spacing for two Mg-Al alloys (Figure 2.8b).

Table 2.1. Parameters relating secondary arm spacing and solidification rate (Eq. 2.4) for the magnesium AZ91 alloy.

	<i>b</i>	<i>n</i>
[CAC02a]	49.0	0.42
[LAB97]	49.9	0.34
[DUB98]	35.5	0.31
[SEQ97]	63.6	0.37

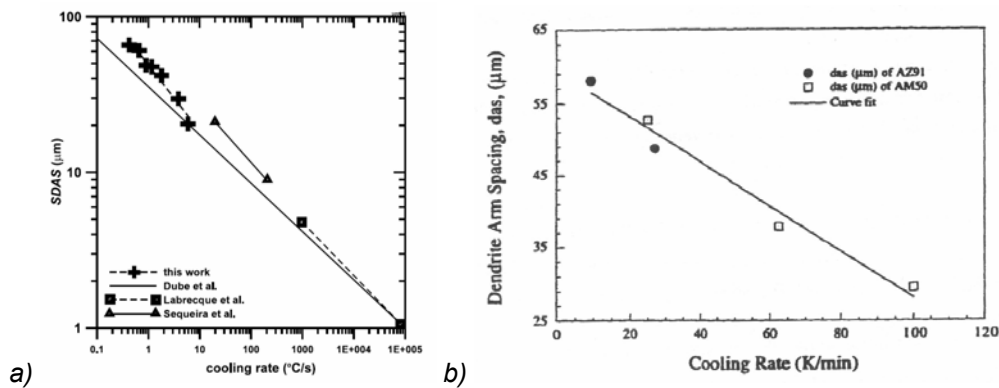


Figure 2.8. a) SDAS as a function of the cooling rate for the AZ91 alloy compared with data from the literature [DUB98, LAB97, and SEQ97 in CAC02a]; b) Effect of cooling rate upon the dendrite arm spacing for AM50 and AZ91 [KAM87, TEN92].

It is necessary to measure the solidification time to solve the Eq. 2.4. One way of determining  $t_s$  is to use sensorised moulds with thermocouples placed inside. The temperature is continuously measured during the solidification process at different positions by the thermocouples using a data acquisition software. Curves like the one shown in Figure 2.9 are obtained by this method. The solidification time can be calculated by the changes in the slopes of the curve at the beginning and at the end of the solidification (second derivative).

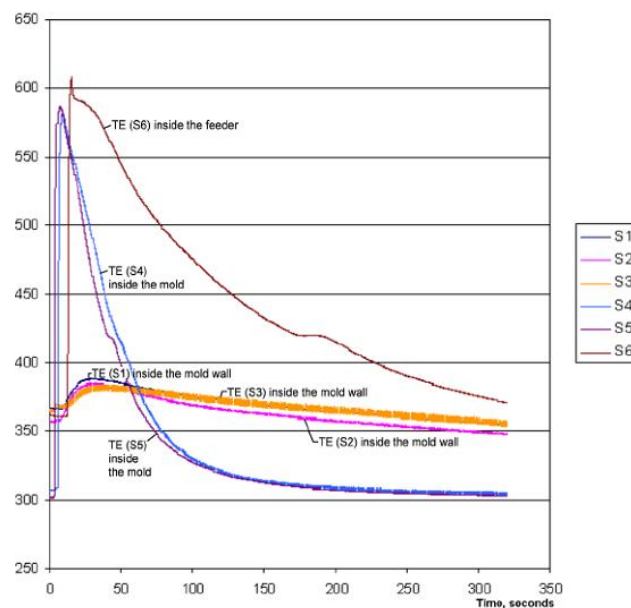


Figure 2.9. Measured temperatures of the AZ91E magnesium alloy at different points of the mould in a gravity die-casting example [WEN06].

## 2.3 Alloying Systems

Magnesium is available commercially with purity exceeding 99.8%. Nevertheless, it is rarely used for engineering applications without being alloyed with other metals due to poor mechanical properties. Key features that dominate the physical metallurgy of magnesium alloys are the hexagonal lattice structure and the fact that the atomic diameter of magnesium (0.320 nm) is such that it has a favourable size factor with a diverse range of solute elements [AVE99].

Atomic-size and valency restrictions, as well as the electropositive nature of magnesium, must be considered in alloying. In this section, the effects of alloying elements and the characteristics of two alloying systems are presented. The Mg-Al and Mg-RE-Zn-Zr systems are the ones analysed in this study. This section is an introduction of the characteristics of these alloys.

The most used alloying system is the Mg-Al-Zn system. The reason for this is the good castability and mechanical properties at room temperature of the alloys of the Mg-Al system in addition to their low cost. Mn additions are common in this alloying system to increase ductility. In order to obtain high-performance alloys, other minority elements, i.e. RE, Si and Ca are added. For high-performance gravity casting alloys, aluminium is completely removed and alloys containing zinc, zirconium, and rare earths are the most common.

### 2.3.1 Metallurgical background of the Mg-Al alloys

Several researchers [AGH98, CAC02a, CAO04, CAR97, FOX43, and STJ03 amongst others] have analysed the microstructure and mechanical properties of Mg-Al alloys.

One of the most interesting properties of Mg-Al alloys is their good castability. In addition, high levels of Al improve the castability in spite of an increase in the volume fraction of eutectic [STJ03]. The amount of eutectic is high in AZ91. This is one of the alloys under investigation in this work, and therefore, it is essential to understand the role of the eutectic in the microstructure of Mg-Al alloys. This section focuses on the description of the eutectic precipitation in these alloys.

According to the Mg-Al equilibrium phase diagram, the  $\gamma$ -Al<sub>12</sub>Mg<sub>17</sub> phase, which is the one appearing in the eutectic reaction, is expected to appear when the aluminium content reaches ~13 wt%. Although in equilibrium an alloy should not exhibit any eutectic structure, in non-equilibrium solidification sufficient liquid enrichment can occur. Consequently, the eutectic structure can appear. It has been reported [EML66, STJ03], that in Mg-Al alloys with about 2 per cent aluminium, particles of  $\gamma$ -Al<sub>12</sub>Mg<sub>17</sub> can appear depending upon the cooling rate. The reason is that alloys do not follow the equilibrium phase diagram in real casting procedures, where the cooling rate is higher than that required for equilibrium solidification. When an alloy reaches the liquidus point, the solute composition of the generated solid is smaller than the solute content in the alloy. Therefore, the liquid is enriched in solute. The path followed in the phase diagram for a non-equilibrium cooling is given by Carlson [CAR97] in Figure 2.10 for a Mg-Al alloy. In this diagram, the  $\gamma$ -Al<sub>12</sub>Mg<sub>17</sub> intermetallic is denoted with  $\beta$ .

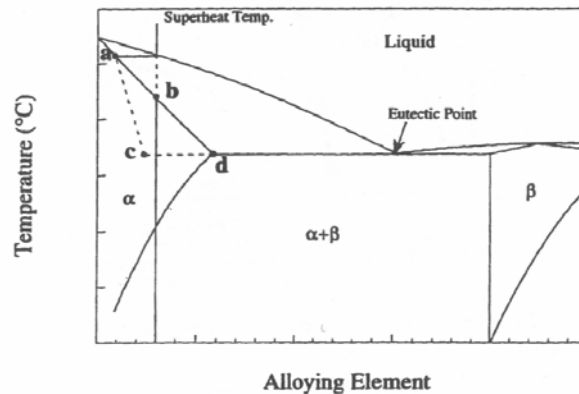


Figure 2.10. Schematic composition paths during Mg-Al non-equilibrium solidification [CAR97].

Aghion and Bronfin [AGH98] explain the solidification of AZ91 alloy in ingot casting, where the cooling rate is relatively slow, compared to sand-casting. However, it is not an equilibrium solidification. They report that solidification starts at 595°C. The first crystals contain approximately 1.5% Al. Aluminium content increases as solidification continues, and the surface of the grain can have contents of 9% aluminium [AGH98].

Eutectic can be produced in several morphologies in magnesium alloys as is shown in Figure 2.11.

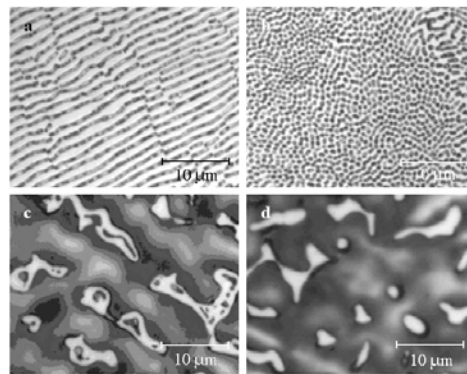


Figure 2.11. a) Lamellar, b) fibrous, c) partially divorced and d) fully divorced morphologies in Mg-Al alloys of various compositions [STJ03].

StJohn *et al.* report [STJ03] that for alloy compositions and casting conditions used commercially (gravity and high-pressure casting), the eutectic morphology is generally fully or partially divorced. Fully divorced morphologies are usually formed in die-casting, while partially divorced morphologies are more likely at lower cooling rates. They explain that at high cooling rates, the isolated regions between dendrite branches are smaller and the undercooling higher. Therefore, fully divorced eutectic is more usual because nucleation in the interdendritic liquid is required in each of these regions. Since the undercooling required for nucleation is larger than the undercooling required for growth, the phases already present are more likely to grow forming the divorced eutectic. In the same work, it is also reported that aluminium content influences the morphology. A reduction in aluminium content favours a more divorced morphology, but ternary additions can change this trend.

Fox and Lardner [FOX43] detail further the precipitation and generation of the pseudo-eutectoid form of the precipitated  $\gamma$ -Al<sub>12</sub>Mg<sub>17</sub> phase after solution treatment and posterior precipitation treatment. They



highlight the importance of the aluminium content, of the heat-treatment temperature and, to a lesser extent, of the heat-treatment time for the precipitation of  $\gamma$ -phase. They distinguish 4 kinds of precipitates in their work. The first kind is the grain boundary precipitate, which grows from the grain boundaries of the supersaturated  $\alpha$  solid solution in the form of continuous waves. The extent of these grain-boundary-precipitate areas depends upon the aluminium content of the supersaturated solid solution and upon the temperature at which the specimen is treated. Those precipitates are called troostite, sorbite and pearlite because of their resemblance to steel precipitates. However, the three types of structure are varieties of one main form, as it is possible to obtain intermediate structures between the two extremes. In troostite, the two phases ( $\alpha$ -Mg and  $\gamma$ -Al<sub>12</sub>Mg<sub>17</sub>) can hardly be recognized as two phases. The sorbite is a coarsened troostite, where the particles show a tendency to lie in parallel layers. Finally, the pearlite shows a fully lamellar structure. Emley [EML66] reports that long heat-treatment times, high temperatures, and low aluminium contents favour coarse pearlite. The second kind of precipitate cited in [FOX43] is the osmondite, which can be crystallographic, uniform or granular. The osmondite comprises the precipitates which are produced in areas not affected by the growth of the grain-boundary precipitates and appears when the grain boundary precipitation ceases. The crystallographic osmondite is the first appearance of osmondite, and needs an "incubation" period. The uniform osmondite is produced from crystallographic osmondite, where the precipitate remains in the form of extremely small particles. In further heating, the orientation of the precipitates is more marked, forming parallel layers, small lozenge-shaped flakes lying in the (0001) crystallographic plane or small bars. The third kind of precipitation is the mosaic type, which appears when large grain growth has taken place during the solution treatment. It is formed by irregular lines of very small precipitated particles going across the grains. It appears that mosaic precipitation may occur as a result of  $\gamma$ -Al<sub>12</sub>Mg<sub>17</sub> particle precipitation on the sites of original grain boundaries. Finally, the spheroidite kind of precipitates appear in continued heat-treatment when the precipitated structures coarsen growing into spheroidal particles, presumably the form in which the energy of the system is at a minimum.

### 2.3.2 Metallurgical background of Mg-Zn-Zr-Nd-Gd-Y alloys

Mg-Zn-Zr-RE alloys are of interest for high strength and high temperature applications [EML66]. However, due to the high reactivity of Zr, only a few elements are compatible with it. The most recognised elements compatible with Zr are Zn, RE, Y and Ag [AGH04]. In this work an alloy containing Mg-Zn-Zr-RE-Y has been analysed.

The addition of rare-earth elements is interesting because these alloys show precipitation hardening by aging [HON07]. Bronfin *et al.* [BRO07] suggest an optimal combination in concentration of gadolinium, yttrium and neodymium to obtain high strength alloys. Nd has a good combination of enhanced solid solubility, availability and low cost, but contents higher than 3% result in significant embrittlement. However, they state that Nd should be considered as the main alloying element. Y and particularly Gd have higher solubility in magnesium than Nd, but they are expensive. Furthermore, Gd, because of its great atomic weight, requires higher additions in weight to have the same atomic percentage compared to Y and Nd.

This section is divided into the analysis of alloys having Zn as a major element and rare earths as the main alloying elements.

### 2.3.2.1 Mg-Zn based alloys

Rao *et al.* [RAO06] report the appearance of MgZn and MgZn<sub>2</sub> nano-sized precipitates that may improve the precipitation strengthening for Mg-Zn-Y alloys. On the other hand, Boris *et al.* [BRO07] indicate that Zn content should be limited in most cases to 0.3-0.8% when zinc is added to a magnesium alloy containing rare earths. The reason is that zinc combines with Nd, Y and Gd to form stable eutectic intermetallics. Thereby, it nullifies the contribution of the above elements to precipitation hardening. However, higher Zn contents can be used in some cases when solid solution strengthening is considered as an alternative strengthening mechanism. Suzuki *et al.* [SUZ03] report that the addition of Zn leads to the formation of planar defects in the (0001) plane after solid solution. Thus, confinement of dislocations in the basal plane and suppression of non-basal slip occur.

Li *et al.* [LI07] have analysed the effect of Nd and Y additions in Mg-Zn-Zr alloys. They conclude that, when only Nd is added to Mg-Zn-Zr alloys, a continuous network of T phase precipitates is formed around the grain boundary. Those precipitates are ribbon-shaped and lamellar eutectics and they reduce the ductility and the ultimate tensile strength. Wei *et al.* [WEI97] define the T phase as a ternary phase of c-centred orthorhombic crystal structure exhibiting a wide range of stoichiometry. When Li *et al.* [LI07] add Nd contents up to 2 wt.%, the W phase coexists with T phase. In this case, the continuous lamellar eutectics became predominant. Yang *et al.* [YAN08] have also analysed the effect of Nd in Mg-Zn alloys. They agree with Li *et al.* in that the addition of 2 wt.% Nd to a Mg-4.5Zn (wt.%) alloy leads to the precipitation of a continuous network of interdendritic compounds leading to a decrease in mechanical properties. However, the addition of 1 wt.% Nd improves the mechanical properties of Mg-4.5Zn (wt.%) alloy. When Li *et al.* [LI07] add 0.5-1 wt.% Y to Mg-5Zn-2Nd-0.6Zr (wt.%) alloy, individual formation of the W phase in the form of lamellar eutectics with  $\alpha$ -Mg is obtained. The addition of Y polygonises and thickens the lamellar eutectics and lessens the continuity of the eutectic networks. Therefore, UTS and elongation are improved. They also find out that the addition of Nd and Y to Mg-Zn-Zr alloys refines the dendritic size, increases the interdendritic phase amount and improves the thermal stability of these interdendritic phases. Conversely, Yang *et al.* [YAN08] do not observe any grain refining effect with the addition of Nd. Figure 2.12 shows the evolution of the microstructures of Mg-Zn-Zr alloys with the addition of Nd and Y. Figure 2.13 shows the TEM image of the lamellar W phase.

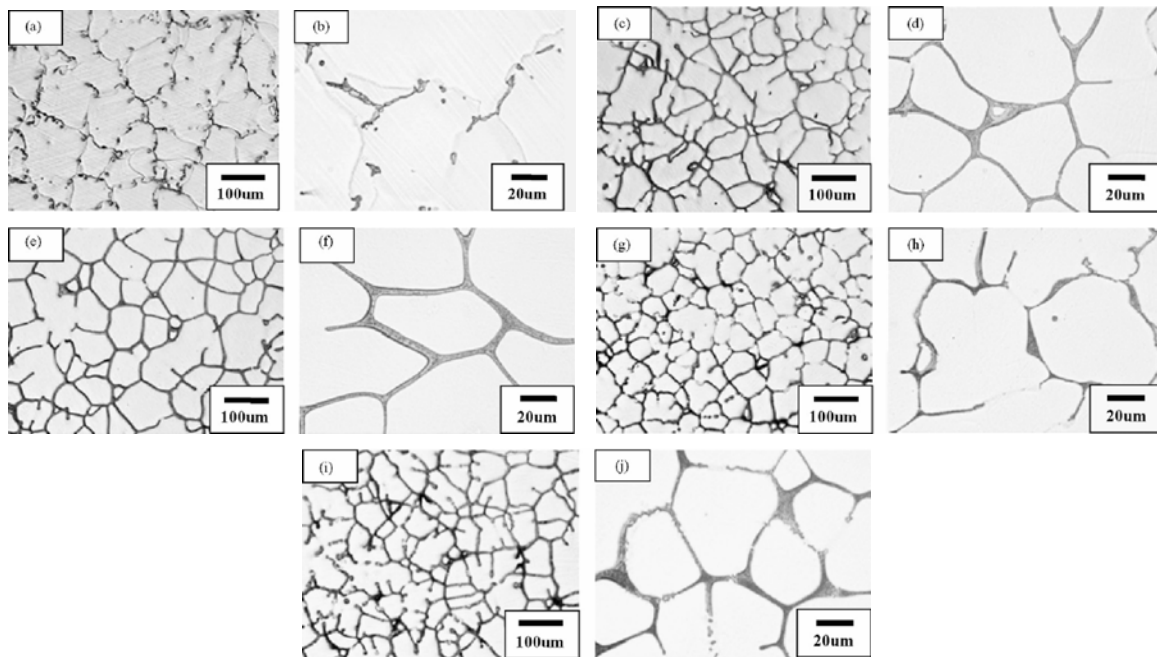


Figure 2.12. Optical micrographs of as-cast alloys at two magnifications each; a) and b) Mg-5Zn-0.6Zr (wt.%); c) and d) Mg-5Zn-1Nd-0.6Zr (wt.%); e) and f) Mg-5Zn-2Nd-0.6Zr (wt.%); g) and h) Mg-5Zn-2Nd-0.5Y-0.6Zr (wt.%); i) and j) Mg-5Zn-2Nd-1Y-0.6Zr (wt.%) [LI07].

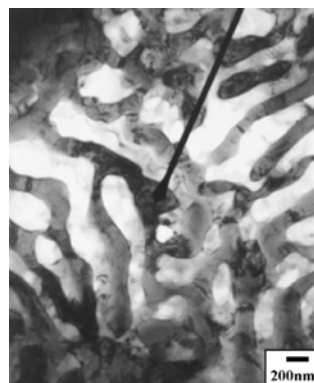


Figure 2.13. TEM BFI showing lamellar eutectic W phase observed in Mg-5Zn-2Nd-1Y-0.6Zr (wt.%) alloy [LI07].

### 2.3.2.2 Mg-RE based alloys

The increase in hardness and strength in Mg-Nd alloys is reported to be due to the formation of plate shaped “GP” zones on one hand and  $Mg_3Nd$  phase and precipitates on prismatic planes of the Mg matrix on the other [PIK73].

Aghion *et al.* [AGH08] summarise the strengthening effect of the addition of Y to a Mg-3Nd (wt.%) alloy schematically, which is illustrated in Figure 2.14. The strengthening effect of Y after T6 heat treatment is explained. The strengthening happens by solid-solution and precipitation. The solubility of Y in magnesium leads to solid-solution strengthening and the formation of a fine dispersed ternary  $\beta'$  ( $Mg_x(Nd,Y)_{1-x}$ ) intermetallic phase is the cause of precipitation strengthening.

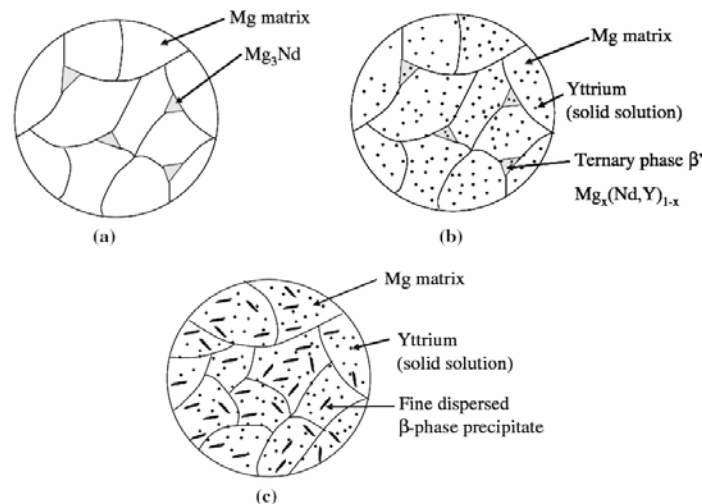


Figure 2.14. Schematic illustration of the strengthening mechanism of yttrium in Mg-3%Nd. a) Mg-3%Nd in as-cast condition; b) Mg-3%Nd-2%Y in as-cast condition; c) Mg-3%Nd-2%Y after T6 heat treatment (all numbers relates to wt.%) [AGH08].

Gill *et al.* [GIL04] analyse the microstructures of three Mg-RE-Zn-Zr alloys. As-cast and solution heat-treated microstructures of the Mg-2.8Nd-0.6Zn-0.46Zr-0.29Gd (wt.%) alloy are shown in Figure 2.15. The as-cast microstructure is formed by equiaxed dendrites of  $\alpha$ -Mg solid solution surrounded by a divorced eutectic. The divorced eutectic is composed of  $\alpha$ -Mg solid solution and Nd-rich second phase. Solution treatment results in the formation of large, 0.1-1  $\mu\text{m}$ , precipitates in the centre of the  $\alpha$ -Mg grains for the Zn containing alloys. Some other authors [MUK97, TIK71] report the presence of  $(\text{MgZn})_{12}\text{Nd}$  precipitates in Mg-RE-Zn-Zr alloys.

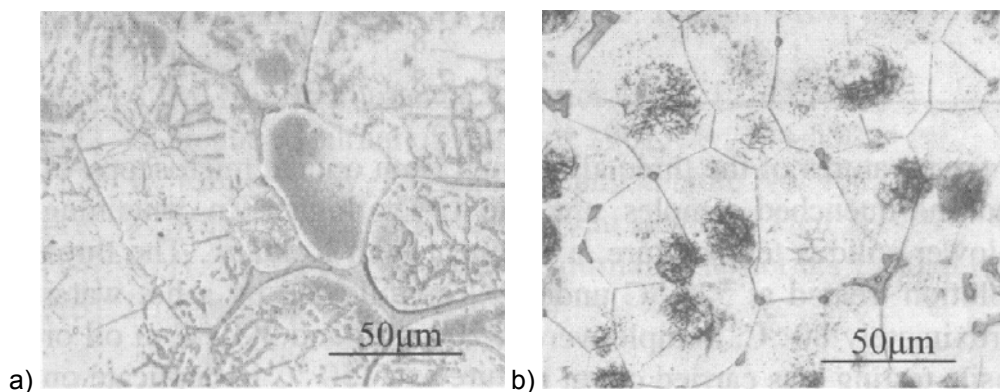


Figure 2.15. Mg-2.8Nd-0.6Zn-0.46Zr-0.29Gd (wt.%) microstructures; a) as-cast; b) solution treated [GIL04].

Penghuai *et al.* [PEN08] work in the same framework as Gill *et al.* They describe the microstructures and mechanical properties of the Mg-3Nd-0.2Zn-0.4Zr (wt.%) alloy. In their study they describe an  $\alpha$ -Mg matrix with eutectic precipitation of  $\text{Mg}_{12}\text{Nd}$  in the grain boundaries in the as-cast condition. In the solution treated condition, they indicate that the eutectic compounds have almost dissolved into the matrix. Instead, they find small gathered precipitates in the grain interior, which they identify as  $\text{ZrH}_2$  and  $\text{Zn}_2\text{Zr}_3$ . They detect some other Zr-containing unidentified particles. Those microstructures are shown in Figure 2.16.

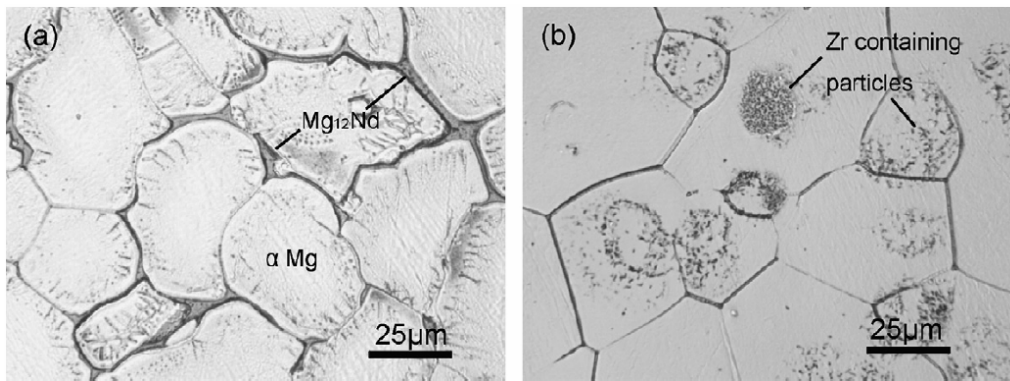
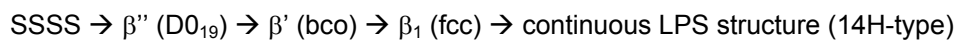


Figure 2.16. Optical micrographs of Mg-3Nd-0.2Zn-0.4Zr (wt.%) alloy: a) as-cast and b) solution treated at 540°C for 6 h [PEN08].

Honma *et al.* [HON07] analyse the effect of Zn additions on the age hardening of Mg-Gd-Y-Zr alloys. They work on the improvement of strength, elongation and creep resistance of these alloys compared to the commercial WE54 alloy. They follow the work presented in previous investigations by other authors [ANY01a, ANY01b, KAW01]. Homma *et al.* report that the precipitation sequence in Mg-2.0Gd-1.2Y-1.0Zn-0.2Zr (at.%) alloy aged at 225°C is:



Concurrent precipitations of  $\beta'$  and  $\beta_1$  phases are attributed to the maximum hardness. Zn does not join  $\beta'$  phases. Zn additions mostly contribute to the formations of  $\beta_1$  phases and 14H-type long-period stacking LPS structures. As a result, it minimizes the total energy in the system and leads to active movement of dislocations on the basal planes. Honma *et al.* [HON07] conclude that this is the reason for the unusual improvement in elongation when adding 1.0% Zn to the Mg-2.0Gd-1.2Y-0.2Zr at.% alloy.

### 2.3.2.3 Description of the MRI207S alloying system

Avraham *et al.* [AVR07] analyse the precipitates generated in the alloy of this work, the MRI207S alloy, based on the Mg-Zn-Zr-Nd-Y (Gd) system. With regard to the precipitated phases, they find the  $\text{GdMg}_3$  phase except in the solubilised alloy. Table 2.2 shows the precipitates they detect in the MRI207S alloy for as cast, solubilised (T4) and after thermal exposure at 200°C for 32 days.

Table 2.2. Phases detected by XRD after different thermal treatments in the MRI207S alloy ( $\alpha$ -Mg excluded) [AVR07].

Alloy	Initial state	Thermally exposed/aged at 200°C for 32 days
MRI207S-F	$\text{GdMg}_3$	$\text{GdMg}_3$
MRI207-T4	-----	$\text{GdMg}_3$

Figure 2.17 shows the BSE micrographs of the MRI207S-F alloy and the same alloy after thermal exposure at 200°C for 32 days presented by Avraham *et al.* [AVR07]. In the as-cast state (F), Zr and Gd are detected at the centre of the  $\alpha$ -Mg matrix, with an eutectic phase of (Gd,Nd) $\text{Mg}_3$  and Zr in the

grain boundaries. Y and Nd are detected in the grain boundary area. After thermal exposure Zr and Gd are also detected at the centre of the  $\alpha$ -Mg matrix. Fine precipitation of  $(\text{Gd-Nd})\text{Mg}_3$  takes place in the matrix. In the grain boundary area it appears as a continuous layer.

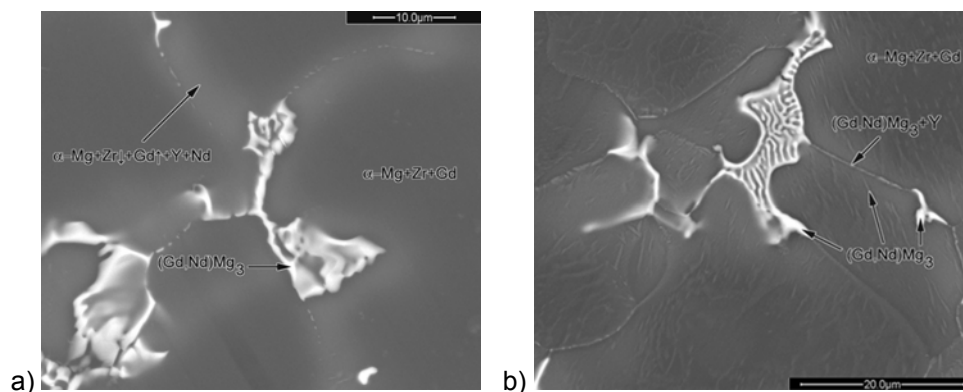


Figure 2.17. a) BSE micrograph of alloy MRI207S-F; b) BSE micrograph of MRI207S-F after thermal exposure at 200°C for 32 days [AVR07].

Precipitation hardening and grain boundary strengthening are the major mechanisms which contribute to the strength of MRI207S alloy [BRO07] after a solution and precipitation heat treatment (T6).

## 2.4 Heat Treatment of Mg-Alloys

Mg alloys can be strengthened by the four most well-known strengthening mechanisms: solid solution strengthening, precipitation hardening, grain boundary strengthening and dislocation hardening or work hardening [AGH04].

Solid solution strengthening happens when solute atoms are placed in the matrix generating substitutional or interstitial point defects in the crystal. Point defects generate lattice distortions that make the movement of the dislocations difficult. The temperature and time required for solid solution treatment should be sufficient to dissolve the eutectic intermetallic phases formed during the solidification of the alloy. Practically, the solid solution treatment is conducted at a temperature of about 20-30°C below the solidus temperature of the alloy [BRO07].

Precipitation hardening is based on the formation of a second phase, which acts as a pinning point in a similar manner to solutes in the solid solution strengthening. In this case, the particles are composed of an intermetallic phase instead of a single atom. This effect is marked only in alloys where fine coherent precipitates of GP zones (Guinier-Preston zones) are formed [AGH04]. Guinier-Preston zones are the first precipitates to form and are coherent with the matrix. They are a small precipitation domain in a supersaturated metallic solid solution. With continued aging, Guinier-Preston zones transform to more stable precipitates [ASM85].

Grain boundary strengthening is based on the fact that different grains have different orientations and that there is a discontinuity of slip planes from grain to grain. Therefore, grain boundaries act as an impediment to the dislocation motion and small grain sizes mean a higher strength of the material. Grain refining is used for the grain boundary strengthening (see the section on nucleation mechanisms of this chapter).

Finally, work hardening occurs due to the pile up of dislocations, which also acts as an impediment to the dislocation motion.

The basic temper designations used are shown in Table 2.3.

Table 2.3. Basic temper designations [AVE99].

Designation	Expansion
F	As-fabricated
O	Annealed, recrystallised (wrought products only)
H	Strain hardened (wrought products only)
H1	Strain hardened only
H2	Strain hardened and partially annealed
H3	Strain hardened and stabilized
W	Solution heat treated; unstable temper
T	Heat treated to produce stable tempers other than F, O or H
T2	Annealed (cast products only)
T3	Solution heat treated and cold worked
T4	Solution heat treated
T5	Artificially aged only
T6	Solution heat treated and artificially aged
T7	Solution heat treated and stabilized
T8	Solution heat treated, cold worked and artificially aged
T9	Solution heat treated, artificially aged, and cold worked
T10	Artificially aged and cold worked

In this study, the hardening mechanism used is precipitation hardening. The relationship between the required temperature and time for precipitation hardening found by Jenkins and Bucknall [JEN35] is given in Eq. 2.6. This equation gives the time needed to obtain the maximal hardness of the material,

$$t = Ce^{\frac{m}{T}} \quad \text{Eq. 2.6}$$

where  $t$  is the time in hours,  $T$  is the absolute temperature in degrees and  $m$  and  $C$  are constants for the particular alloy system. Fox and Lardner [FOX43] obtained a straight line when plotting the log of time in hours against the reciprocal of the absolute temperature for the alloy AZ91, which is in agreement to the above formula. They suggested that the period required for maximum hardening at 100°C would be 40 days, and at room temperature (15°C) about 40 years.

## 2.5 Correlation between mechanical properties and microstructure

For a polycrystalline material, the ductility will be dependent upon the texture. For random orientation, as obtained in castings for the present work, the ductility will increase with a decrease in the grain size [EML66]. Figure 2.18 shows the relationship between grain size and ductility for pure magnesium. In the same book, Emley also refers to the stress to be applied. During deformation of a polycrystalline material, considerable stresses must develop at boundaries between grains which are unfavourably oriented for slip and adjacent grains in which slip can occur readily. Therefore, tensile properties of Mg alloys should increase more rapidly in Mg alloys with decreasing grain size than in the case of cubic metals for which more modes of deformation are possible.

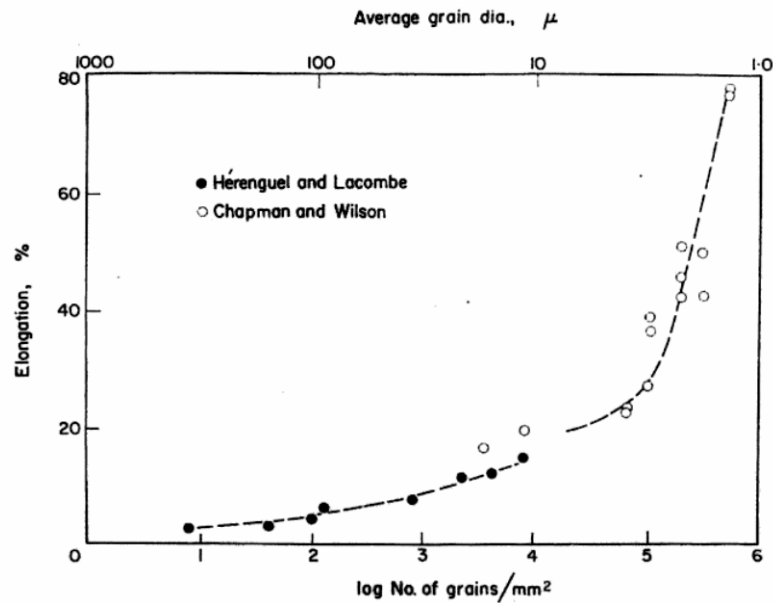


Figure 2.18. Relation between grain size and ductility for pure magnesium [EML66, data taken from HER36, CHA62].

The yield stress of metals,  $\sigma_y$ , and alloys usually follows the Hall-Petch equation [HAL51, PET53] (Eq. 2.7).

$$\sigma_y = \sigma_0 + kd^{-1/2} \quad \text{Eq. 2.7}$$

where  $\sigma_0$  and  $k$  are experimentally derived constants and  $d$  is the measure of the grain diameter. It is thought that the friction stress,  $\sigma_0$ , is possibly related to the critical resolved shear stress (CRSS) for basal slip while  $k$  seems to be related to slip in the prismatic system [ARM83].  $k$  seems to be dependent on texture, having a lower value for textured materials [AND03].

Pfeiler [PFE07] in his book proposes a more specific explanation of the Eq. 2.7. He argues that the Hall-Petch law, which was first explained in terms of dislocation pile-ups emitted by sources and blocked against grain-boundaries, cannot describe large-grain materials where long dislocation pile-ups have never been observed. Therefore, he proposes the Eq. 2.8.

$$\sigma_y = \alpha\mu b\sqrt{\rho} + cte = \alpha\mu\sqrt{\varepsilon b/d} + cte \quad \text{Eq. 2.8}$$

where  $\alpha$  is the proportionality coefficient,  $\mu$  is the shear modulus,  $b$  is Burgers vector,  $\rho$  is the density of dislocations,  $d$  is grain size and  $\varepsilon$  is the plastic strain. This equation is similar to the Eq. 2.7 with  $k = \alpha\mu\sqrt{\varepsilon b}$ . Taking  $\varepsilon=0.2\%$ ,  $k$  has the right order of magnitude. However, most authors use the Hall-Petch equation described in Eq. 2.7 instead of the Eq. 2.8, because it is usually valid in commonly used alloys.

Blake and Cáceres [BLA08] define the Hall-Petch coefficients  $k$  and  $\sigma_0$  as dependent on temperature. They base their study on the conclusions of Armstrong [ARM68, ARM83], where  $k$  is defined as dependent on  $\tau_p$  in a relationship of  $(\tau_p)^{1/2}$  and  $\sigma_0$  varies with temperature as does  $\tau_b$ .  $\tau_p$  is



the critical resolved shear stress of the prism slip system and  $\tau_b$  of the basal system. Blake and Cáceres [BLA08] express  $k$  by the following relationships (Eq. 2.9):

$$k = \alpha(\tau_p)^{1/2} \quad \text{Eq. 2.9}$$

where  $\alpha$  is a constant.

$\sigma_o$  is described by Eq. 2.10,

$$\sigma_o = m\tau_b = m(\tau_o + B_r c^{2/3} + B_s [c(1-c)]^2) \quad \text{Eq. 2.10}$$

where  $m$  is the Taylor factor (=4.5 [CAC??]),  $\tau_o$  is the CRSS<sub>basal</sub> of pure Mg (=0.5 MPa [AKH72]),  $B_r$  is the strengthening coefficient for random solid-solution (=43.2 MPa [AKH72]) and  $B_s$  that of short-range order (SRO) (=6000 MPa [CAC02b]). A value of  $\alpha = 0.058 \text{ MPa}^{1/2} \text{ m}^{1/2}$  was chosen for Mg-Zn alloys, being  $k \approx 0.40 \text{ MPa m}^{1/2}$  for Mg-Zn alloys [BLA08].

The Hall-Petch coefficients described in literature for Mg alloys ( $k$  and  $\sigma_o$ ) are listed in the Table 2.4.

Table 2.4. Hall-Petch coefficients for several Mg-alloys for determining tensile yield strength.

Alloy	Material history	$k$ (MPa m <sup>-1/2</sup> )	$\sigma_o$ (MPa)	Ref.
Pure Mg	Grain refined by hot extrusion and annealing	0.22	12	[HAU56]
Pure Mg	Cast with Zr grain-refinement and stress relieved	0.25	17.7	[AND03]
Mg-2wt.%Zn	Sand-cast with Zr grain refinement	0.47	3.1	[MAN04]
AZ91	Gravity die-cast with grain refinement	0.181	40	[CAR97]
AZ91	Extruded at 200°C	0.21	130	[NUS89]
AZ91	Extruded at 200~450°C	0.23	144	[MAB00]
AZ91	Sand-cast (as-cast)	0.42	66	[COU66 in CAC02a]
AZ91	Sand-cast with undefined T6	0.60	84	[COU66 in CAC02a]
AZ91	Squeeze cast + T6 (420°C/16h+205°C/4h)	1.25	60	[YUE95 in CAC02a]
AZ91	Gravity cast (as-cast)	0.32	53	[SAS96 in CAC02a]
AZ91	Gravity cast + T6 (420°C/16h+205°C/4h)	0.48	77	[SAS96 in CAC02a]

Cáceres *et al.* [CAC02a] give some possible reasons for the high discrepancy of the Hall-Petch parameters shown in Table 2.4, where  $k$  values go from  $0.181 \text{ MPa} \sqrt{\text{m}}$  to  $1.25 \text{ MPa} \sqrt{\text{m}}$ . One of the first reasons could be the lack of a wide range of grain sizes due to the nonexistence of effective grain

refiners for Mg-Al alloys. This generates the deficiency in statistics. Secondly, it is difficult to dissolve the  $\text{Al}_{12}\text{Mg}_{17}$  particles during solution-treatment without causing grain growth, making it hard to explore small grain sizes, particularly in die cast material. Thirdly, some results, particularly for extruded material, may have been affected by preferred orientation effects.

Eq. 2.7 will be used in this thesis for the establishment of relationship between microstructures and mechanical properties. The reason for this is their easy applicability, even if the integration of the effect of precipitates in the equation proves to be interesting for future works. Summarising, the Hall-Petch relationship is valid when a single phase is present or when the phases in the material do not vary. If the precipitated phases or the distribution of solute elements differs, the constants of the relationships will change.

## 2.6 Fracture mechanisms

Pure magnesium, and conventionally, cast alloys show a tendency for brittleness. The fracture of pure magnesium near and below room temperature is described [AVE99] as happening primarily due to the joining of intergranular cracks. Those intergranular cracks form on  $\{30\bar{3}4\}$  or higher-order planes, such as  $\{10\bar{1}4\}$  or  $\{10\bar{1}5\}$ . At elevated temperatures, cracking and cavitation at grain boundaries become much more important factors in the fracture of magnesium.

The most used alloys are based on the Mg-Al system, whose fracture mechanisms are analysed in this section.

An important feature of Mg-Al alloys is the presence of the  $\gamma\text{-Al}_{12}\text{Mg}_{17}$  phase at grain boundaries, which is known to be fragile. The eutectic interface provides a convenient crack path around the more ductile magnesium dendrites. The result is a sharp decrease in the ductility of the alloys [STJ03]. The as-cast properties of Mg-Al alloys increase with aluminium content up to about 6%, after which the UTS falls gradually and the elongation falls rapidly due to the increasing proportions in the grain boundaries of the relatively brittle  $\gamma\text{-Al}_{12}\text{Mg}_{17}$  phase [EML66]. An example of how large deposits of  $\gamma\text{-Al}_{12}\text{Mg}_{17}$  phase can lead to fracture paths is shown in Figure 2.19. This microsection is taken longitudinally close to the point of failure. The sample is a solution-treated test-piece showing numerous large deposits of the  $\gamma$  phase. These cracks disappeared after fully heat-treated conditioning. Therefore, heat treatments could be applied to reduce the brittle effect of continuous  $\gamma\text{-Al}_{12}\text{Mg}_{17}$  precipitates.

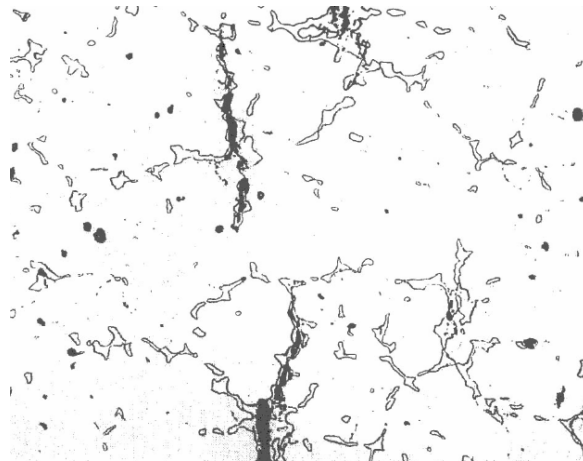
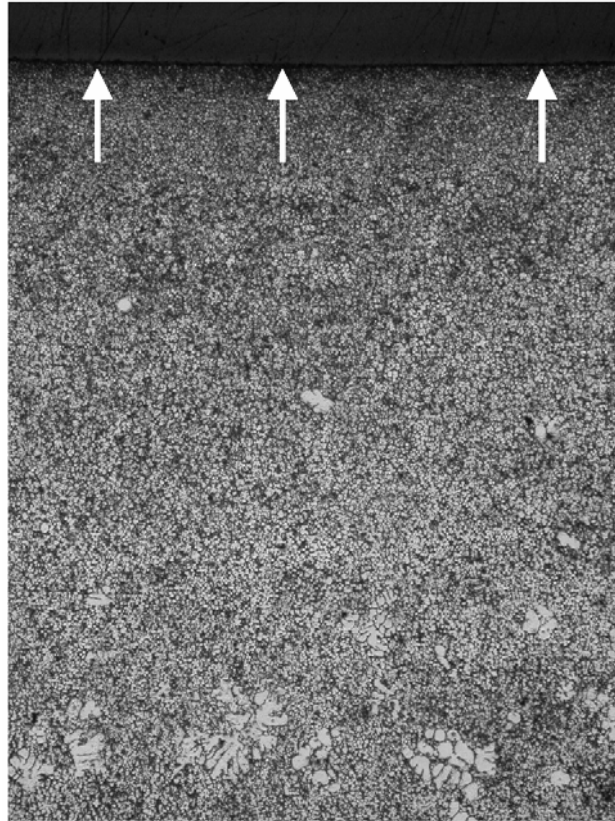


Figure 2.19. A Mg-8%Al-4%Zn alloy solution treated for 30 hr. at 365°C, showing a premature fracture in the residual  $\gamma$ -Al<sub>12</sub>Mg<sub>17</sub> phase away from the main fracture. This cracking tendency disappeared after precipitation [FOX45].

HPDC alloys have two regimes, plasticity and void formation. Assuming that there is no porosity, on loading, plastic deformation starts in the  $\alpha$ -Mg matrix. Stress concentrations develop between the  $\alpha$ -Mg and the  $\gamma$ -Al<sub>12</sub>Mg<sub>17</sub> particles. When the dislocation pile-ups become large enough, either the fracture of  $\gamma$ -Al<sub>12</sub>Mg<sub>17</sub> particles or the decohesion of the  $\gamma$ -Al<sub>12</sub>Mg<sub>17</sub>/ $\alpha$ -Mg interface occurs and a void or microcrack is formed [SEQ04].

In high-pressure die-castings two regions can be distinguished: a fine-grained skin-region and an interior zone as shown in Figure 2.20. The large grains have a typical size of 20-30  $\mu$ m and are oval in shape. The fine grains ranged in size from 1  $\mu$ m to 5-10  $\mu$ m with their size tending to be finer within the surface layer [AGH98]. Sequeira and Dunlop [SEQ04] state that the difference in microstructure causes the surface to have a higher yield strength. It is because of the presence of a high volume fraction of  $\gamma$ -Al<sub>12</sub>Mg<sub>17</sub> intermetallic in the skin regions of the castings combined with a high dislocation density, increased solute (Al) in the  $\alpha$ -Mg grains, and the constraining effects of the hard  $\gamma$ -Al<sub>12</sub>Mg<sub>17</sub> phase. The process of void formation starts with voids first forming in the fine grained regions.



*Figure 2.20. Cross section of a die-cast test plate of alloy AM60. The arrowheads show the fine grained surface [KOC03].*

Crack paths are intergranular for small grain-sized magnesium alloys. Intergranular regions are covered by intermetallic phases and the decohesive force of these regions is lower than the cleavage force required for transgranular cracking in small  $\alpha$ -Mg grains. The result is a ductile dimple fracture surface, which is the result of growth and coalescence of microvoids [YAN04]. When the crack encounters a large  $\alpha$ -Mg grain, cleavage or transgranular fracture may occur. When large grains are encountered by the advancing crack, intergranular fracture is still predominant but some of these large grains may fracture transgranularly [SEQ04].

Magnesium alloys do not usually show any necking behaviour at room temperature testing. For example, although the AZ91D high-pressure die-castings show ductile fracture, they do not have necking behaviour. This means that once voids are formed and reach a critical density, the material fails catastrophically [SEQ04].

## **2.7 Deformation modes and texture development in Mg-Alloys**

In this section, the deformation mechanisms in magnesium are described. Thereafter, a general description of the texture in polycrystalline materials and the development of texture during deformation are discussed.

Figure 2.21 illustrates the principal deformation planes and directions for a better understanding of this section.

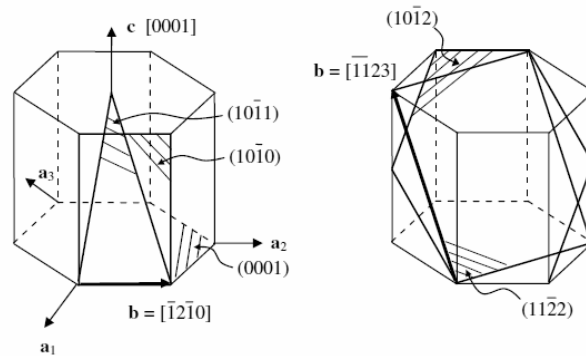


Figure 2.21. Relevant hexagonal close packed crystal planes for slip and twinning in magnesium [AGN05].

### 2.7.1 Deformation modes in magnesium and its alloys

Compared to, for example, the face-centred cubic (fcc) structure, the hexagonal close-packed (hcp) crystal structure of magnesium has fewer slip systems. Therefore, its ability to be deformed is limited, especially at low temperatures.

Staroselsky *et al.* [STA03] state that crystallographic slip in hcp single crystals is commonly observed to occur on the basal or prismatic systems. However, for magnesium polycrystals, most authors [AVE99, EML66, PEK03, and STA03, among others] agree that, at room temperature, deformation occurs mainly by slip on the basal planes at room temperature. These investigations reveal that deformation of pure magnesium takes place mainly by slipping in the basal plane of the hexagonal crystal lattice and by twinning at temperatures up to around 225°C. It is not until the temperature rises above this level that further (pyramidal and prismatic) slipping planes are activated. This causes a strong increase in formability [STA01]. Kainer [KAI03], in his analysis, suggests that extensive deformation only occurs above 225°C.

There are only three equivalent basal slip systems in magnesium, which are the three  $\langle 11\bar{2}0 \rangle$  most closely packed directions in the (0001) plane. However, the compatibility of deformation in polycrystals requires at least five independent slip systems [TAY38]. The  $\langle 11\bar{2}0 \rangle$  direction is also present in the  $\{10\bar{1}0\}$  vertical face planes (prismatic) and in the  $\{10\bar{1}1\}$  pyramidal planes. However, the  $\{10\bar{1}1\}$  pyramidal plane is only active at elevated temperatures (above 225°C) [AVE99, EML66, PEK03].

Due to the fact that all the  $\langle 11\bar{2}0 \rangle$  directions are perpendicular to c-axis, slip on the systems listed above, does not produce any elongation or shortening parallel to the c-axis [STA03]. In order to accommodate the deformation in the c-direction, other slip or twin systems must be operative. In magnesium, twinning is the dominant mechanism. Twinning re-orientates basal planes favouring the orientation of the grains for slip, even though it is only a finite amount of strain that may be accommodated by twinning [AGN05]. Twinning on the pyramidal  $\{10\bar{1}2\}$  plane is widely reported [AVE99, EML66, GEH05, NAV04, YI05], and it is also called tensile twin. The activation of twinning itself is dependent on the grain orientation [EML66]. Twinning of this type is only possible in compression with stresses parallel to the basal plane (0001) and only with stresses perpendicular to

the basal plane in tension. Other twins are reported [NAV04], which are the contraction twinning on the  $\{10\bar{1}1\}$  and  $\{10\bar{1}3\}$  planes and the double twins where the matrix twins on either a  $\{10\bar{1}1\}$  or  $\{10\bar{1}3\}$  plane and then the material inside the twin twins on a plane such that both twinning events produce rotation about the same  $\langle 10\bar{1}2 \rangle$  axis.  $\{30\bar{3}4\}$  results from  $\{10\bar{1}1\}$  twins re-twinning according to  $\{10\bar{1}2\}$  in the re-oriented lattice [EML66]. The characteristic misorientation relationships resulting from types of twinning commonly observed in Mg are listed in Table 2.5.

Table 2.5. Misorientations between the matrix and primary or secondary twins commonly observed in Mg [NAV04].

Type of twin	Misorientation angle/axis
$\{10\bar{1}1\}$	$56^\circ \langle 10\bar{1}2 \rangle$
$\{10\bar{1}2\}$	$86^\circ \langle 10\bar{1}2 \rangle$
$\{10\bar{1}3\}$	$64^\circ \langle 10\bar{1}2 \rangle$
$\{10\bar{1}1\}$ - $\{10\bar{1}2\}$	$38^\circ \langle 10\bar{1}2 \rangle$
$\{10\bar{1}3\}$ - $\{10\bar{1}2\}$	$22^\circ \langle 10\bar{1}2 \rangle$

### 2.7.2 Description of the texture

The commonly used metallic materials are polycrystalline, containing several crystallites. When the material is cast, a random orientation of the grains is usually achieved. Nevertheless, thermo-mechanical treatments can lead to the obtaining of a preferred orientation of the crystals. When a material shows a preferred orientation, it is said that the material has a texture. When the texture is random, there is no preferred orientation of the grains. A strongly textured material behaves similarly to a single crystal, inheriting, for example, the anisotropic behaviour.

The texture of a polycrystalline material is defined as the orientation distribution function of its crystallites with respect to a given sample coordinate system (Eq. 2.11) [BUN89, YI05].

$$f(g) = \frac{dV/V}{dg}; \quad g = \{\{\varphi_1, \phi, \varphi_2\}\} \quad \text{Eq. 2.11}$$

$$dg = \frac{\sin \varphi}{8\pi^2} d\varphi_1, d\phi, d\varphi_2$$

$dV/V$  is the volume fraction of crystallites having a crystallographic orientation  $g$  within the limits  $dg$ . An orientation  $g$  may be described by a rotation that transforms the sample-fixed coordinate system  $K_A$  into the crystal-fixed system  $K_B$  of the crystallite in question (see Figure 2.22). The orientation  $g$  may be described by the Euler angles  $\varphi_1, \phi, \varphi_2$ , or by many other orientation parameters like Miller indices  $(hkl)$   $[uvw]$ .  $g$  is the relationship between two coordinate systems defined in the orientation distribution. One coordinate system is usually fixed in the exterior shape, e.g. normal, transverse and rolling direction in case of rolled sheet. The second coordinate system is fixed in the crystal-axes following the crystal symmetry, e.g.  $[10\bar{1}0]$ ,  $[11\bar{2}0]$  and  $[0001]$  in case of the hexagonal structure. Euler angles are used in this work. Euler angles are defined by rotation angles around 3 fixed axes, from which the crystal coordinate system becomes matched with the sample coordinate system. The crystal coordinate system is firstly rotated about the  $Z'$ -axis through the angle  $\varphi_1$ , secondly about the

X'-axis (in its new orientation) through  $\phi$  and thirdly, once again about the Z'-axis (in its new orientation) through the angle  $\varphi_2$  [BUN93]. Figure 2.22 shows two methods of representing the crystallographic orientation. One is by Miller indices and the other by Euler angles.

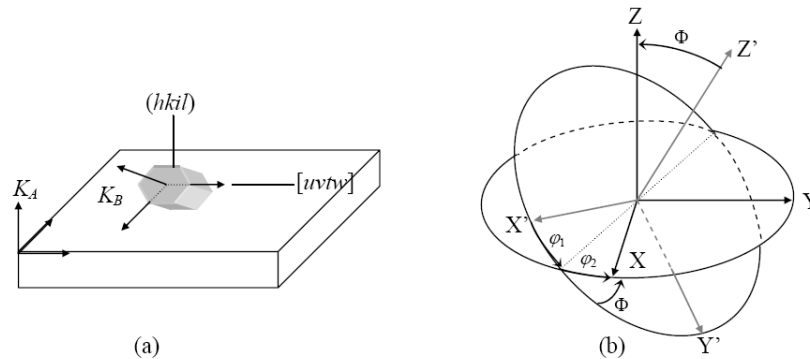


Figure 2.22. Two methods for representing the crystallographic orientation  $g$ : a) Miller indices; b) Euler angles; a coordinate system is presented as Z-axis and its X-Y plane for the sample; Z' and X'-Y' plane for the crystal [Y105].

The pole figure represents the probability of the distribution of the crystals laid in an arbitrary sample direction [Y105]. Figure 2.23 explains the construction of a stereographic projection to represent a pole figure. The orientation of an individual crystallite is defined by the position of its unit cell in space with reference to a coordinate system. In this explanation a cubic material is used, representing the unit cell by a cube. The stereographic projection is obtained by the following procedure:

- The unit cell is located in the origin of the coordinate systems and surrounded by the unit sphere.
- To represent the cube faces in the stereographic projection, the point of intersection of the normal vector of each cube face with the surface of the unit sphere is determined.
- Only the intersections 1, 2 and 3 on the northern hemisphere are taken into account.
- Connecting the points of intersection with the south pole yields the intersecting points 1', 2' and 3' in the equatorial plane.
- They are called poles of the respective cube faces.

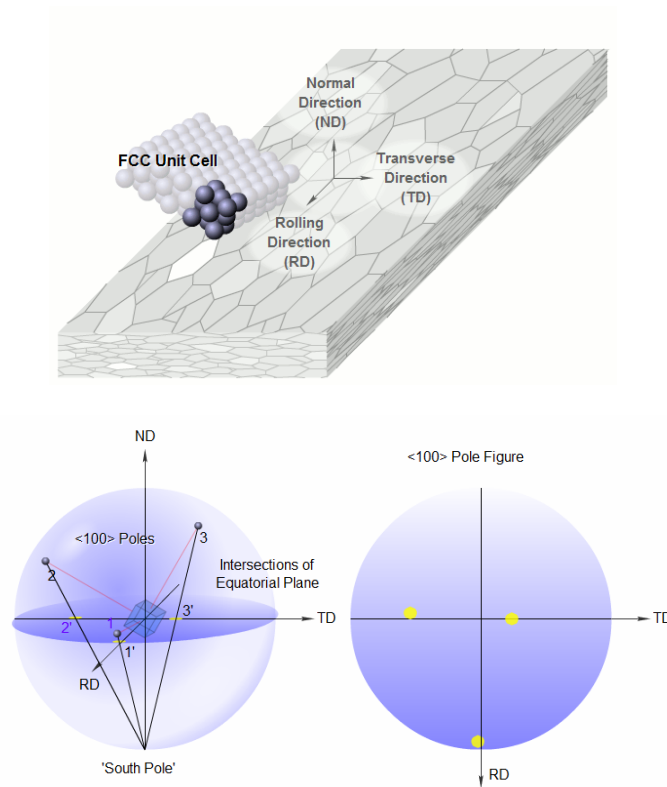


Figure 2.23. Stereographic projection construction of a cubic material [ALU08].

For polycrystalline materials, a set of poles can be plotted for each individual grain to produce a pole figure. If the grains are randomly oriented, then the poles may be distributed evenly over the pole figure. When the grains are not randomly oriented, but tend towards particular orientations, the previously mentioned preferred orientation or crystallographic texture appears. In this case, the poles will be concentrated within certain areas of the pole figure. Figure 2.24 shows the difference between random and preferred texture in the pole figures.

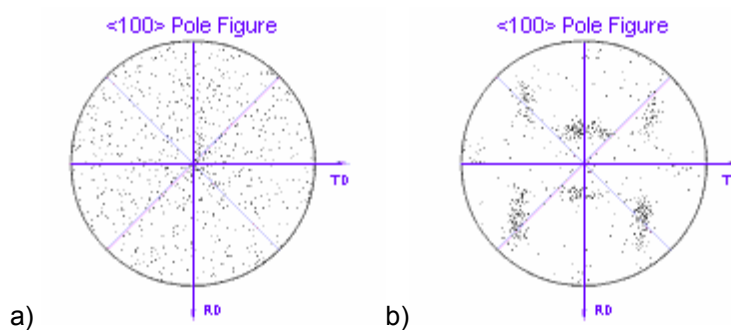


Figure 2.24. Representation of a) random and b) preferred texture in the pole figure [ALU08].

### 2.7.3 Development of texture in magnesium

Since the texture is a key issue for wrought alloys, most of the literature is focused on the study of texture in wrought material. Nevertheless, the theory is applied, in the same way, to cast or wrought alloys, the only difference being the initial texture of the material prior to deformation. In this section,



an introduction of the texture of wrought alloys is given. However, the main point is to explain the texture obtained after tensile and compression testing.

### 2.7.3.1 Texture in wrought materials

It is written [TEN80] that, for hexagonal materials with  $c/a$  ratios approximately equal to the ideal ( $c/a \approx 1.633$ ), such as Mg, the textures are developed with a tendency of basal fibre texture, so called c-type (center-type) (Figure 2.25). In the c-type texture most of the grains have the c-axis perpendicular to the rolling plane. The c-type texture is observed in several works concerning rolling of Mg alloys [PER04a, SOM06, STA03, and VAL03]. Yi [YI05] estimates that the categorization by  $c/a$  ratio is a rather crude approach because many other factors influence the texture development, e.g. strain rate, temperature, chemical composition, etc. Yi in this work reports the presence of t-type and r-type textures in hexagonal materials. In the r-type texture the basal pole splits towards the rolling direction (RD) in the (0002) pole figure and in the t-type towards the transverse direction (TD). The r-type texture has been reported in other works [DUY03, PER04b], where the maximum intensity is displaced from the ideal basal orientation by a rotation around the transverse direction (Figure 2.26).

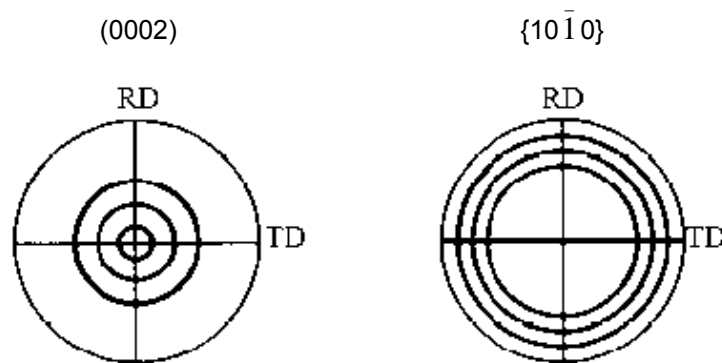


Figure 2.25. Schematic rolling textures in HCP metals with  $c/a$  ratios are approximately equal to the ideal like Mg (c-type) [TEN80]

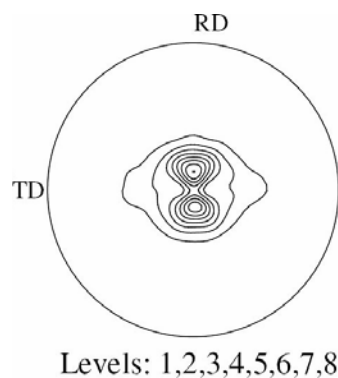


Figure 2.26. (0002) pole figure illustrating the macrotexture of the AM60 alloy after one rolling pass at 375°C with a 80% thickness reduction. r-type texture is observed [PER04b].

### 2.7.3.2 Texture development during tensile testing

It is reported [DUY03, JIA07, LIU06, STA03, WAG06, YI05, YI06] that tensile testing leads to the formation of texture in the  $\{10\bar{1}0\}$  plane perpendicular to the loading direction (LD) and in the  $\langle 10\bar{1}0 \rangle$  direction parallel to LD. Figure 2.27 shows the evolution of the texture during tensile test for a sample machined at  $0^\circ$  to the extrusion direction. In this sample the initial texture is given and the measuring points of the sample during the test are represented in the tensile curve. In the  $0^\circ$  sample only the intensity is slightly changed during tensile testing. In the same work, Yi [YI05] also analyses samples cut at  $45^\circ$  and  $90^\circ$  to the extrusion direction, all of them having a tendency to form the texture in the  $\{10\bar{1}0\}$  plane. In the  $90^\circ$  sample the component  $\{\bar{1}2\bar{1}0\}$  is also present. The maximal intensity ( $P_{max}$ ) of the  $45^\circ$  and  $90^\circ$  samples is about 6.5 m.r.d. in the (0002) pole figure. Thus, it is similar to the  $0^\circ$  sample presented in Figure 2.27.

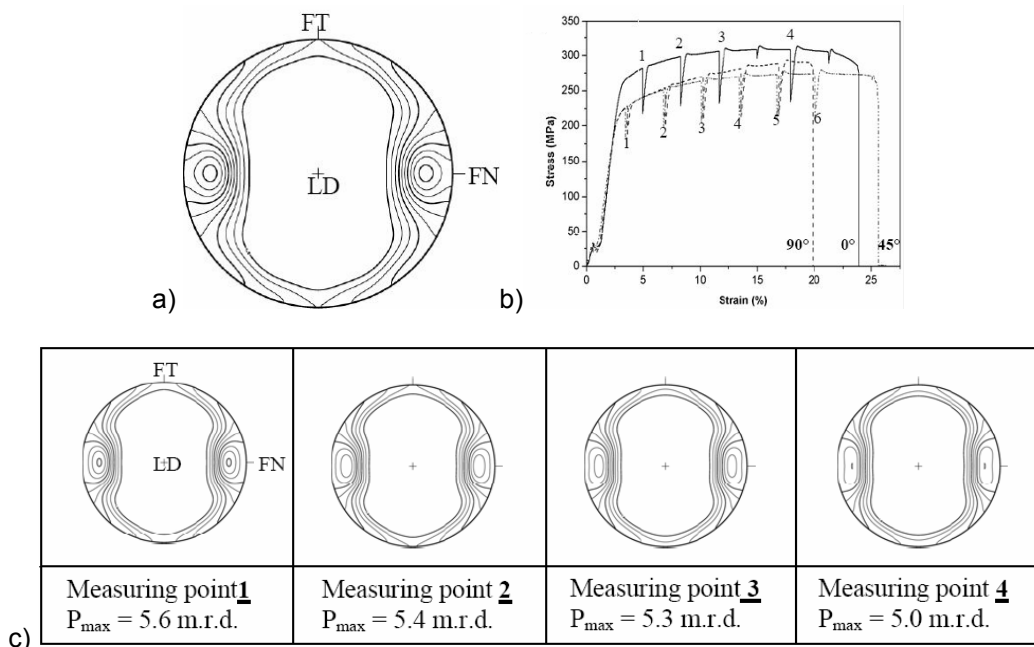


Figure 2.27. a) (0002) pole figure of the  $0^\circ$  tensile sample. FN is the original normal direction after cutting of the sample and FT is the transverse direction of the extruded bar.  $P_{max}=5.7$  m.r.d.; b) the flow curve during tensile test, indicating the in-situ measuring points of the texture. c) variation of the (0002) pole figure during tension of the  $0^\circ$  sample. Level = 1.0, 1.5 ... 5.5 in all the pole figures [YI05].

### 2.7.3.3 Texture development during compression testing

During compression most grains are reoriented so that their c-axes lie parallel to the load axis [JAI07, JIA07, STA03, and WAG06]. Figure 2.28 shows the texture in compression, being a) the undeformed texture and b) and c) the texture after compression in the RD and TD directions. Note that the loading direction in these two is not represented in the centre but in the top-bottom or left-right of the pole figures.

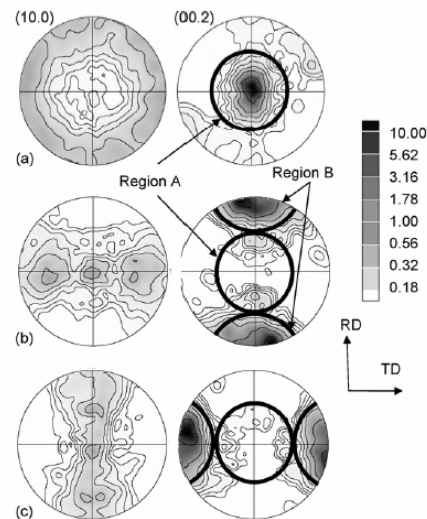


Figure 2.28.  $\{10\bar{1}0\}$  and  $(002)$  pole figures for the a) undeformed; b) compression in the rolling direction, and; c) compression in transverse direction samples. [JAI07].

## 2.8 Summary

A small summary of the models to be used is presented in this section. The models are only related to the sections 2.2 and 2.5 of this chapter, which are used to predict the microstructure and the mechanical properties.

Several solidification models are found in literature, but most of them are complicated to use, mostly in multicomponent alloys. A lot of physical properties of the material have to be measured in order to solve these equations. Therefore, it is not interesting to use them in real applications. The measuring of all the data for every alloy is time consuming and expensive. The selected equations for this study are useful for numerical simulations for example. They are easily introduced in the models and the obtained results give an approximate value of the reality.

In this thesis work Eq. 2.4 defined by Flemings [FLE74] were used for the prediction of the grain size from the solidification time. For the prediction of the tensile yield strength Hall-Petch equation was used (Eq. 2.7). Hall-Petch equation makes the assumption that the material is a single phase polycrystal. When the nature, distribution and amount of precipitates are constant, this equation is valid. When any of them changes, the constants may be calculated again. However, if the casting and heat treatment conditions are similar, these equations are valid and easy to use. In this work it is expected to obtain equations for the commonly used casting and heat treatment conditions. Table 2.6 summarises the equations mentioned above.

Table 2.6. Summary of the selected equations.

<b>Prediction of grain size</b>	$d = a \cdot t_s^n = b \left( \frac{\Delta T_s}{t_s} \right)^{-n}$	Eq. 2.4
<b>Prediction of tensile yield strength</b>	$\sigma_y = \sigma_0 + kd^{-1/2}$	Eq. 2.7

## **CHAPTER 3 - EXPERIMENTAL PROCEDURE**



### 3 EXPERIMENTAL PROCEDURE

In this chapter the experimental procedures are described. The main objective was to increase the knowledge of the prediction of mechanical properties in magnesium castings. In order to analyse the effect of solidification conditions on mechanical properties, a variety of microstructures were obtained using different casting technologies and part geometries. Tensile bars, test-parts and prototypes were cast using sensorised moulds for the acquisition of cooling curves. Later, microstructures, textures and mechanical properties were analysed. The effects of alloying elements in the mechanical properties and in the creation of the texture during deformation were considered for a better understanding of how properties can be improved.

#### 3.1 Casting technology

Four casting technologies were used in this research work: sand-casting, gravity die-casting, investment-casting and high-pressure die-casting (HPDC). The last one, due to the difficulties to insert thermocouples inside the melt, was not considered for establishing the relationship between solidification conditions, microstructures and mechanical properties.

The casting was performed mostly in foundries except for some investment-cast parts which were produced in the installations of Mondragon Goi Eskola Politeknikoa (MGEP). Sand-castings were produced by Stone Foundries Ltd, in London, England. Gravity die-castings and investment-castings were cast by SpecialValimo Oy and by Helsinki University of Technology, both in Espoo, Finland. Finally, HPDC parts were made by Magnesium Research Institute (MRI), in the Dead Sea, Israel and by Fémalk co., in Budapest, Hungary.

The melting procedure for the AZ91E alloy was defined as described by Stone Foundries and employed in all the gravity castings, with the only variation of some commercial products such as grain refiners. The crucibles were preheated to a dull red heat before being dusted by flux and charged with ingots first, then scrap returns progressively. Flux was added in the AZ91E alloy as required to prevent the burning of the metal, and the temperature of the melt was adjusted. After grain refinement, the melt was cleaned from oxides and the casting temperature was fixed. The MRI207S alloy and the HPDC alloys were melted under protection atmosphere of  $\text{CO}_2 + \text{SF}_6$ . Pouring was always completed under protection gas  $\text{CO}_2 + \text{SF}_6$  to avoid the burning of the melt during the casting process. The MRI207S alloy was melted following the indications defined by MRI. Filters were placed in the sand and investment-cast moulds.

MGEP used a similar procedure. A Nabertherm K4/13 tilting melting furnace was used for the melting of Mg. A steel crucible was constructed as recommended for melting magnesium [AVE99], with a capacity of 3.5 l. Figure 3.1 shows the CAD model of it and the crucible built and placed in the furnace. The flux Magrex 60 from FOSECO was used for protection during the melting process. When the melt reached 720-740°C, the grain-refiner powder Nucleant 5000 (FOSECO) was applied. For submerging the grain-refiner inside the melt, it was put inside aluminium foil. Due to the flammability of the grain-refiner, care must be taken in this process. Finally, the oxides were removed from the surface. A

preheated investment-cast mould was placed under the furnace and the casting was completed under protective atmosphere of  $N_2+6\%SF_6$ .

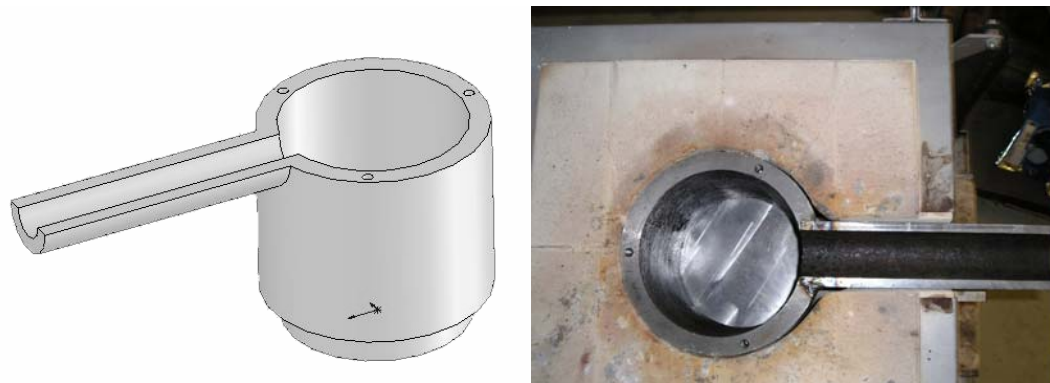


Figure 3.1. The CAD model of the crucible and the crucible constructed and placed in the furnace.

HPDC alloys were originally produced in ingot form and then re-melted and die-cast at the MRI's high-pressure die-casting laboratory using an IDRA cold chamber die casting machine with a 345 t clamping force. The configuration of the HPDC die is shown in Figure 3.2. In this die, apart from two tensile bars, a corrosion bar, a fatigue, a bending and a Charpy sample were obtained. In this work, only the tensile bars are analysed.



Figure 3.2. Configuration of High-Pressure Die-Cast specimens.

HPDC test parts were cast in Fémalk in a cold-chamber die-casting machine under protective atmosphere.

### 3.2 Selected alloys

Two gravity casting alloys were selected along with other three HPDC alloys. All these alloys are summarised in Table 3.1. The AZ91 was the only common alloy for all the technologies. The only difference between the gravity cast AZ91E alloy and the HPDC AZ91D alloys are minor elements in their composition for a better behaviour in each technology.

Table 3.1. Alloys used in each technology.

Technology	AZ91	AM50	AM50+Si+Sn	MRI207S
Sand-casting	X			X
Investment-casting	X			X
Gravity die-casting	X			X
HPDC	X	X	X	



Two gravity casting alloys were used in this study, which are the commercial AZ91E alloy and the new developed MRI207S alloy. The MRI207S alloy is a high strength magnesium alloy which can be suitable for the required mechanical properties of the aerospace industry. The AZ91E alloy was selected because of its high castability and for being the most common alloy in actual applications. Moreover, in order to compare two different kinds of technologies, as are gravity casting and high-pressure casting, this alloy was the most suitable. Other usual high-performance alloys, for example the commercial WE54 alloy, are not possible to cast by HPDC due to their reduced castability. It would lead to the impossibility of comparing the mechanical properties of those different technologies. Another reason for using the AZ91 alloy is because of the literature. Most of the data about Mg-alloys refers to pure Mg or to AZ91. In order to verify the experimental data with literature, AZ91 is the most suitable magnesium casting alloy.

The composition of the gravity cast AZ91E alloy is shown in Table 3.2. The compositions of the HPDC AZ91D and AM50 alloys are also given in the same table. The MRI207S alloy is an alloy based on the Mg-Zn-Zr-Nd-Y-Gd alloying system, but the exact composition of this alloy may not be disclosed due to confidentiality issues. The AM50A alloy was selected as a reference alloy, and a higher strength alloy modified with Si and Sn was developed. This new alloy is called the AM50+Si+Sn alloy in this work and its composition is also kept confidential. These alloys were developed by MRI in the frame of the FP6 European IDEA project. The compositions are confidential until MRI decides to protect them by patents.

Table 3.2. Composition (%wt.) of the AZ91E, AZ91D and AM50A alloys [AVE99].

Alloy	Standard		% Al	% Mn	% Zn	% Si	% Fe max.	% Ni max.	% Cu max.	Other elements
	ASTM	UNS								
AZ91E <sup>a</sup>	B93	M11918	8.1-9.3	0.17-0.35	0.4-1.0	0.20	0.005	0.0010	0.015	0.01 OE <sup>c</sup> 0.30 OT <sup>d</sup>
AZ91D <sup>b</sup>			8.5-9.5	0.17-0.40	0.45-0.9	0.05	0.004	0.001	0.025	0.01
AM50A <sup>b</sup>			4.5-9.5	0.28-0.50	0.20	0.05	0.004	0.001	0.008	0.01

<sup>a</sup> [AVE99]

<sup>b</sup> [DSM08]

<sup>c</sup> max other (each)

<sup>d</sup> max other (total)

### 3.3 Selected geometries

Tensile bars, a test part and some components were cast. Separately cast specimens were cast with optimal parameters to avoid defects like porosity. The purpose of the separately cast tensile specimens was mainly to characterise the material for each casting technology. The test part has changing wall thicknesses, which make it prone to shrinkage. This part is appropriate for optimising casting parameters as well as for having different solidification rates inside one casting. The capability of the technologies can be compared in a same geometry with the test part. Figure 3.3 shows the sand-cast tensile bars and test part. The selected geometry for the prototype is a thin-wall aerospace part, which is at present produced in aluminium. Other two components were also proposed within the IDEA project as possible candidates to substitute aluminium made components by magnesium. These geometries are presented in the introduction of the chapter 6.

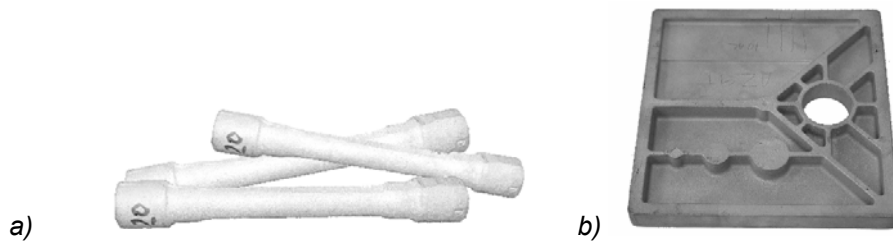


Figure 3.3. Different geometries cast by sand-casting: a) tensile bars; b) test-part.

Half of the cast parts were T6 heat treated for mechanical and microstructural characterisation.

Sand-cast tensile bars were slightly machined before tensile testing to avoid the influence of the surface roughness in the mechanical properties. Tensile bars were excised from the test-part and samples for metallographic examination were taken from several locations of this part.

For simplicity for further references, Table 3.3 introduces all the gravity cast samples in this work. This table also describes the nomenclature utilised later in this document. It also states whether cooling curves were measured for each casting family and the origin of the castings.

Table 3.3. Summary of the gravity cast samples and the utilised nomenclature.

Casting Technology	Part geometry <sup>a</sup>			Alloy		Nomenclature <sup>b</sup>	Cooling curves
	T	P	C	AZ91E	MRI207S		
Sand-casting (foundry)	X			X		TSFA	No
	X				X	TSFM	No
		X		X		PSFA	Yes
		X			X	PSFM	Yes
Investment-casting (foundry)	X			X		TIFA	No
	X				X	TIFM	No
		X		X		PIFA	Yes
		X			X	PIFM	Yes
Investment-casting (MGEP)	X			X		TIMA	Yes
			X	X		CIMA	Yes
Gravity die-casting (foundry)	X			X		TGFA	No
	X				X	TGFM	No
		X		X		PGFA	Yes
		X			X	PGFM	Yes

<sup>a</sup> T: Tensile bar; P: Test part; C: Component

<sup>b</sup> The nomenclature of the castings is composed by the first letter meaning the kind of geometry (T: tensile bar, P: test part, C: component or prototype). The second letter means the casting technology (S: sand-casting, I: investment-casting, G: gravity die-casting). The third letter signifies the place of casting (F: foundry, M: MGEP) and the last letter means the cast alloy (A: AZ91E, M: MRI207S). The foundries were Stone Foundries Ltd., England, for sand-cast parts and SpecialValimo J. Pap Oy, Finland for gravity and investment-cast parts.

The geometries of separately cast tensile bars were different for each technology in order to have the optimum properties in each technology. A single geometry was defined for tensile bars machined from the test parts. The test parts, being of the same geometry, will allow us to compare different technologies.

Most of the geometries were defined using the standards of ASTM. Tensile specimens were dimensioned following the standard ASTM E8-M [AST03], except sand-casting, where dimensions were defined with an English standard used by Stone Foundries for tensile testing. Sand-cast tensile bars were slightly machined, but tensile bars produced by the other three technologies were tested without any machining. The main reason is to avoid the influence of the roughness of the as-cast surface in the testing of the sand-cast tensile specimens, while other technologies, with a better surface finishing do not need machining. On the other hand, machining can be harmful, deteriorating, for example, the properties of HPDC parts. The fine grained skin typical in HPDC is considered to be responsible for increasing the strength of the alloys. The dimensions of HPDC tensile samples are shown in Figure 3.4a, gravity die-cast tensile specimens in Figure 3.4b, investment-cast samples in Figure 3.4c and sand-cast tensile specimens in Figure 3.4d.

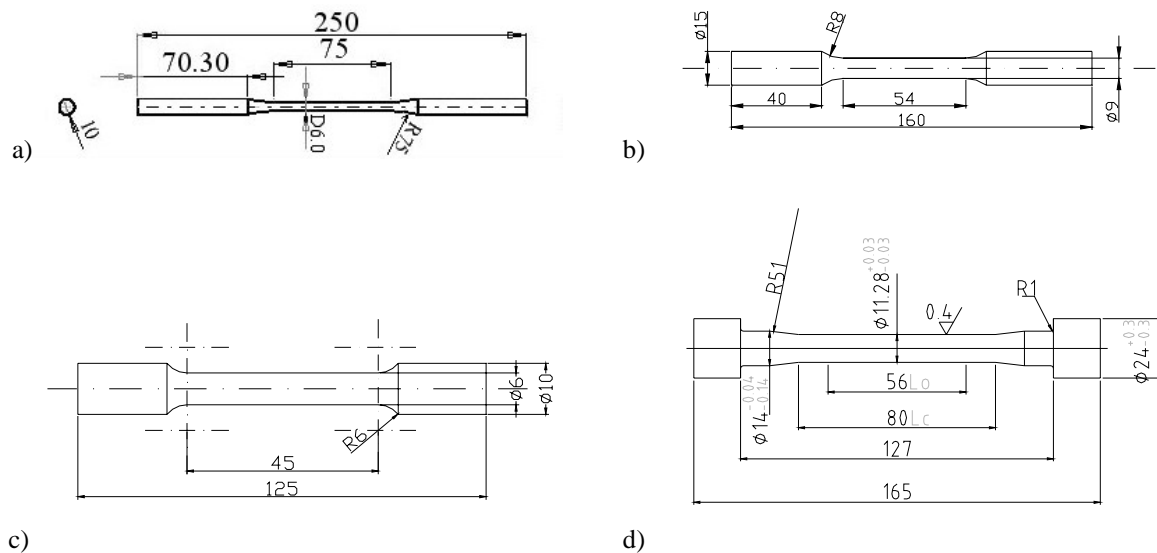


Figure 3.4. a) Tensile bar for HPDC; b) for gravity die-casting; and c) for investment-casting; d) machined sand-cast tensile sample.

The maximum dimensions of the test parts (Figure 3.5) were  $200 \times 200 \times 20 \text{ mm}^3$ . This test plate, with its combination of different thicknesses and shapes, is adequate for producing different microstructures together with variable porosity levels inside the casting. The right side of the casting has thicknesses of up to 13 mm in the thick area, and the right side is dominated with a 4 mm thick area with some massive cylinders where the porosity should be concentrated. The upper side of the part is composed with an empty area in the centre with ribs around. The test part, apart for mechanical and microstructural characterisation, serve to obtain cooling curves at different positions.

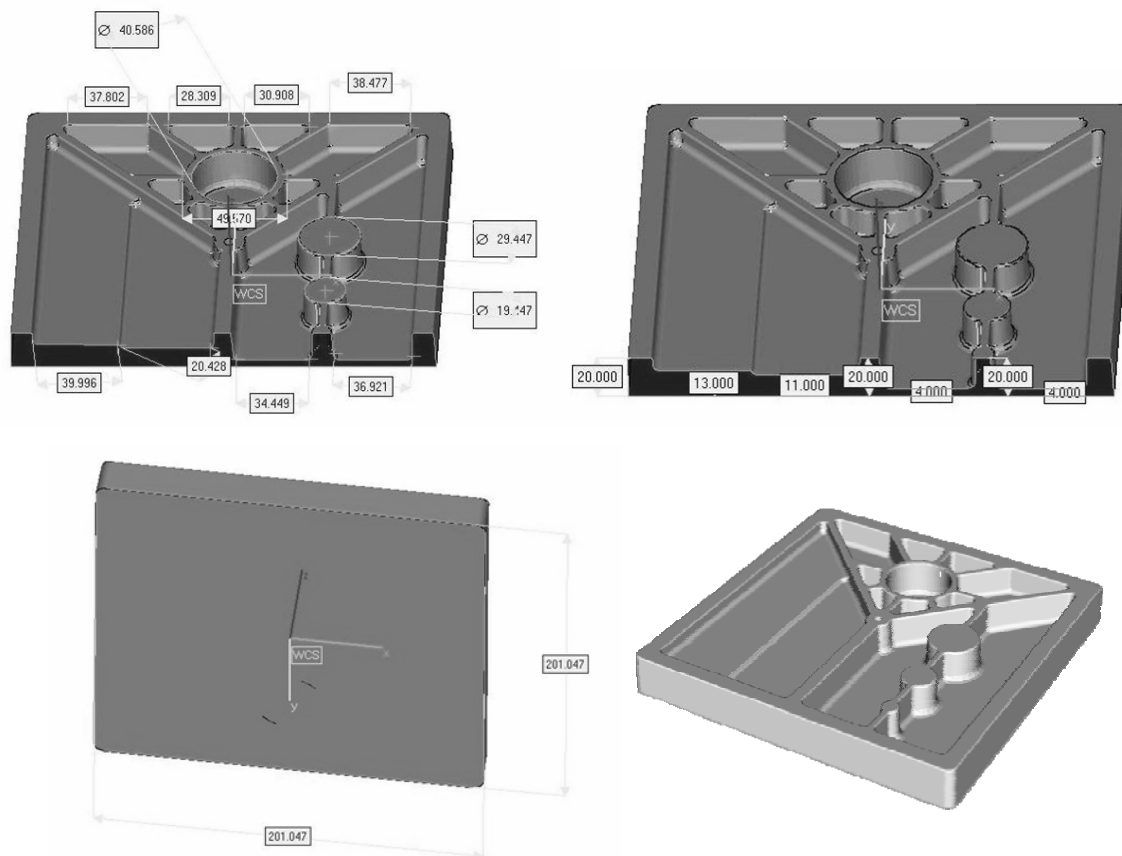


Figure 3.5. CAD model of the test part.

A component was also cast for the acquisition of cooling curves. The component was a thin-wall aerospace part, actually produced in aluminium. This part is shown in Figure 3.6, with maximum dimensions of 900x45x45 mm<sup>3</sup> and 2.5 mm of thickness. The parts were not used for further characterisation of the material.



Figure 3.6. CAD model of the prototype.

### 3.4 Acquisition of cooling curves

Cooling curves were measured placing K-type thermocouples (chromel-alumel) inside the moulds at different locations and temperatures were recorded from the casting up to the solidification of the alloy. DaqView<sup>®</sup> data-acquisition software was used for the registering of the data, using time-steps of 0.1 s.

Thermocouples were placed in different positions of the casting. Different positions mean different cooling curves, and it is more pronounced in parts like the selected test part due to its differences in thickness. The different solidification times will lead to a variety of microstructures inside the casting, which will be used for setting correlations between solidification times and microstructures. Figure 3.7 describes where thermocouples were placed inside the test part. Figure 3.8 describes the positions of the thermocouples inside the moulds that were investment-cast in MGEP. Figure 3.8a shows the investment-cast tensile bars with the gating and running systems and in Figure 3.8b the positions in the prototype mould are marked.

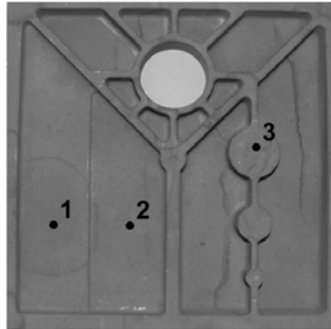


Figure 3.7. Positions for the thermocouples placed inside the test part.

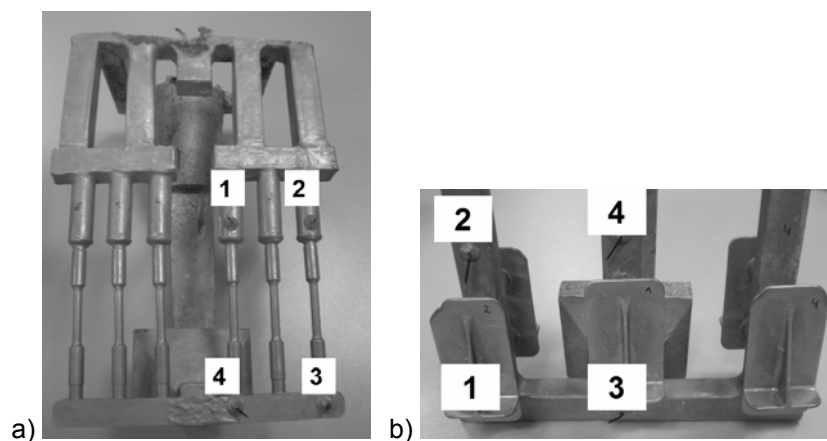


Figure 3.8. Positions for the thermocouples placed in the investment-cast parts: a) placements in the mould for casting tensile bars; b) placement of the thermocouples in the mould of the prototypes.

### 3.5 Heat treatment

The microstructure and mechanical properties of AZ91E and MRI207S alloys were characterised in as-cast and heat-treated conditions. The heat-treatment applied to both alloys was solution heat treatment and subsequent artificial aging (T6). AZ91E was T6 treated as follows: 385°C for 8 hours plus 415°C for 16 hours (under protective atmosphere of CO<sub>2</sub>+2%SF<sub>6</sub>), water quenched (65-85°C) and aged at 165°C for 16 hours. An accelerated T6 heat treatment developed by MRI was applied to MRI207S alloy.

No heat treatment was applied to the HPDC alloys.

### 3.6 Microstructural analysis

The preparation of samples consisted of grinding passes of 2 min each on SiC-papers of grit 800, 1200, 2500 and optionally 4000. Subsequently, samples were polished using OPS or alumina with a particle size of 0.05  $\mu\text{m}$ . When automatic polishing was used, 6 samples were prepared together at a pressure of 1.8 bars. The disc rotated at 280 rpm and 2 min time was applied for each grinding step and at 180 rpm during 7 min for polishing.

For grain size measurement of the AZ91E alloy, samples were solution heat treated prior to metallographic preparation. Standard practice dictates that Mg-Al alloys should undergo a solution treatment of 12 hours at 410°C [CAR97]. Otherwise, the problem for grain size measurement in as-cast conditions is the dendritic morphology, which makes it difficult to distinguish the grains. On the other hand, after complete T6 heat treatment, large areas of eutectic appear in the microstructure, and grain size measurement is influenced by the presence of two structures. Therefore, these two structures should be counted separately or the eutectic phase should be resolubilised in order to have a single phase. That is the reason why both as-cast and T6 heat treated grain sizes were measured after a solution heat treatment of 12 hours at 410°C under protective atmosphere of Ar. It has been reported [BUS45] that an approximate 13.5% increase of grain size may occur due to the annealing. However, the possible grain growth due to the solution treatment was not taken into account because it was considered a systematic error in all the AZ91E grain size measurements. All the measurements were made after the same solution treatment, so the grain size should be proportional in all of them, and therefore, the results comparable.

The AZ91D, AM50, AM50+Si+Sn and MRI207S samples were etched in a solution of 5 ml acetic acid, 6 g picric acid, 10 ml H<sub>2</sub>O and 100 ml ethanol (98%). The AZ91E alloy in as-cast and T6 heat treated conditions were etched using a solution of 30 ml distilled water, 25 ml acetic acid, 50 ml ethanol, 60 ml ethylene glycol, 1-2 ml nitric acid and 3 g of picric acid. The reason for using this etchant was to have a soft etching in the eutectic, given that the usual etchant produces an excessive etching in the lamellar eutectic. The AZ91E solubilised samples for grain size measurement were etched using a solution of 60 ml distilled water, 50 ml acetic acid, 100 ml ethanol, 120 ml ethylene glycol, 2 ml nitric acid and 2 g of picric acid. This etchant allows a good definition of grain boundaries in the solubilised AZ91E alloy. All these etchants are summarised in Table 3.4.

Table 3.4. Metallographic etchants used for Mg alloys.

Etchant	Alloy	Formula	Application
Etchant 1 Acetic picral [AVE99]	MRI207S, AZ91D, AM50 and AM50+Si+Sn	5 ml acetic acid, 6 g picric acid, 10 ml H <sub>2</sub> O and 100 ml ethanol (98%)	Highlights general structure
Etchant 2	AZ91E-F and AZ91E- T6	30 ml distilled water, 25 ml acetic acid, 50 ml ethanol, 60 ml ethylene glycol, 1- 2 ml nitric acid and 3 g of picric acid	The same as etchant 1 but softer for better demonstration of the eutectic phase
Etchant 3	AZ91E after solubilisation	60 ml distilled water, 50 ml acetic acid, 100 ml ethanol, 120 ml ethylene glycol, 2 ml nitric acid and 2 g of picric acid	The same as etchant 1 but softer for the $\alpha$ -Mg matrix and capable of showing the grain boundaries of solubilised AZ91E alloy

Grain size was measured with the average linear intercept method described in the standard ASTM E112 [AST96] using optical microscopy. Both the average linear grain size ( $d$ ) and the ASTM grain size number,  $G$ , are reported in this document.

Porosity was measured in as-cast samples (without heat-treatment) using the image analysis technique. Surfaces were polished and no etching was applied.

Secondary and backscattering electron microscopy with EDX was used for the analysis of the precipitates. Transmission Electron Microscopy (TEM) was employed for the analysis of HPDC tensile bars for checking the deformation mechanisms that are present during testing. Samples for TEM were prepared using ion-mill technique.

### 3.7 Texture Analysis Using Neutron Diffraction

The texture is formed when there is a preferred orientation of the grains in a polycrystalline material. There is usually a random texture in castings. Texture is formed when the material is deformed, such as in uniaxial deformation. The reason to measure texture is to identify if there is any influence of the alloying elements in the formation of the texture in high-pressure die-castings.

Several techniques can be used for texture measurements, such as synchrotron sources, visible light, neutrons and electrons [BUN89]. In this thesis, the neutron diffraction method was selected because of its capacity to measure global texture with high penetration depth instead of measurements in local or small areas. Schäfer [SCH68] also states that more accurate pole figures are obtained by neutrons than those obtained by X-rays.

The high-cooling rate generates a small grain size on the surface of high-pressure die-castings and the microstructure is inhomogeneous, with a fine grain skin and a coarser grain interior. The difference on grain size may also cause an inhomogeneity in the texture. The objective of this work is to measure

the change of the global behaviour of the different alloys. Hence, the texture on a macro scale is needed, which is obtained directly by neutrons.

### 3.7.1 *The utility of neutrons*

Intense neutron beams have a diverse potential for industrial applications and materials research. For this purpose, a variety of thermal neutron techniques have been established. The materials under examination are often complex, such as oils, welds, engines, etc., and these often experience harsh chemical, mechanical, thermal, and processing environments. Under such conditions, thermal neutrons are well suited to perform in situ measurements. Their high penetrating power, up to several centimetres, makes neutrons also particularly well suited for non-destructive testing of real materials and components in their as-fabricated or in-service condition.

The most important applications of thermal neutrons are listed below [ASM86]:

- Determination of atomic arrangements (for example, crystal structure, short- and long-range order), especially for structures containing light (low atomic number) atoms in the presence of heavier atoms or neighbouring elements
- Determination of magnetic structures
- Determination of structural changes as a function of temperature, pressure, magnetic field, etc.
- Quantitative analysis of multiphase materials
- Determination of residual stress and texture in polycrystalline engineering materials

### 3.7.2 *Lattice Strain Determination*

The neutron diffraction technique for lattice strain characterisation in crystalline materials is based on Bragg's law given by Eq. 3.1

$$n\lambda = 2d_{hkl} \sin \theta \quad \text{Eq. 3.1}$$

where  $\lambda$  is the neutron wavelength,  $d_{hkl}$  is the lattice plane spacing of a selected  $hkl$  reflection and  $\theta$  is half the diffraction angle. Monochromatic neutron diffraction obeys the same Bragg's Law of diffraction as X-rays, being the difference that neutrons diffract from atomic nuclei rather than orbiting electrons [EDI75, SWI04].

$n$  (reflection order) appears because of the periodicity of the wave and can be any positive integer. Figure 3.9 illustrates Bragg's Law for the reflection orders  $n = 1, 2, 3$ .



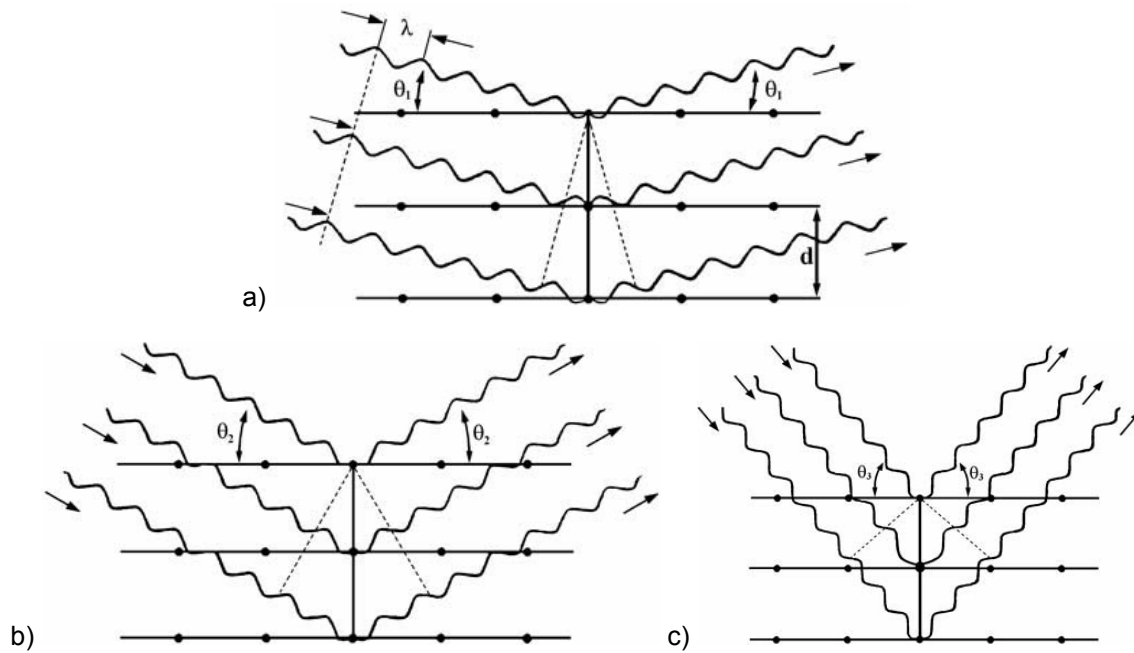


Figure 3.9. Schematic of concept of neutron diffraction according to Bragg's law; a) 1<sup>st</sup> order reflection:  $\lambda = 2d \sin \theta_1$ ; b) 2<sup>nd</sup> order reflection:  $2\lambda = 2d \sin \theta_2$ ; c) 3<sup>rd</sup> order reflection:  $3\lambda = 2d \sin \theta_3$  [BRU08].

Swift [SWI04] explains as follows the application of Bragg's law for the case of monochromatic diffraction. Basically, a beam of neutrons strikes a sample and is diffracted from the crystal planes within the sample. For each crystal plane of different orientation (or composition or structure for multiphase materials) within a polycrystalline sample, the neutron beam will require a different angle to diffract and be detected. Thus, for a single wavelength neutron source, the incident angle (and thus diffraction angle) is altered by rotating the sample with respect to the incident beam, which itself cannot move and always admits the beam from the same direction. Therefore, for the case of monochromatic diffraction, the only unknown is  $d$ , while  $\lambda$  is fixed and known, and  $\theta$  is known but varied and controlled.

### 3.7.3 Experimental Set-Up

In this work neutron diffraction has been used for texture measurements in uniaxially deformed HPDC cast samples. Two alloys were measured without any deformation and after fracture in order to establish the influence of the alloying elements in the formation of the texture. Tensile testing was used as the deformation method. Some samples were deformed at 1%, 5%, 10%, 15% and up until fracture for the texture measurement. When deformation levels of 1%, 5%, 10% and 15% were reached, some tests were stopped in order to measure the texture at these deformation levels. The texture measured at different levels of deformation gives an idea of how the texture is formed in HPDC under uniaxial deformation.

The tests were performed in the Stress-Spec instrument in the FRM-II in Munich [FRM08]. The Materials Science Diffractometer STRESS-SPEC is located at the thermal beam port SR3 of FRM II and can easily be configured either for texture or stress analysis. The set-up utilises three different monochromators: Ge (511), bent silicon Si (400) and pyrolytic graphite (002) (PG). This selection of

monochromators and the possibility of varying automatically the take-off angles from  $2\theta_M = 30^\circ$  to  $120^\circ$  allows us to find a good compromise between the resolution and intensity for each measuring problem. Figure 3.10 describes the Stress-Spec instrument at FRM-II in Munich, Germany.

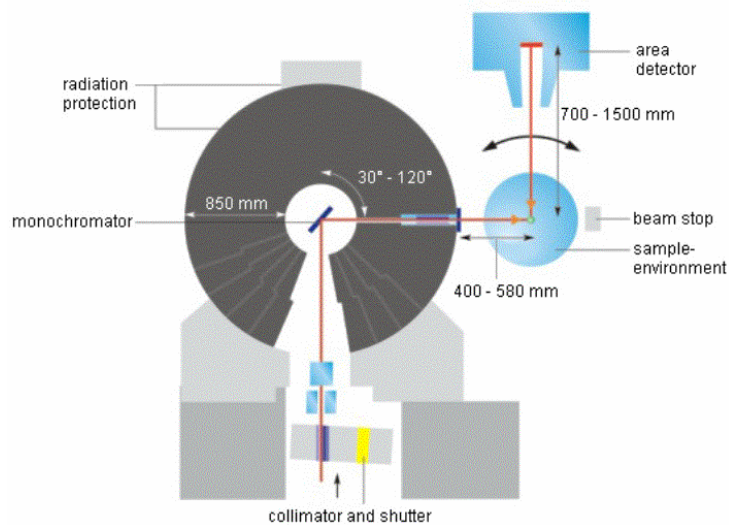


Figure 3.10. Representation of the Stress-Spec instrument at FRM-II [FRM08].

Figure 3.11, on the other hand, shows a picture of the set-up used in the texture measurements performed in this work. A PG-monochromator was used for the measurements and a distance of 800 mm between the sample and the detector. Samples were mounted in a pin to ease their positioning. Two diffraction angle ranges,  $2\theta$ , were chosen for the texture measurements. The first range at  $2\theta = 35^\circ$  includes the diffraction peaks  $(10\bar{1}0)$ ,  $(0002)$  and  $(10\bar{1}1)$ . The second range at  $2\theta = 67^\circ$  includes the peaks  $(11\bar{2}0)$  and  $(10\bar{1}3)$ . The measuring time was controlled through a fixed number of neutron counts for one measuring point.

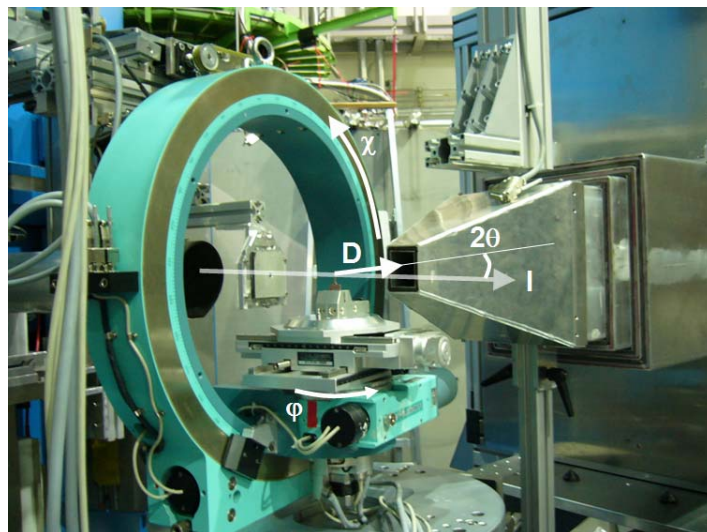


Figure 3.11. The set up in the Stress-Spec instrument at FRM-II.

### 3.8 Mechanical characterisation

#### 3.8.1 Tensile testing

The geometries of tensile specimens are explained in section 3.3 of this chapter and shown in Figure 3.12. As already explained, the dimensions are defined by ASTM standards except sand-cast tensile bars. For more information check the section on selected geometries.



Figure 3.12. Tensile bars cast in this work by HPDC, sand, investment and gravity die-casting.

Moreover, four tensile samples were excised from the indicated positions of the test parts (Figure 3.13). The geometry of the machined samples was the same as the geometry described in Figure 3.4c already presented.

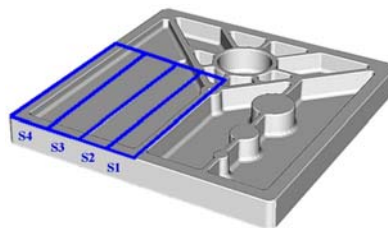


Figure 3.13. Positions for excising tensile bars from the test part.

Tensile tests were performed in an INSTRON 4206 testing machine in MGEP, with a first speed of the moving crosshead of 0.2 mm/min up to offset yield 0.4% and then switching to 0.5 mm/min (strain rate of  $1.5 \cdot 10^{-4} \text{ s}^{-1}$ ) for HPDC, gravity die-cast and sand-cast tensile bars, where an extensometer of gauge length of 50 mm was used. 0.1 mm/min and 0.25 mm/min crosshead speeds were used for investment-cast tensile bars and samples machined out from the test parts, where tests were performed with an extensometer of 25 mm.

#### 3.8.2 Hardness measurements

Finally, Vickers hardness measurements were performed. The hardness of the  $\alpha$ -Mg matrix and the lamellar structure composed by the  $\alpha$ -Mg and  $\gamma$ -Al<sub>12</sub>Mg<sub>17</sub> phases in the AZ91E alloy were measured. The objective was to quantify the influence of those two structures in the mechanical properties. First, the solidification times and/or the time of the eutectic reaction would be related to the quantity of precipitation and its hardness, and then, the quantity and hardness of them would be integrated in the equations for the prediction of mechanical properties.

Different precipitates generate a change in the hardness and consequently, a change in the mechanical properties. The microstructure of AZ91E-T6 is composed by two mayor structures, which are a magnesium matrix and a pearlitic lamellar structure, as it is shown in Figure 3.14. The idea is to identify the hardness of both structures, to quantify the percentage of lamellar structure generated in

different zones and finally, to establish correlations of the precipitates with the mechanical properties. This way, the effect of the precipitates in the mechanical properties could be integrated in the correlations between microstructure and mechanical properties. As it is discussed in the literature review, Hall-Petch equation is valid for a single phase material. In those materials, where more than one phase is present, the parameters of the equation should be modified with the morphology of the precipitates. This was a first attempt to integrate the effect of the precipitates in a more precise manner in such relationships.

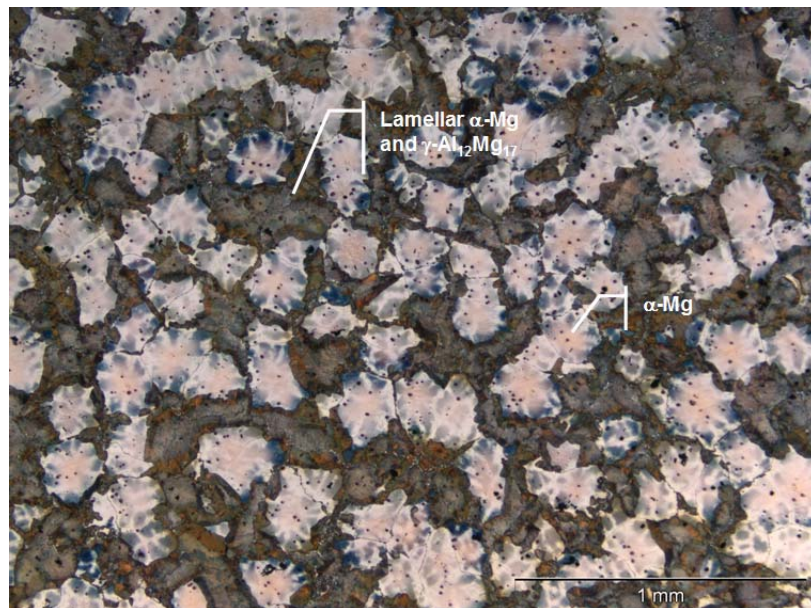


*Figure 3.14. Microstructure of the AZ91E alloy showing two main phases:  $\alpha$ -Mg and lamellar  $\alpha$ -Mg and  $\gamma$ - $Al_{12}Mg_{17}$  (TSFA)*

Vickers hardness was measured using a diamond indenter with the shape of a square-based pyramid with an angle of  $136^\circ$  between opposite faces ( $22^\circ$  between the indenter face and the surface of the material).

Vickers Pyramid Number (HV) can be expressed by Eq. 3.2

$$HV = \frac{1.854F}{d^2} \quad \text{Eq. 3.2}$$

where  $F$  is the force applied to the diamond and  $d$  the average length of the diagonal left by the indenter.

**CHAPTER 4 - CASTING AND SOLIDIFICATION OF MAGNESIUM  
ALLOYS**



## 4 CASTING AND SOLIDIFICATION OF MAGNESIUM ALLOYS

The main objective of the work described in this chapter is to analyse the cooling behaviour of the magnesium alloys. Microstructures, and therefore, mechanical properties, are dependent upon the alloy and the local solidification times in castings. Solidification times are calculated using cooling curves.

Four casting technologies, sand casting, investment casting, gravity die-casting and high-pressure die-casting were considered for producing a variety of castings. The most relevant result of this chapter is the acquisition of cooling curves, along with an explanation of the encountered difficulties to obtain sound parts. Solidification times and cooling rates are measured from these cooling curves for the AZ91E (Mg-Al system) and the MRI207S (Mg-Zn-RE system) alloys.

Moreover, an overview of the high-pressure die-casting trials is given in a separate section. The differences between gravity-casting technologies and HPDC are too large, gravity casting being closer to equilibrium solidification than HPDC. Therefore, the morphology and the distribution of the precipitates are very different. Another divergence is that high-strength alloys, not containing aluminium, are not castable by HPDC. Therefore, it was decided not to analyse this technology with respect to gravity casting technologies.

### 4.1 Casting of gravity Mg-parts

Tensile bars, test parts and prototypes were produced in foundries and in MGEP. Three different technologies were employed in gravity casting, which are sand, investment and gravity die-casting. Two magnesium alloys were cast, which are the AZ91E and MRI207S alloys. Figure 4.1 shows the different parts produced for this work. More information about the cast geometries is presented in chapter 3, in the description of the experimental procedure.

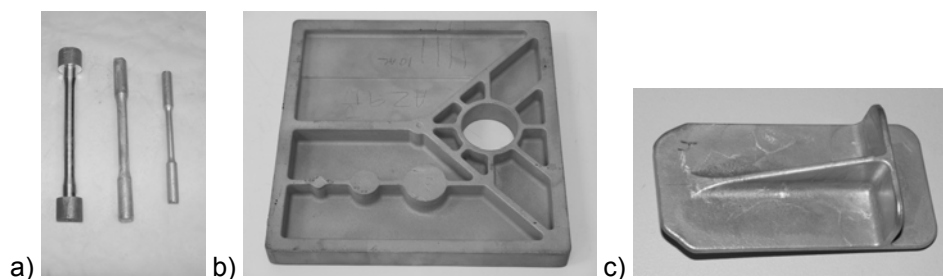


Figure 4.1. Magnesium parts cast in this work: a) tensile bars; b) test part; c) prototype.

This section is divided in two parts. The first one is dedicated to the casting of the samples in the foundries, and then to the casting of the parts in MGEP. This separation is done mainly because the part made in the foundries was not directly controlled. Casting parameters were established by the foundry and only the results are available for this study. On the contrary, the casting procedure and parameters employed in MGEP were designed in the frame of this study.



#### 4.1.1 Casting of Mg-parts in the foundries

For each casting technology the process was optimised until sound castings were obtained. Figure 4.2 shows the casting of the investment-cast bars (TIFM) in SpecialValimo S. Pap Oy Foundry.



Figure 4.2. Pouring of MRI207S to an investment casting mould (TIFM).

The main defects encountered during the production of the test-parts were misruns, internal oxides and porosity. For example, the thin area of the investment-cast test part (PIFA and PIFM) shown in Figure 4.3 presents misruns. This is due to the faster cooling of the melt in this area. When the cooling melt reaches its mushy zone due to a faster cooling rate, the viscosity increases. Therefore, the filling velocity in colder areas decreases, generating incomplete filling. It was observed that small variations in the process, such as lower melt or mould temperature, lower surrounding air temperature, variation in filling time, different alloy, variations in mould structure, and so on cause visible problems in the thin areas.

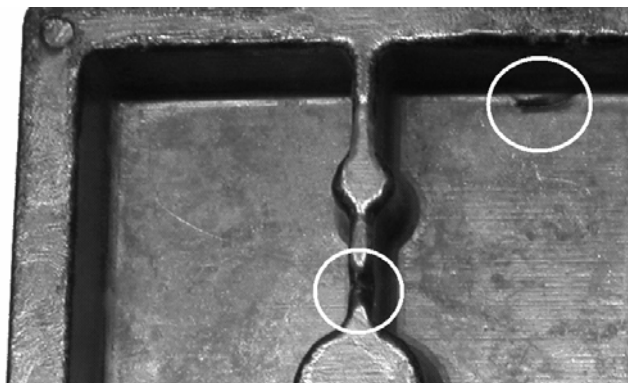


Figure 4.3. Small visible defect area in a test-part (PIFM).

Another encountered problem was the presence of porosity, oxides and impurities inside the castings. These defects decreased the mechanical properties. Figure 4.4 shows one of the clearest examples of bad quality samples encountered after tensile testing.



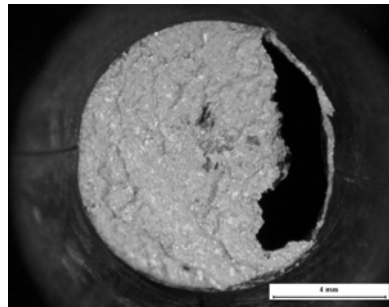


Figure 4.4. Porosity and internal oxidation encountered in some investment-casting test parts after fracture (TIFA).

However, after some optimisation process, the castings were sound and good mechanical properties were obtained in most cases. Some exceptions were the AZ91E gravity die-cast tensile samples (TGFA), where mechanical properties were low due to a high presence of oxides. The exceptions are explained further in chapter 6 when the mechanical properties are given.

#### 4.1.2 Investment-casting of Mg-parts in MGEP

Tensile bars and prototypes were produced in MGEP with the AZ91E alloy. In this section solutions to filling problems, presence of oxides, melt protection and grain refinement are discussed.

When producing investment-cast parts in MGEP, one of the first problems encountered was the incomplete filling of the casting. Using simulation tools for optimising parameters, it was concluded that the main reason was the long filling time. Another crucible was then constructed with a bigger crucible mouth and the filling time was reduced from the initial 25-30 s to 9-10 s. In this manner, the filling problem was solved (Figure 4.5).

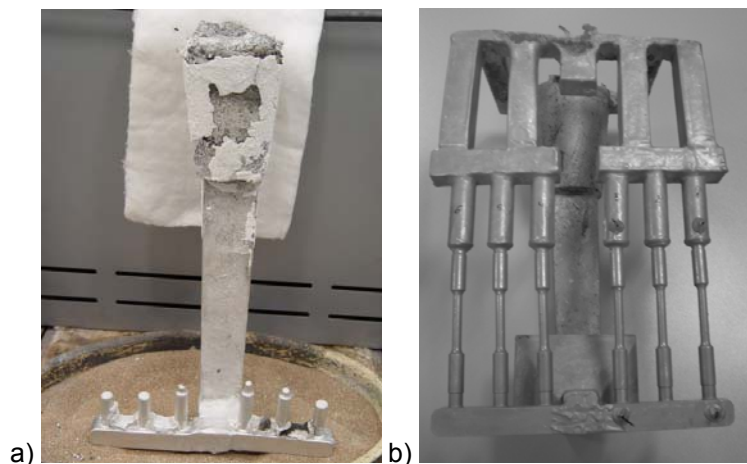


Figure 4.5. a) Incomplete filling of the mould in the first trials with the old crucible; b) Complete filling of the mould with the new crucible (TIMA).

Another main objective was to avoid internal and surface oxidation. A filter was placed in the feeding system to catch impurities. However, it was concluded that the melt temperature is a key factor for avoiding oxidation. Problems with internal oxidation were solved when melt temperature was reduced from 760°C to 720°C. Surface oxidation also disappeared with a melt temperature of 720°C and using ceramic shells with the first layer of alumina. This first layer of the shell is important, as mentioned by

Cingi [CIN06]. When aluminium oxide ( $\text{Al}_2\text{O}_3$ ) was used, little or no oxidation was observed in the surface of the castings. On the contrary, surface oxidation was common in commercially used colloidal silica ( $\text{SiO}_2$ ) ceramics (Figure 4.6).

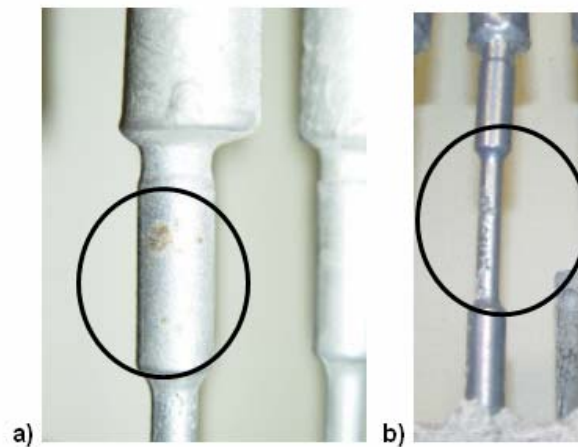


Figure 4.6. a) Isolated oxides in aluminium oxide moulds; b) Oxides distributed in the longitudinal area of the sample in moulds made by colloidal silica.

Another important factor for reducing surface oxidation is the use of inhibitors. The inhibitor mainly used is  $\text{SF}_6$ . In these experiments, a mixture of  $\text{N}_2 + \text{SF}_6$  was used for protecting the melt during the casting process. The mould was filled with this gas and metal was also protected while pouring. The  $\text{NaBF}_4$  inhibitor was impregnated in the moulds to avoid surface oxidation.  $\text{NaBF}_4$  is a liquid inhibitor producing  $\text{BF}_3$  protection gas when heated at temperatures higher than  $384^\circ\text{C}$  [CIN06]. When no protection was used high oxidation levels were encountered in the castings.

Another factor to be analysed was the importance of the use of grain refiners. A test without any addition of grain refiner to the AZ91E alloy was performed. An extremely brittle material was the result. The material broke down when solidifying, and microstructural analysis showed long dendrites where needles from the brittle  $\gamma$ - $\text{Al}_{12}\text{Mg}_{17}$  phase were present inside the grains as shown in Figure 4.7 and Figure 4.8.

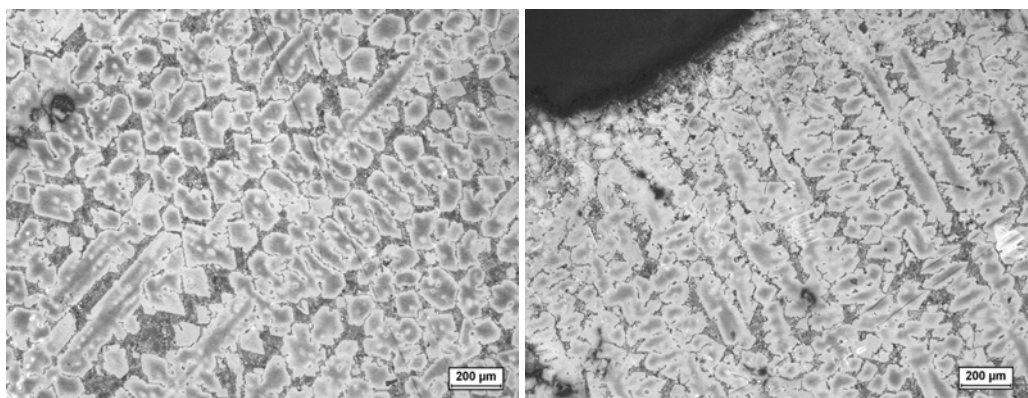


Figure 4.7. Long dendrite arms encountered when no grain refiner was used.

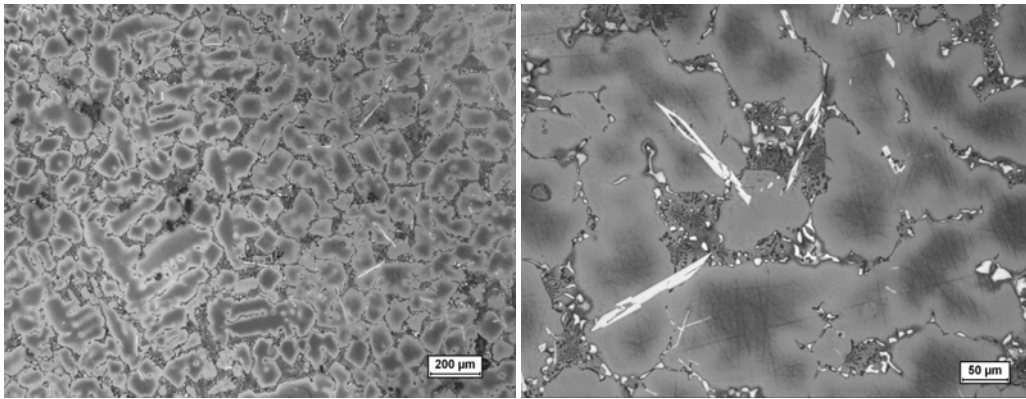


Figure 4.8. Needles of the brittle phase  $\gamma$ - $Al_{12}Mg_{17}$  distributed in the microstructure.

Therefore, the use of grain refiners is required for the AZ91E alloy.

Once the casting parameters and procedure were established, cooling curves were measured and analysed. These cooling curves are explained in the next section together with the cooling curves measured in the foundries.

#### 4.2 Cooling curves in gravity-cast parts

Cooling curves were measured for the different technologies in order to establish a relationship between local solidification times and microstructure. Several control points were defined in the test part and in the castings performed in MGEP. The placement of the control points is described in chapter 3 and in Figure 4.9.

Test parts of the AZ91E and the MRI207S alloys were produced in the foundries. In the experiments in MGEP, only the AZ91E alloy was cast. Figure 4.9 shows the measured curves in the sand-cast test part for the AZ91E alloy (PSFA) and Figure 4.10 for the sand-cast MRI207S (PSFM) alloy as examples of cooling curves. Figure 4.11 is the measured cooling curve of the AZ91E test-part (TIMA) cast in MGEP and Figure 4.12, of the AZ91E component (CIMA), also cast in MGEP.

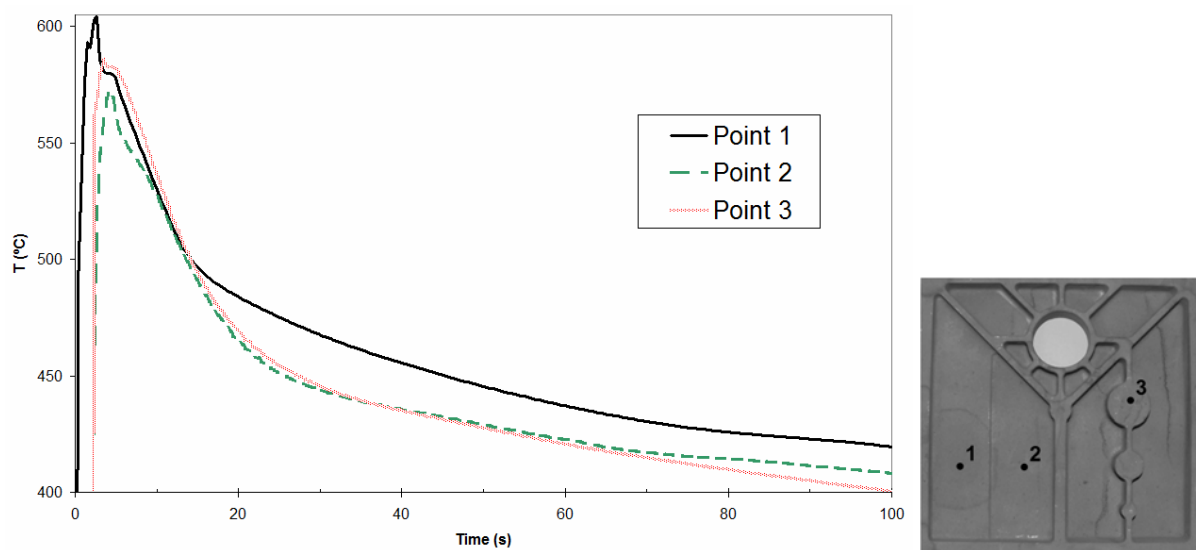


Figure 4.9. Measured cooling curves at the indicated points in the AZ91E sand-cast test part (PSFA).

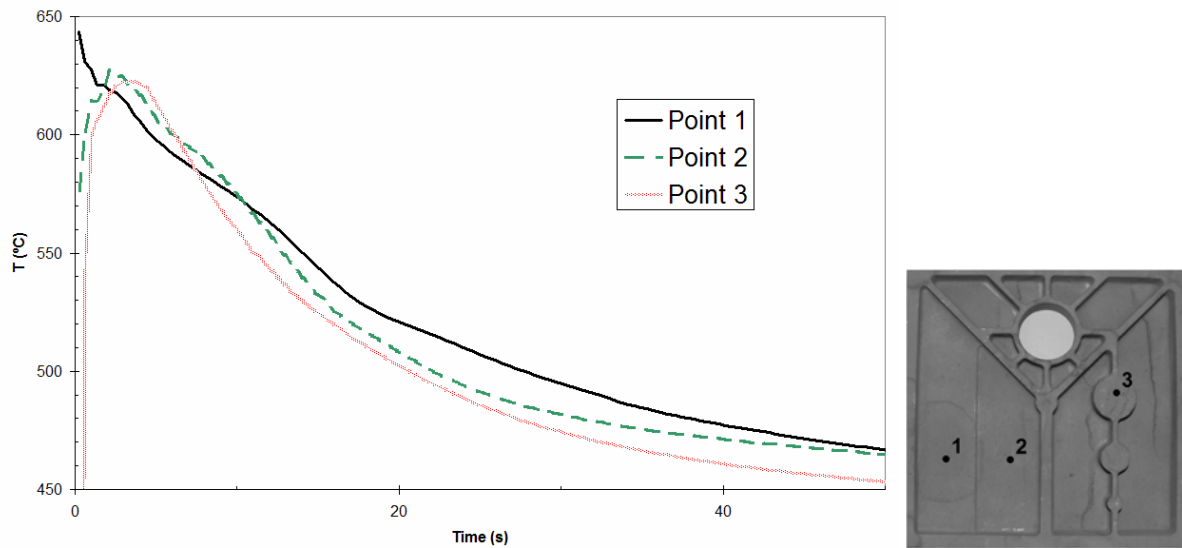


Figure 4.10. Measured cooling curves at the indicated points in the MRI207S sand-cast test part (PSFM).

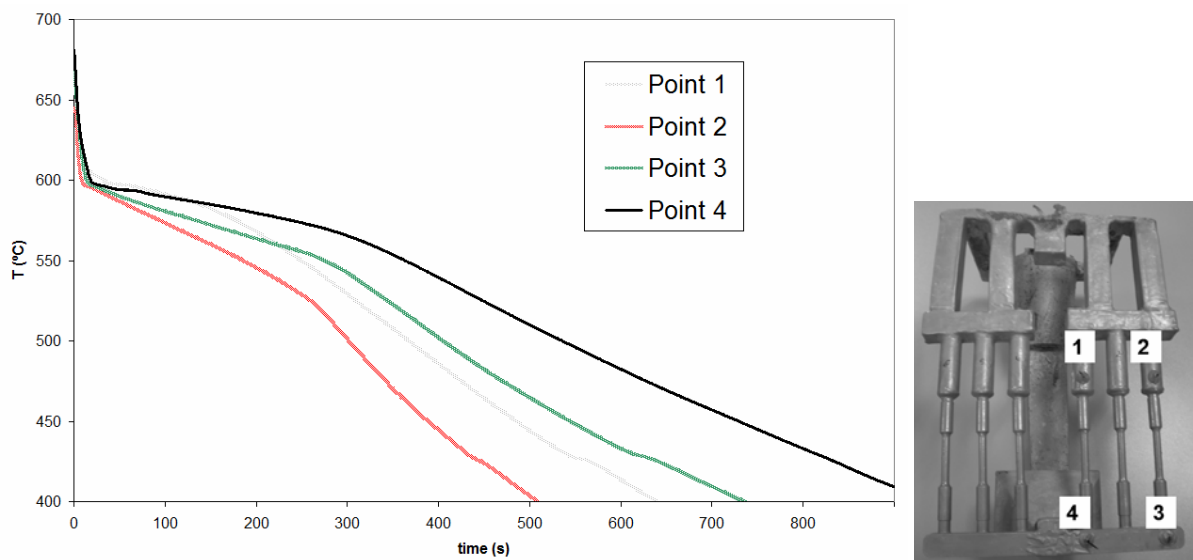


Figure 4.11. Measured cooling curves at the indicated points in the AZ91E investment-cast tensile bars at MGEP (TIMA).

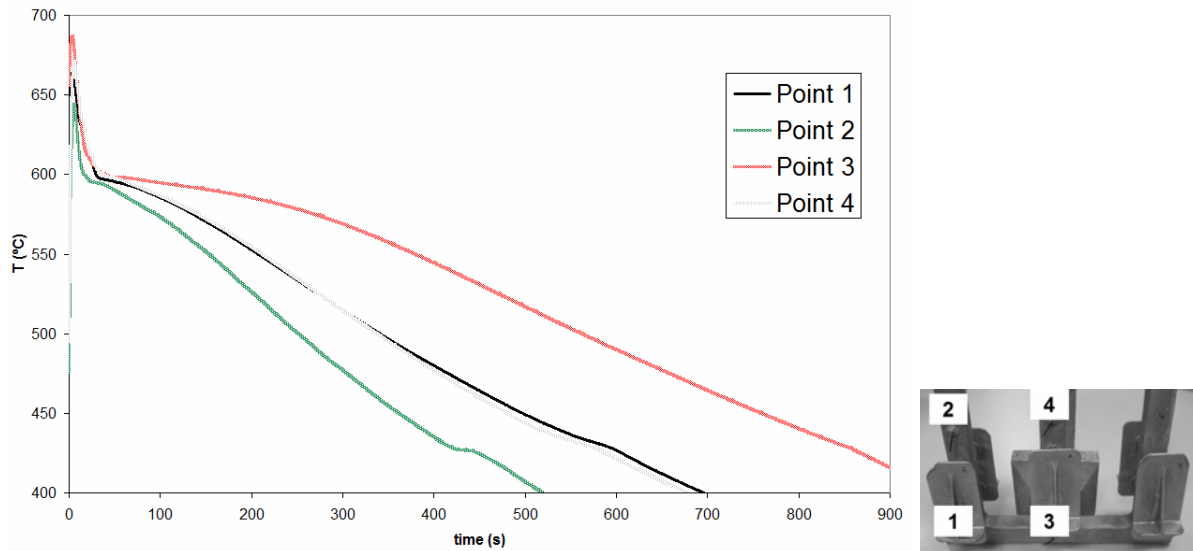


Figure 4.12. Measured cooling curves at the indicated points in the AZ91E investment-cast components at MGEP (CIMA).

The melt arrives at each point in the maximum temperature shown in the graphs. From here on, the cooling starts. At temperatures around 600°C the solidification starts for the AZ91E alloy and at temperatures around 620–640°C for the MRI207S alloy. This temperature can be distinguished by the curves due to a change in the slope of the curve. The solidification is finished with a last change of slope at around 430°C for the AZ91E and 520°C for the MRI207S alloy. The eutectic reaction coincides with the end of solidification. Luo [LUO94] and Busk [BUS87] report undercooling of the eutectic reaction for AZ91. They measured the reaction at 425–427°C instead of at the equilibrium Mg–Al eutectic temperature of 437°C. The AZ91E alloy has an eutectic transformation at this temperature, where the  $\gamma$ -Al<sub>12</sub>Mg<sub>17</sub> phase is generated. Table 4.1, Table 4.2 and Table 4.3 show the characteristic parameters extracted from the cooling curves. These parameters are:

- **Maximum temperature:** this is the maximum temperature registered in each analysed curve.
- **Liquidus temperature:** this temperature corresponds to the temperature of the first change of slope, where the solidification starts. For the points where the melt arrives under the liquidus temperature, the indicated temperature is the maximal temperature at this point.
- **Solidus temperature:** this temperature corresponds to the temperature of the last change of slope, where the solidification is finished.
- **Solidification time:** this is the time spent from the liquidus temperature to the solidus temperature.

A comment should be made about the values presented. The values of the curves measured in the foundries (Table 4.1 and Table 4.2) are average values taken from 4 different curves. The motivation is to provide statistics. This is due to the fact that the microstructural analysis presented in chapter 5 is not taken from the same castings where the curves were measured. Therefore, it was decided to work with average values in the parts produced in the foundries. However, the same parts, where cooling curves were registered, were analysed for microstructural analysis in the castings produced in MGEP.

Consequently, the values are directly related to the points and they are not average but individual measurements (Table 4.3).

*Table 4.1. Solidification temperatures and times of the sand, investment and gravity die-cast AZ91E test-parts produced in the foundries (average values; PSFA, PIFA and PGFA).*

Test-parts in the foundries	Area	T <sub>max</sub> (°C)	T <sub>liquidus</sub> (°C)	T <sub>solidus</sub> (°C)	t <sub>s</sub> (s)
PSFA Sand-casting	Point 1	592.9	579.0	421.0	<b>86.9</b>
	Point 2	591.8	592.0	423.0	<b>77.9</b>
	Point 3	585.9	585.2	423.3	<b>45.0</b>
PIFA Investment-casting	Point 1	654.2	596.0	425.0	<b>45.7</b>
	Point 2	652.7	595.5	423.7	<b>47.5</b>
	Point 3	640.1	595.3	425.5	<b>41.7</b>
PGFA Gravity die-casting	Point 1	583.0	583.0	416.0	<b>45.7</b>
	Point 2	589.0	589.0	415.0	<b>47.5</b>

*Table 4.2. Solidification temperatures and times of the sand, investment and gravity die-cast MRI207S test-parts produced in the foundries (average values; PSFM, PIFM and PGFM).*

Test-parts in the foundries	Area	T <sub>max</sub> (°C)	T <sub>liquidus</sub> (°C)	T <sub>solidus</sub> (°C)	t <sub>s</sub> (s)
PSFM Sand-casting	Point 1	644	619	516	<b>19.8</b>
	Point 2	627	623	516	<b>14.8</b>
	Point 3	623	622	516	<b>12.8</b>
PIFM Investment-casting	Point 1	703.7	641.0	533.7	<b>34.5</b>
	Point 2	705.3	640.0	533.0	<b>36.4</b>
	Point 3	692.0	638.3	533.8	<b>23.4</b>
PGFM Gravity die-casting	Point 1	630.0	630.0	525.5	<b>24.0</b>
	Point 2	631.4	631.4	522.5	<b>24.3</b>

*Table 4.3. Solidification temperatures and times of the sand, investment and gravity die-cast AZ91E tensile bars and components produced in MGEP (TIMA and CIMA).*

Tensile bars and components in MGEP	Area	T <sub>max</sub> (°C)	T <sub>liquidus</sub> (°C)	T <sub>solidus</sub> (°C)	t <sub>s</sub> (s)
TIMA10	Point 1	648	596	417	<b>437.5</b>
	Point 2	629	595	423	<b>375.5</b>
	Point 3	651	595	424	<b>316.5</b>
	Point 4 <sup>a</sup>	633	580	422	<b>524.5</b>
TIMA11	Point 1	643	594	423	<b>364</b>
	Point 2	612	599	423	<b>345</b>
	Point 3 <sup>b</sup>	461	461	428	<b>40.6</b>
	Point 4	675	612	424	<b>562</b>
CIMA01	Point 1	664	599	428	<b>555</b>
	Point 2	644	595	425	<b>421.5</b>
	Point 3	687	599	427	<b>812</b>
	Point 4	671	598	426	<b>537</b>

<sup>a</sup> Point E in the TIMA10 has a high undercooling. Solidification starts at 580°C. This point will not be taken into account because of this different behaviour.

<sup>b</sup> Point 3 measured in TIMA11 is not valid due to a bad placement of the thermocouple inside the mould. Therefore, the thermocouple was not in contact with the melt and the results are not valid.

In the following chapters, the values of solidification times are compared with the generated microstructures and mechanical properties for a further understanding of the behaviour of magnesium alloys when different solidification rates are applied. Correlations between solidification time and microstructure are given in chapter 7.

### 4.3 Casting of HPDC tensile bars

HPDC tensile bars were cast by MRI in the Dead Sea, Israel. The reference alloys were the commercial AZ91D and AM50A alloys. The reference alloys were compared to the newly developed AM50+Si+Sn alloy. The developed alloy was based in the AM50 reference alloy and was modified with Si and Sn. The tensile parts received were free of oxides and impurities. The porosity was also finely dispersed as usual in high-pressure die-castings.

HPDC test parts were produced in Fémalk co. Contrary to tensile specimens, test-parts were not satisfactory because of high porosity levels. The reason is that the geometry of the part is not suitable for HPDC due to the thick areas. The porosity of the test parts caused problems during machining operations at MGEP. Some of the tensile samples broke down when machining because of the lack of soundness. Furthermore, the samples which were not broken during the machining presented very poor tensile properties. More details about the amount of porosity encountered in HPDC test parts are given in the following chapters.

#### 4.4 Summary and outlook

In this chapter the casting trials and the acquisition of cooling curves are explained.

Casting parameters were optimised to obtain acceptable castings. Parameters like filling time, melt temperature, shell material in investment-casting, inhibitors and the use of grain refiners are discussed in this chapter. Short filling times, less than 10 s, lead to complete filling, while misruns were present with higher filling times. Surface oxidation was solved with the application of the liquid inhibitor  $\text{NaBF}_4$  to the investment-cast shells. Moreover, the effect of the grain refiner was verified in the AZ91E alloy. The grain refiner, apart of the reduction of the grain size, leads to the change in the morphology of the  $\gamma$ - $\text{Al}_{12}\text{Mg}_{17}$  phase.

The cooling curves obtained at different points are also given and the essential information disclosed. This information is used for the prediction of microstructures. The main discussion about these results is done in the chapter 7, where all the results are put together and the main conclusions presented. In the measurements of solidification curves, it is observed that the solidification time is more dependent upon the casting parameters than on technology. In theory, sand-casting is the technology which has the slowest solidification due to a lower thermal conductivity of the moulds. Nevertheless, for example in the MRI207S test part, the solidification time is higher in a same area in investment-casting. This means that it is also dependent upon the melt and mould temperatures, mould material, usage of freezers, feeders, etc. It should be noted that the usage of freezers and feeders was remarkable in the design of the sand-cast test-part in order to obtain sound castings.



## **CHAPTER 5 - MICROSTRUCTURAL EVOLUTION**



## 5 MICROSTRUCTURAL EVOLUTION

The objective of this chapter is to analyse the grain size and precipitates of the cast parts in order to be able to relate the microstructures to the cooling conditions explained previously and to the mechanical properties which are described in chapter 6.

With this aim, gravity and high-pressure die-casting microstructures and fracture surfaces were analysed at different points. Precipitates were identified in order to achieve a better understanding of the effect of the alloying elements. In addition, grain sizes of gravity cast alloys were measured. Porosity level also influences the mechanical properties. Therefore, the porosity in the test part was also measured.

Finally, for a better understanding of the formability of magnesium alloys, the texture creation of HPDC tensile bars during deformation was analysed.

### 5.1 Identification of microstructures

First of all, the characterization of microstructures using SEM and optical microscopy was studied. The kind of precipitates present was identified for each alloy. In general, the precipitation was similar for all the alloys at the different cooling rates. The difference was mainly in the morphology of the microstructure between high-pressure die-castings and gravity castings. Gravity and high-pressure die casting precipitates are separately analysed for a better understanding. The phases present in Mg-Al commercial alloys are described in literature, for example in [AGH04, EML66, KAI03]. The phases of the new alloys were described inside the IDEA project by Technion, Israel Institute of Technology. Once the phases are identified, the description of the microstructure is done by optical and electronic microscopy.

#### 5.1.1 Gravity cast microstructures

Two alloys were cast in gravity casting technologies, which are the AZ91E and the MRI207S alloys. The phases present in those alloys are summarized in Table 5.1.

*Table 5.1. Phases present in AZ91E and MRI207S alloys in as-cast and T6 conditions.*

Alloy	Phases
<b>AZ91E</b>	$\alpha$ -Mg $\gamma$ -(Al,Zn) <sub>12</sub> Mg <sub>17</sub> Al <sub>x</sub> Mn <sub>y</sub>
<b>MRI207S</b>	$\alpha$ -Mg (Gd,Nd)Mg <sub>3</sub>

Figure 5.1 shows the optical micrographs of the alloy AZ91E in as-cast and T6 conditions. This alloy shows a dendritic morphology in as-cast condition. After T6 treatment, the continuous precipitated  $\gamma$ - $\text{Al}_{12}\text{Mg}_{17}$  forms a lamellar structure with  $\alpha$ -Mg in its totality (the dark area in Figure 5.1 b).

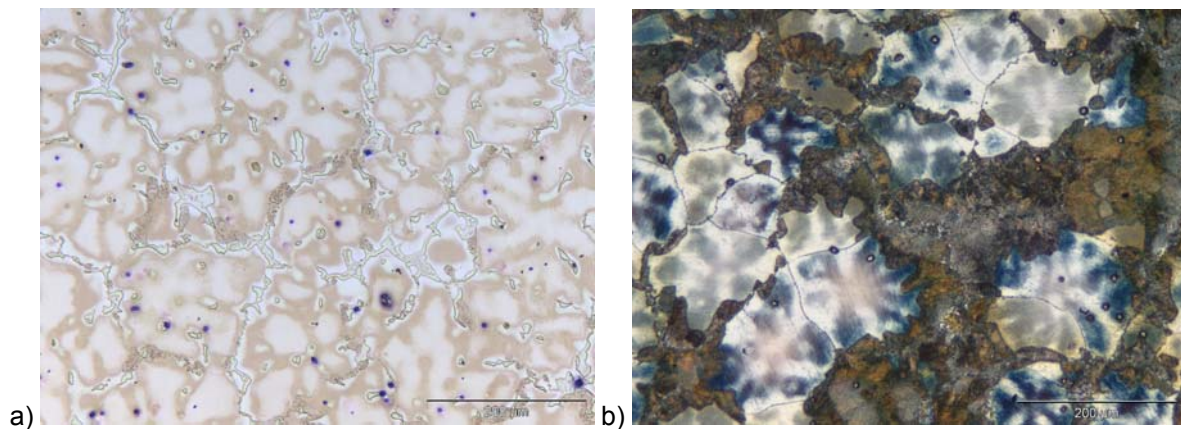


Figure 5.1. Optical microscopy of investment-cast a) AZ91E-F; and b) AZ91E-T6 (TSFA).

A trial to characterise the precipitates was made in this task. The main encountered problem is concerning the quantification of second phases. The etchants utilised do not produce a constant contrast of the second phases in the microstructure. When utilising automatic image analysis software for the counting of the amount of several phases, the error is big. An error superior to 20% is estimated in the case of the counting of the pearlitic structure in AZ91E. This counting depends mostly on the etching. The etching is dependent upon the alloy, the days the etchant is made, the etching time and the exact etchant composition, amongst others. As the composition inside the grains is also different, a contrast is also found here, mixing the matrix with the eutectic in the image analysis.

Figure 5.2 shows the SEM images of the AZ91E alloy in as-cast condition (F) and after solution and precipitation heat treatment (T6). In the as-cast condition the microstructure of AZ91E is based on an  $\alpha$ -Mg matrix with intermetallic precipitates of  $\text{Al}_x\text{Mn}_y$  inside the grains. There is an eutectic precipitation of  $\gamma$ - $\text{Al}_{12}\text{Mg}_{17}$  in the grain boundaries.  $\gamma$ - $\text{Al}_{12}\text{Mg}_{17}$  is mostly found in continuous precipitation, which is sometimes divorced. Small quantities of  $\gamma$ - $\text{Al}_{12}\text{Mg}_{17}$  phase also forms a lamellar structure with  $\alpha$ -Mg. After T6 heat-treatment, the continuous or divorced eutectic disappears completely. The  $\gamma$ - $\text{Al}_{12}\text{Mg}_{17}$  phase appears uniquely forming a lamellar eutectic structure. A detail of this lamellar structure is shown in Figure 5.3. However, the lamellar spacing is not constant in the whole microstructure.

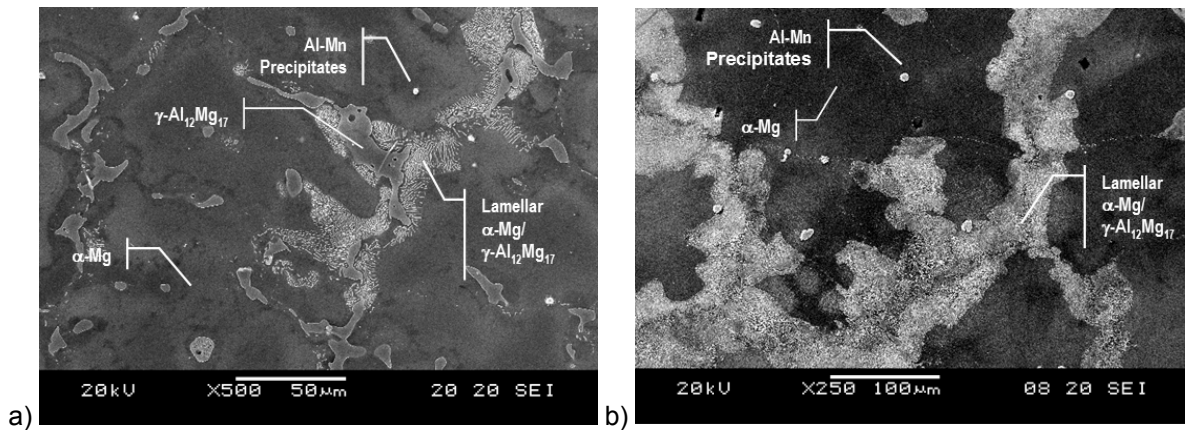


Figure 5.2. SEM micrographs showing microstructure of a) sand-cast AZ91E-F; and b) sand-cast AZ91E-T6 (TSFA).

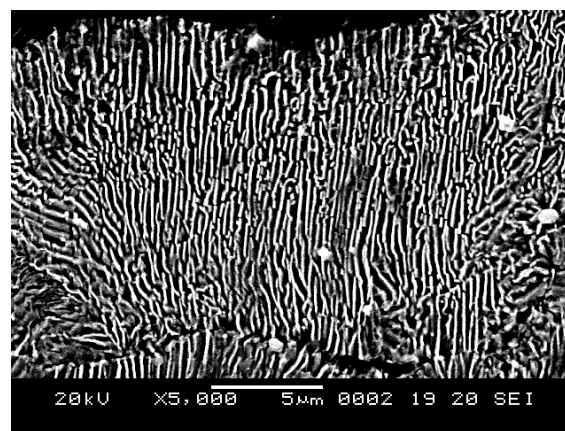


Figure 5.3. Lamellar eutectic detail of sand-cast AZ91E-T6 alloy (TSFA).

The reduced ductility of the AZ91E commercial alloy, even after T6 treatment, can be explained by the coarse grain size and the large amount of pearlitic phase in grain boundaries in the T6 condition. The even higher brittleness in as-cast condition is due to the large continuous precipitates of  $\gamma$ -Al<sub>12</sub>Mg<sub>17</sub> in the grain boundaries. It is in accordance with the literature review, where Fox [FOX45] shows the fracture of the AZ91 alloy from the grain boundary. The  $\gamma$ -Al<sub>12</sub>Mg<sub>17</sub> phase appears in large amounts in the AZ91 alloy increasing the brittleness.

The MRI207S alloy is based on the Mg-Zn-Zr-Nd-Y (Gd) alloying system. It is, in fact, also a creep resistant alloy. Avraham *et al.* [AVR07] describe the precipitates of this alloy in the frame of the IDEA project. Precipitation hardening and grain boundary strengthening are major mechanisms contributing to the strength of this alloy. The microstructure in as-cast condition (Figure 5.4a) consist of an  $\alpha$ -Mg matrix, where the content in the interior of the grains is of  $\alpha$ -Mg with some Zr and Gd. Next to the grain boundaries Y and Nd are also found. Precipitation of an eutectic (Gd,Nd)Mg<sub>3</sub> intermetallic appears in the grain boundary. After heat treatment (Figure 5.4b), the grains are mainly composed of  $\alpha$ -Mg with some Zr and Gd content. Fine (Gd,Nd)Mg<sub>3</sub> also precipitates in the matrix. The grain boundary area is surrounded with a continuous fine and coarse precipitation of (Gd,Nd)Mg<sub>3</sub>.

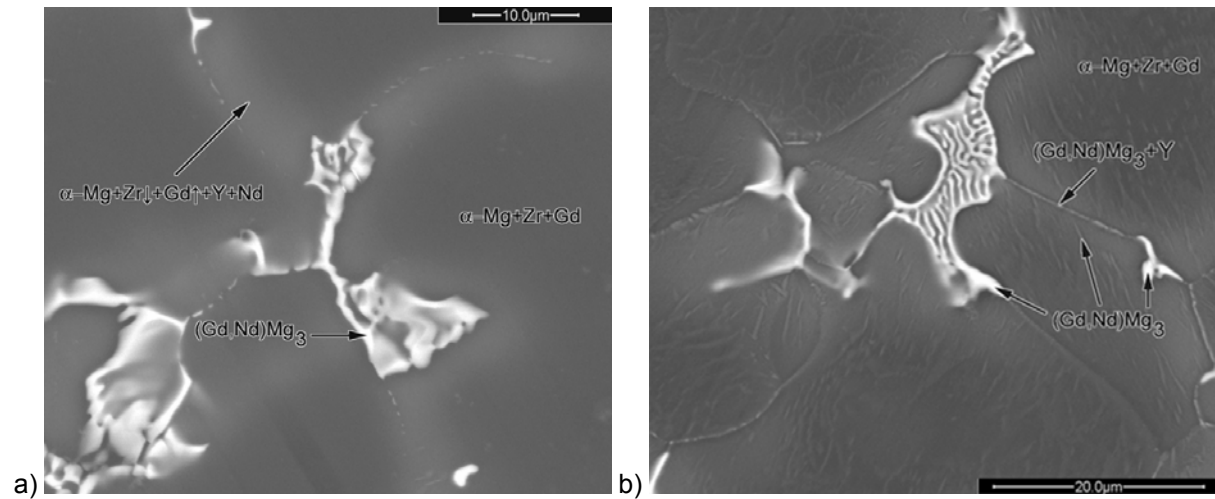


Figure 5.4. a) BSE micrograph of alloy MRI207S-F; b) BSE micrograph of MRI207S-F after thermal exposure at 200°C for 32 days [AVR07].

Figure 5.5 shows the optical micrographs of MRI207S in as-cast and T6 conditions. Grain growth is observed after T6 heat treatment in the MRI207S alloy. A globular morphology of the grains prevails in both conditions, being the grains hexagonal shaped.

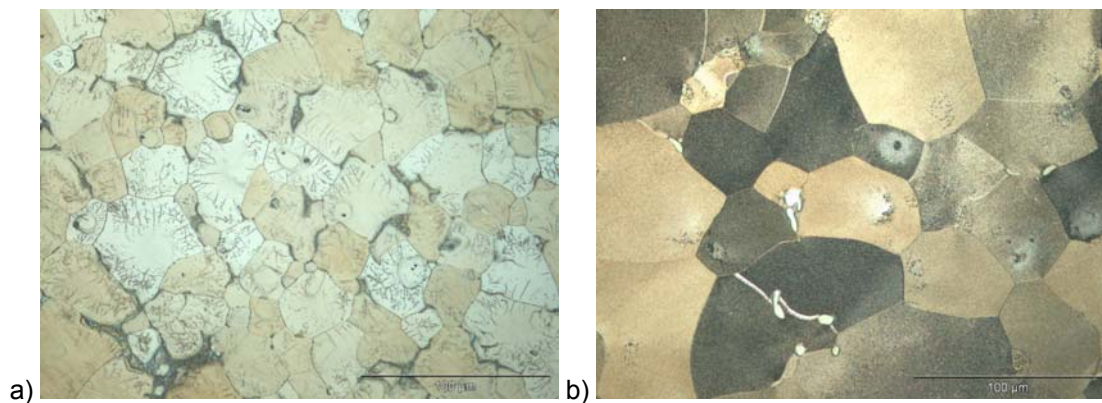


Figure 5.5. Optical micrographs of a) MRI207S-F; and b) MRI207S-T6 (TSFM).

After T6 heat treatment, precipitation hardening increases the strength of this alloy in detriment to the ductility. Gross precipitates are mostly dissolved in the matrix as can be seen in Figure 5.5. Instead, small precipitation happens inside the grain.

### 5.1.2 High-pressure die-cast microstructures

Table 5.2 summarises the phases present in the AZ91D, AM50 and AM50+Si+Sn high-pressure die-cast alloys.

Table 5.2. Phases present in the AZ91D, AM50 and AM50+Si+Sn HPDC alloys.

Alloy	Phases
AZ91D	$\alpha$ -Mg $\gamma$ -Al <sub>12</sub> Mg <sub>17</sub> ( $\eta$ -Al <sub>8</sub> Mn <sub>5</sub> )
AM50	$\alpha$ -Mg $\gamma$ -Al <sub>12</sub> Mg <sub>17</sub> ( $\eta$ -Al <sub>8</sub> Mn <sub>5</sub> )
AM50+Si+Sn	$\alpha$ -Mg $\gamma$ -Al <sub>12</sub> Mg <sub>17</sub> ( $\eta$ -Al <sub>8</sub> Mn <sub>5</sub> )  MgSi <sub>2</sub>

The precipitation of  $\gamma$ -Al<sub>12</sub>Mg<sub>17</sub> mainly takes place in the grain boundaries. Furthermore,  $\eta$ -Al<sub>8</sub>Mn<sub>5</sub> is found inside the grains in small precipitates of about 200-500 nm. AZ91D presents a quite similar microstructure to AM50, with the difference being a larger quantity of precipitation of  $\gamma$ -Al<sub>12</sub>Mg<sub>17</sub> at the grain boundaries due to its higher amount of Al. These precipitates are the responsible of higher strength and the reduced ductility of the AZ91D alloy in comparison to the AM50 alloy. The AM50 and AM50+Si+Sn alloys on the other hand differs in the precipitates which are present in the microstructure. In order to show this difference, the microstructures of AM50 and AM50+Si+Sn are shown in Figure 5.6. In this figure the change in the morphology and distribution can be seen. In the grain boundary area of the AM50+Si+Sn alloy, precipitates formed by Al-Mn and MgSi<sub>2</sub> are also found (Figure 5.7) which are not present in the AM50 alloy.

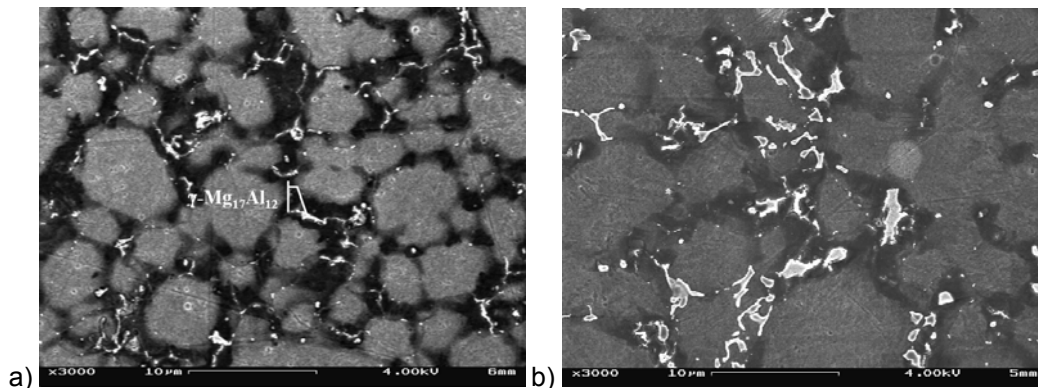


Figure 5.6. Microstructures of a) AM50; b) AM50+Si+Sn.

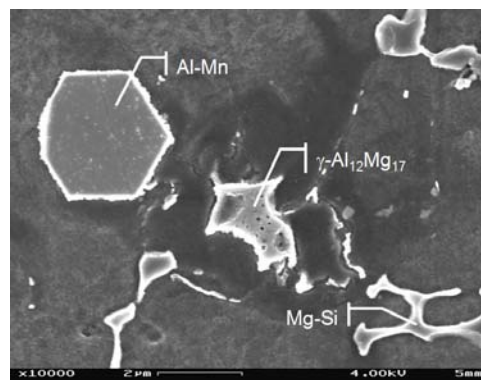


Figure 5.7. Intermetallics in grain boundaries of the alloy AM50+Si+Sn.



The precipitates present in the AM50+Si+Sn alloy increase the strength of the alloy compared to the AM50 alloy and being similar to the strength of the AZ91D alloy. However, the reduction in ductility of this alloy is not significantly reduced and is kept close to that of AM50.

## 5.2 Analysis of fracture zones

When observing fracture surfaces in the Scanning Electron Microscope (SEM) the fracture modes can be defined for each alloy and each heat treatment condition. First, gravity cast alloys are explained in as-cast and heat treat conditions and then, HPDC fracture modes are discussed.

All the gravity cast alloys analysed show cleavage fracture. Cleavage fracture mode is a transgranular fracture, propagating the crack from the grain boundary (Figure 5.8). Cleavage is a low-energy fracture that propagates along well-defined low-index crystallographic planes known as cleavage planes [ASM87]. AZ91E in as-cast condition shows a brittle fracture. The cleavage planes are small, but the fracture surface shows no deformation. All of them are flat planes without any deformation. AZ91E-T6 shows big cleavage planes in the surface. It is a brittle shaped fracture because the crack is propagated from the pearlitic structure of  $\gamma\text{-Al}_{12}\text{Mg}_{17}$  and  $\alpha\text{-Mg}$  which is located in the grain boundaries. MRI207 alloy shows a similar fracture mode in as-cast and heat treat conditions. They show a mixed fracture mode. There are some cleavage planes together with a dimple fracture. The whole fracture surface shows higher deformation than the AZ91E alloy and some dimples appear between the cleavage surfaces.

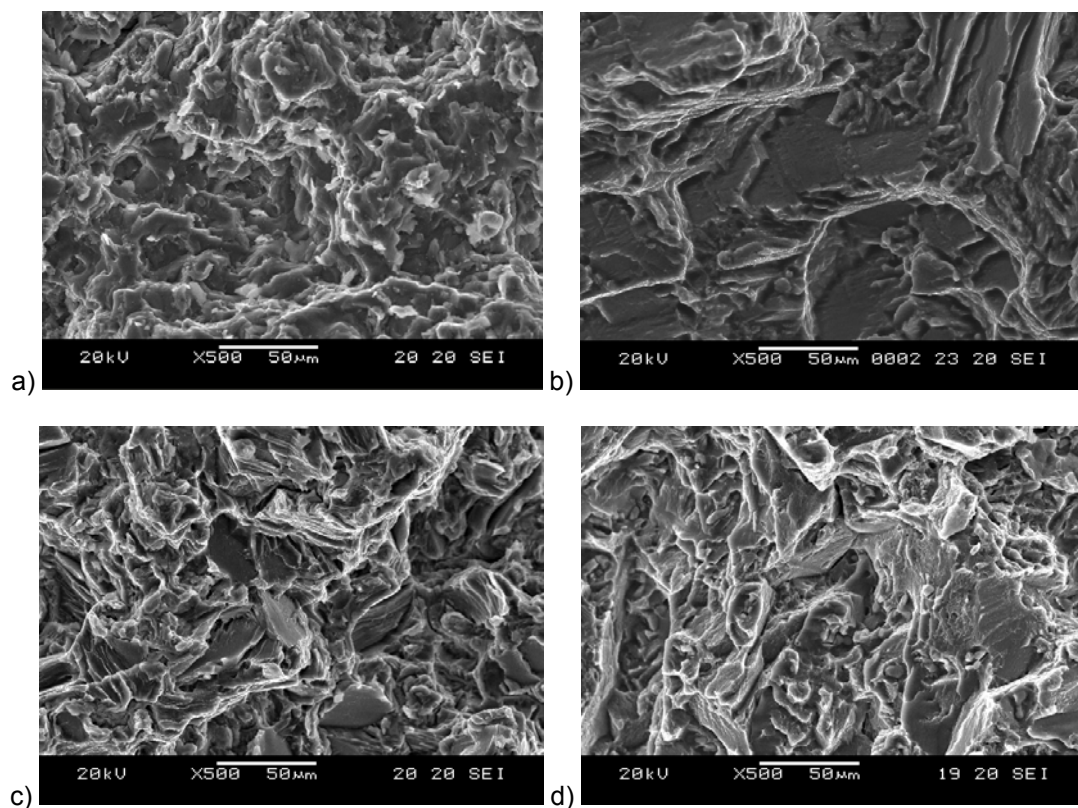


Figure 5.8. Fracture surfaces of a) AZ91E-F; b) AZ91E-T6; c) MRI207S-F and d) MRI207S-T6 (TSFA and TSFM).



With regard to the fracture mechanism of HPDC alloys, all samples show an intergranular dimple fracture (see Figure 5.9) caused by decohesion inside the matrix. However, even if it is a ductile fracture, these samples do not show any necking behaviour in the fracture zone. There is ample evidence of porosity, caused both by entrapped gas and by shrinkage (see Figure 5.10). The microshrinkage in these alloys is characterized by zones without any deformation and appears as rounded branches.

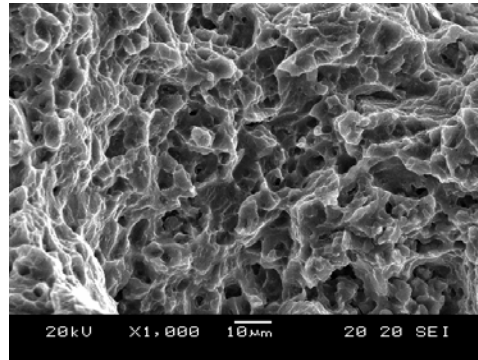


Figure 5.9. Dimple fracture zone in alloy AM50+Si+Sn.

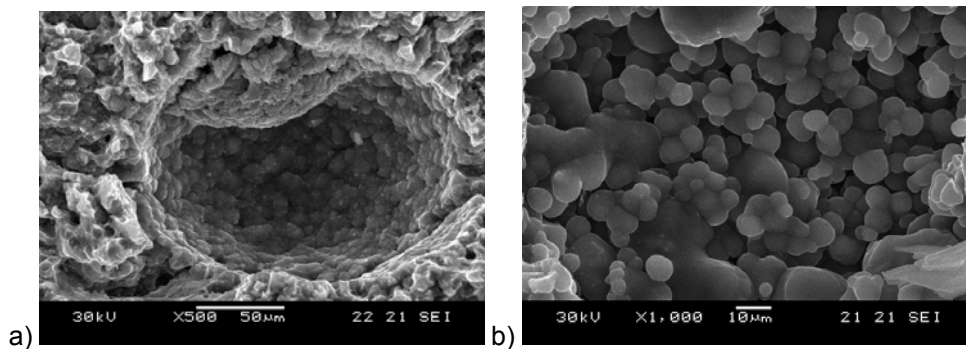


Figure 5.10. Presence of porosity in the fracture surface of high-pressure die-cast alloys: a) gas porosity; b) microshrinkage (AM50 alloy).

SEM images were taken of polished and etched samples near the fracture and perpendicular to it. In the AM50+Si+Sn alloy,  $MgSi_2$  precipitates were cracked and decohesion occurred with the matrix (Figure 5.11) which could be a prior step before producing the dimpled fracture. Even though in the whole deformed area cracked precipitates were found, the percentage next to fracture was higher.

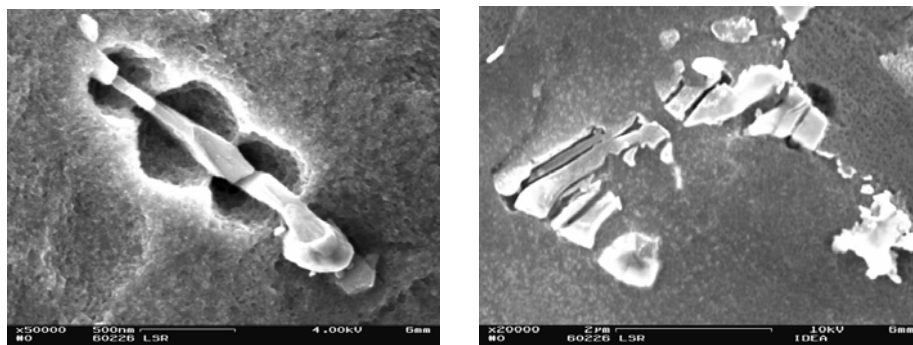
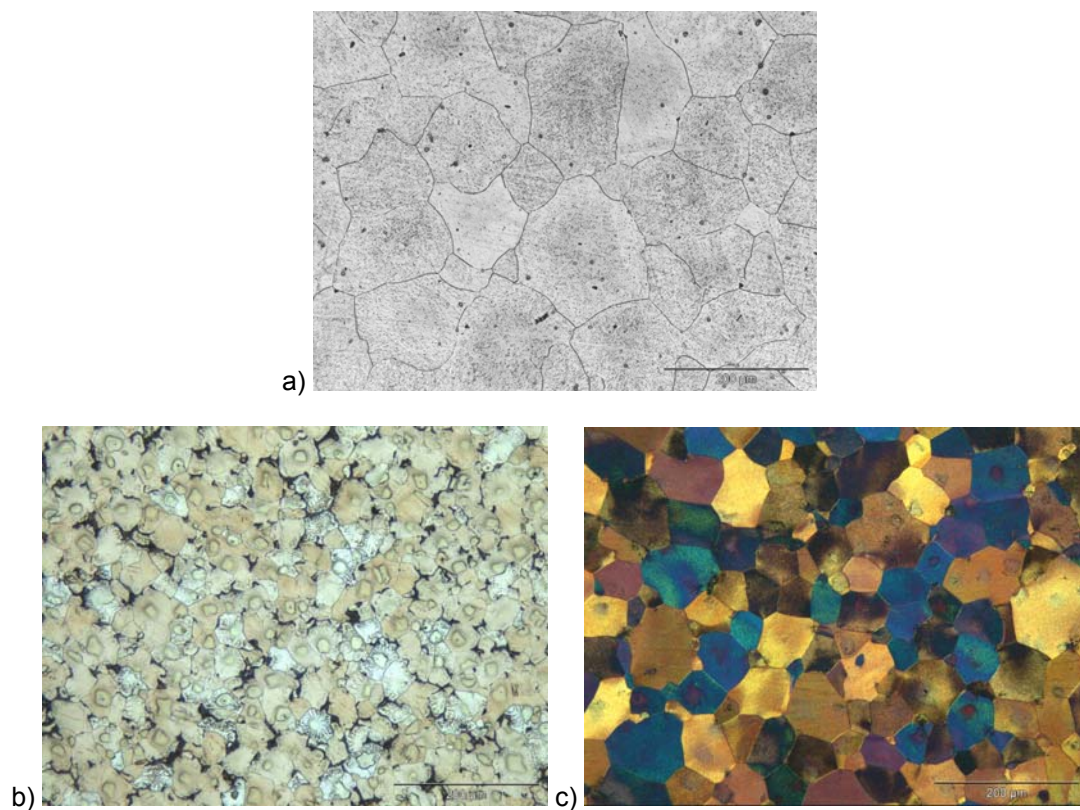


Figure 5.11.  $MgSi_2$  intermetallics after deformation next to the fracture area.

### 5.3 Analysis of grain size distribution in gravity cast alloys

Grain sizes were measured for establishing relationships between solidification and microstructures and between microstructures and mechanical properties. Grain size measurements were performed in gravity-cast tensile bars, test parts and components.

Grain sizes were measured with the linear intercept method. The prepared microstructures are shown in Figure 5.12. AZ91E-F and AZ91E-T6 alloys were measured after solubilisation. The reason was to clearly distinguish the grain structure. Otherwise, the problem for grain size measurement in as-cast conditions is the dendritic morphology, which makes it difficult to distinguish the grains. However, after complete T6 heat treatment, large areas of eutectic appear in the microstructure, and grain structure is, again, difficult to recognize. MRI207S-F and MRI207S-T6 did not have any further heat treatment because grain structure was clearly defined.



*Figure 5.12. Microstructures of the alloys for grain size measurement; a) solubilised AZ91E (TSFA); similar microstructure for as-cast and heat-treat conditions after solubilisation); b) MRI207S-F (TSFM); c) MRI207-T6 (TSFM).*

Results from the grain size measurements of sand, investment and gravity die-cast tensile bars are shown in Table 5.3.

Table 5.3. Grain size distribution for AZ91E and MRI207S alloys in as-cast and T6 condition in tensile bars.

Alloy	Technology	Nomenclature	Heat treatment	Grain size ( $\mu\text{m}$ )	ASTM
AZ91E	Sand-casting	TSFA	F	121	2.8
			T6	109	3.1
MRI207S		TSFM	F	29	6.9
			T6	49	5.4
AZ91E	Investment-casting	TIFA	F	187	
			T6	234	
MRI207S		TIFM	F	33	
			T6	59	
AZ91E	Gravity die-casting	TGFA	F	223	
			T6	180	
MRI207S		TGFM	F	26	
			T6	51	

It was not possible to measure the grain sizes in all the control points illustrated in Figure 5.13 on the test parts. In some test parts, part of the casting was used for other measurements and some of the points were not available. The most interesting values are the obtained in positions 1, 2 and 3, where solidification curves and tensile properties were also measured. However, in order to have a complete distribution of the grain size in the casting, more points were defined. Even if some parts were lost, a considerable amount of data was obtained. Some of the results are plotted in Figure 5.14 and a summary of all the measured values is shown in Table 5.4.

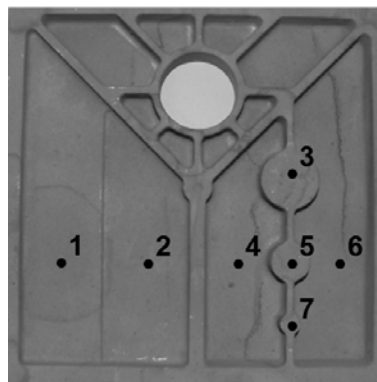


Figure 5.13. Positions for grain size measurement in the test part.

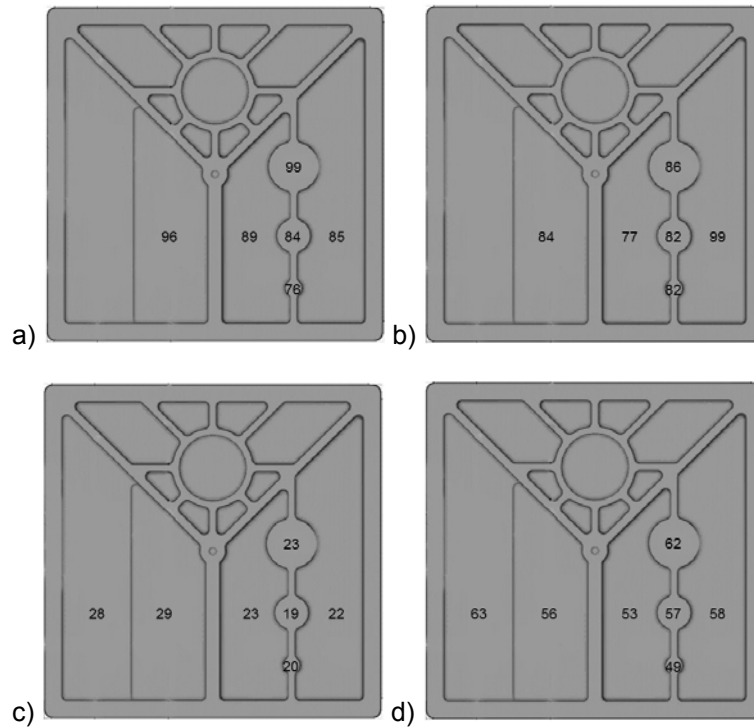


Figure 5.14. Grain size ( $\mu\text{m}$ ) distribution in the: a) sand-cast AZ91E-F alloy (PSFA); b) sand-cast AZ91E-T6 (PSFA); c) sand-cast MRI207-F (PSFM); d) investment-cast MRI207-T6 (PIFM).

Table 5.4. Grain size distribution for the AZ91E and MRI207S alloys in as-cast and T6 condition in the control points defined in Figure 5.14.

Alloy	Technology	Nomenclature	Heat-treatment	Units	Position						
					1	2	3	4	5	6	7
AZ91E	Sand-casting	PSFA	F	$\mu\text{m}$		96	99	89	84	85	76
				ASTM		3.5	3.4	3.7	3.9	3.8	4.1
			T6	$\mu\text{m}$		84	86	77	82	99	82
				ASTM		3.9	3.8	4.0	3.9	3.4	3.9
	Investment-casting	PIFA	T6	$\mu\text{m}$	154						
				ASTM	2.1						
Gravity die-casting	PGFA	T6	$\mu\text{m}$	89							
			ASTM	3.7							
MRI207S	Sand-casting	PSFM	F	$\mu\text{m}$	28	29	23	23	19	22	20
				ASTM	7.0	6.9	7.5	7.5	8.1	7.7	8.0
			T6	$\mu\text{m}$	Abnormal grain growth						
				ASTM	Abnormal grain growth						
	Investment-casting	PIFM	F	$\mu\text{m}$	44	45					
				ASTM	5.7	5.6					
			T6	$\mu\text{m}$	63	56	62	53	57	58	49
				ASTM	4.7	5.1	4.7	5.2	4.9	4.9	5.4
	Gravity die-casting	PGFM	T6	$\mu\text{m}$			58	63	66	53	
				ASTM			5.0	4.7	4.6	5.2	

The sand-cast MRI207S test parts suffered abnormal grain growth during heat treatment, and an average grain size was not logical in this case. The grain size varied from around one millimetre to a few tenths of microns. These values were discarded due to the lack of homogeneity. An example of the inhomogeneous grain size is given in Figure 5.15.

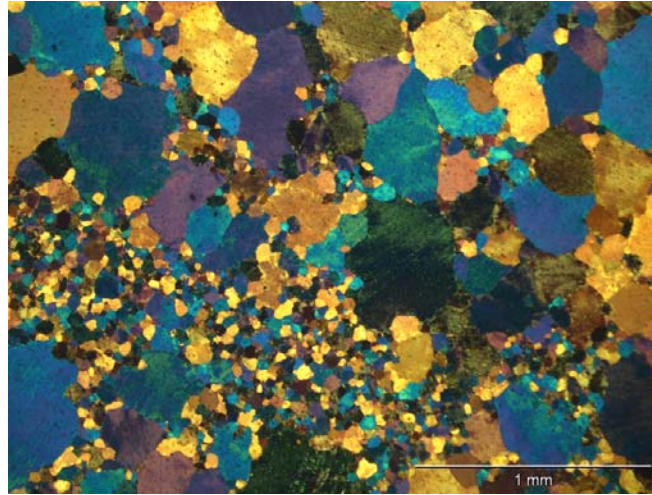


Figure 5.15. Inhomogeneous grain size distribution in the MRI207S sand-cast test part after T6 heat treatment.

In order to have a greater amount of microstructures relating to cooling curves, some AZ91E investment castings were produced in MGEP. In these castings thermocouples were placed in the bottom and upper sides of the parts as has already been described in chapter 3.

Table 5.5. Grain size for the AZ91E alloy in as-cast condition in the control points for the investment-cast parts produced in MGEP (TIMA and CIMA).

TIMA and CIMA	Placement	Grain size	
		$\mu\text{m}$	ASTM
TIMA10	Point 1	132	2.6
	Point 2	137	2.5
	Point 3	120	2.9
	Point 4	120	2.8
TIMA11	Point 1	149	2.2
	Point 2	135	2.5
	Point 3	140	2.4
	Point 4	142	2.3
CIMA01	Point 1	205	1.3
	Point 2	171	1.8
	Point 3	*	*
	Point 4	193	1.5

\* high porosity level

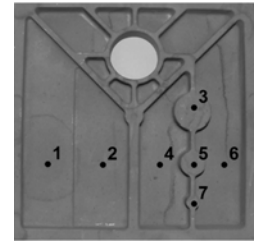
A high porosity level was encountered in the D area (CIMA01) related to the other zones. Due to this dispersion, it was decided not to use these values for the correlation between grain size and cooling curves. The shrinkage porosity in this area was up to 40%, compared to less than 5% in all the other areas.

#### 5.4 Analysis of porosity distribution

Porosity distribution was measured in the test parts because of the influence it could have on mechanical properties. The following values (Table 5.6) were obtained using the image analysis method for HPDC, sand, investment and gravity die-casting technologies. Tensile bars had very small porosity levels (0.01% or less) and, therefore, the possible influence was neglected.

Table 5.6. Porosity distribution in the test parts.

Technology	Alloy	Position			
		1	2	3	4 and 6
Sand-casting	AZ91E	0.1	0.1	<0.1	0.1
	MRI207S	0.3	<0.1	<0.1	<0.1
Investment-casting	AZ91E	1.9	3.9	0.5	0.2
	MRI207S	0.3	0.7	0.3	0.2
Gravity die-casting	AZ91E	0.4	3.0	3.8	0.1
	MRI207S	0.2	0.3	0.2	0.1
HPDC	AM50A	9.9	6.6	11.7	0.7



High values of porosity were obtained in high-pressure die-cast test parts. The reason is that it is not a suitable geometry for HPDC due to the thick areas. Low porosity was achieved in sand-cast test parts instead due to a good design of gating and chilling systems. The low porosity obtained in the MRI207S investment and gravity die-cast test parts compared to AZ91E is promising because AZ91 is an alloy with high castability. Therefore, these gravity cast technologies were finely developed in the foundries to obtain the high performance MRI207S alloy.

#### 5.5 Microstructure and texture evolution in HPDC alloys during tensile testing

For a better understanding of the deformation mechanisms and texture generated during deformation of cast samples, the texture of HPDC alloys was analysed in a neutron guide. High-pressure die-cast alloys should not have any texture after the casting operation and texture is developed when forming. AM50 and AM50+Si+Sn alloys were the selected alloys for this study.

When comparing the texture developed after testing in AM50 and AM50+Si+Sn, all the general tendencies are comparable. Thus, it is concluded that the alloying elements do not have any influence in the generation of the texture in these two alloys. The measurements in both of them show a good coherence which will support the comparative analysis between the different alloys for a deformation state. As an example of the results, Figure 5.16 shows the evolution of the peak  $\{10\bar{1}0\}$  before and after deformation for the two alloys. It can be seen that in as-cast condition none of them has a preferential orientation of the grains.

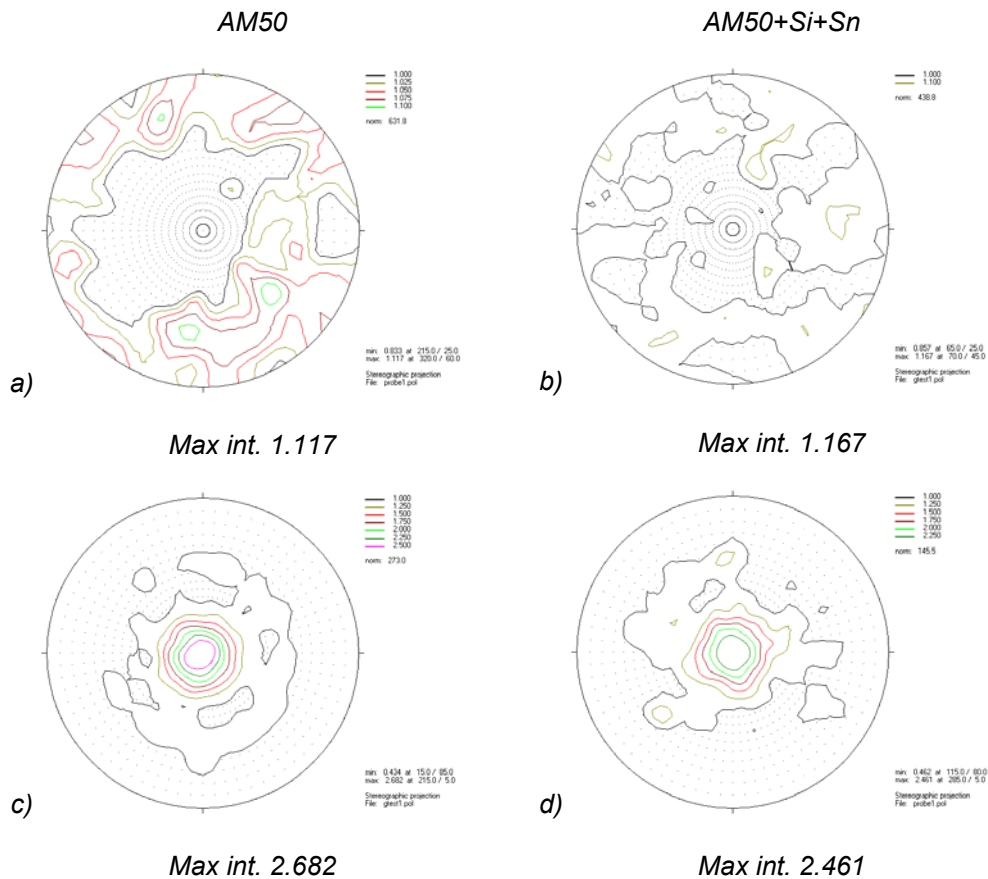


Figure 5.16. Pole figures for the diffraction peak  $(10\bar{1}0)$ ; a) AM50 before testing; b) AM50+Si+Sn before testing; c) AM50 after tensile testing; d) AM50+Si+Sn after tensile testing. The loading direction is perpendicular to the pole figures.

From the figures above, it can be seen that the created texture for both alloys is equivalent in all conditions. The non-deformed samples show a near random distribution of grains (m.r.d. max. 1.1) which can be expected from the solidification conditions. The m.r.d. values of both alloys show a similar texture distribution after fracture. The m.r.d. values are relatively low (about 2.5) and practically independent of the alloy type. It can be concluded that the alloying elements do not generate a change in the texture generation. Therefore, the increment of mechanical properties of the new alloy is not due to a change in the generation of the texture.

For a better understanding of the texture evolution at different strain levels, a single alloy, the AM50A, was chosen for a more detailed analysis. Figure 5.17 shows the tensile engineering curve of the AM50A alloy. The generation of texture during testing was analysed at different deformation levels. Tensile testing was stopped at 4 different strain levels (1%, 5%, 10% and 15%), and the deformations of 20% and 26% were obtained at fracture of two different samples. The most deformed part of the tested samples is considered to be about one centimetre in length including the fracture zone when samples reached fracture. This part was used for the texture measurements in the Stress-Spec instrument.



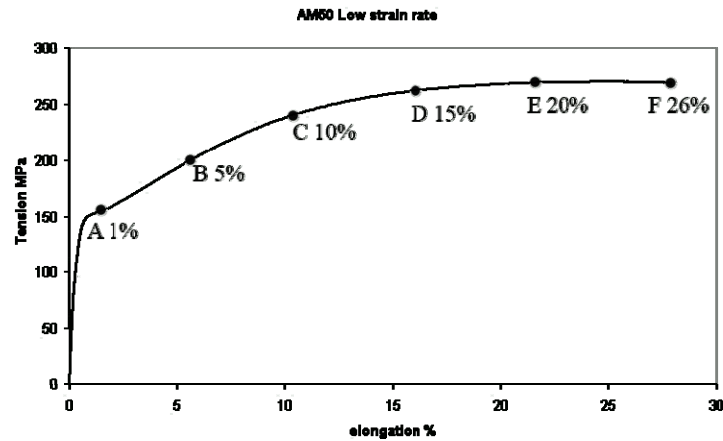


Figure 5.17. Engineering tensile curve of the alloy AM50A, showing the points of deformation where texture was measured.

Figure 5.18 shows the  $(10\bar{1}0)$  pole figures obtained in the AM50A samples at the strain levels defined above. The creation of the texture in tensile test can be observed in this figure. The as-cast sample prior to testing is a non-textured sample, presenting a near random distribution of grains (m.r.d. max. 1.1). A texture generates in the tensile testing, getting more intensity in the  $(0, 0)$  degrees in the  $(10\bar{1}0)$  pole figures. Nevertheless, a change in the main orientation is observed in the 26% elongated sample where the intensity in  $(0, 0)$  becomes smaller and the intensity in the hexagonal faces gets higher (at  $60^\circ$ ). This is also the same tendency described for wrought alloy during tensile testing, even if wrought alloys have higher intensities. In all the pole figures the loading direction (LD) is perpendicular to the pole figure.



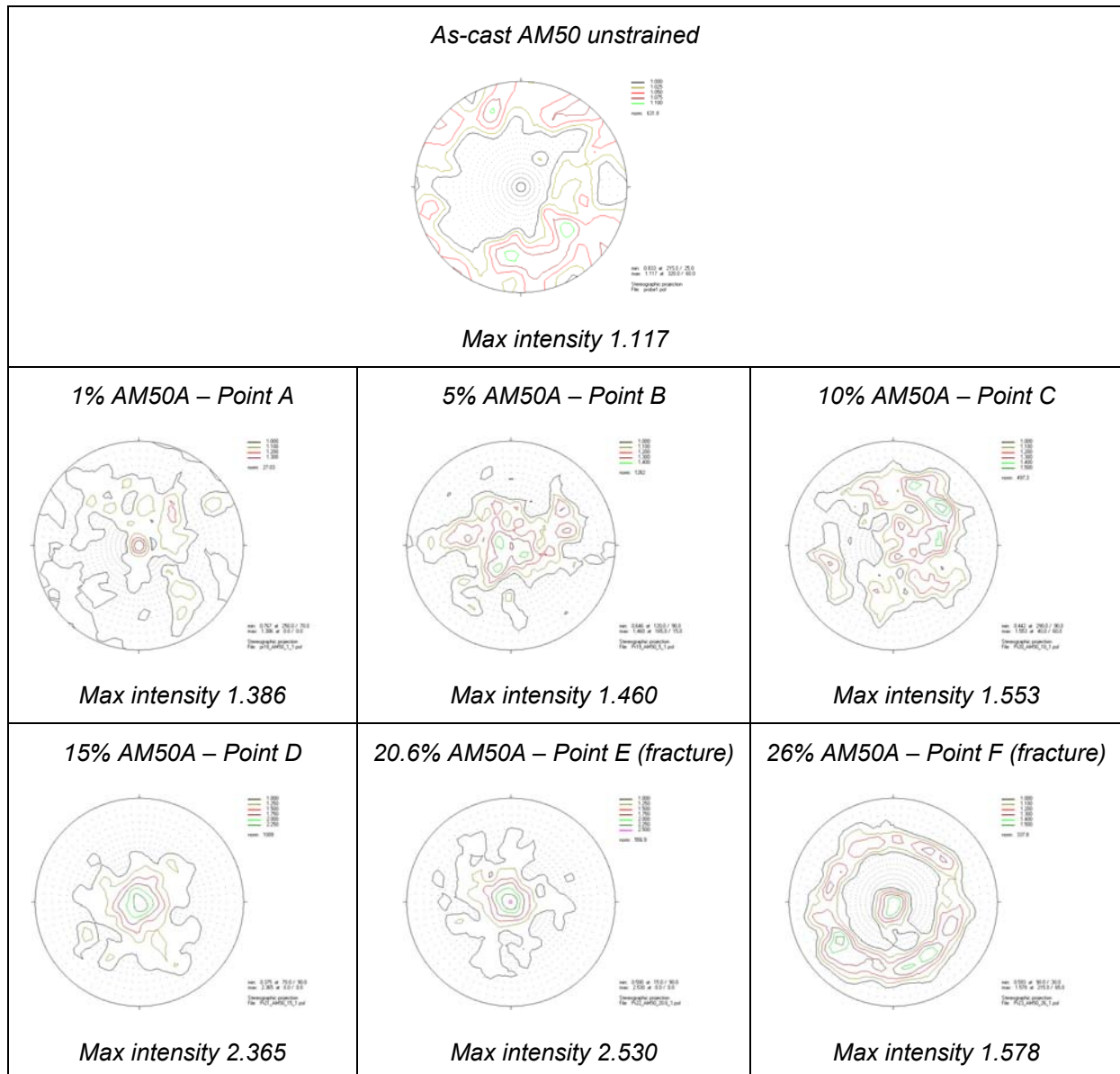


Figure 5.18. Pole figures for the diffraction peak  $\{10\bar{1} 0\}$  (Loading direction perpendicular).

A last analysis for obtaining more information about the deformation mechanisms was done with TEM images. The new AM50+Si+Sn alloy was used for this purpose. Piles of dislocation and twins were found after strain rate of  $1.5 \times 10^{-4} \text{ s}^{-1}$  but when strain rate was switched to  $0.1 \text{ s}^{-1}$  the apparition of some kind of subcells in the matrix could be observed (Figure 5.19).

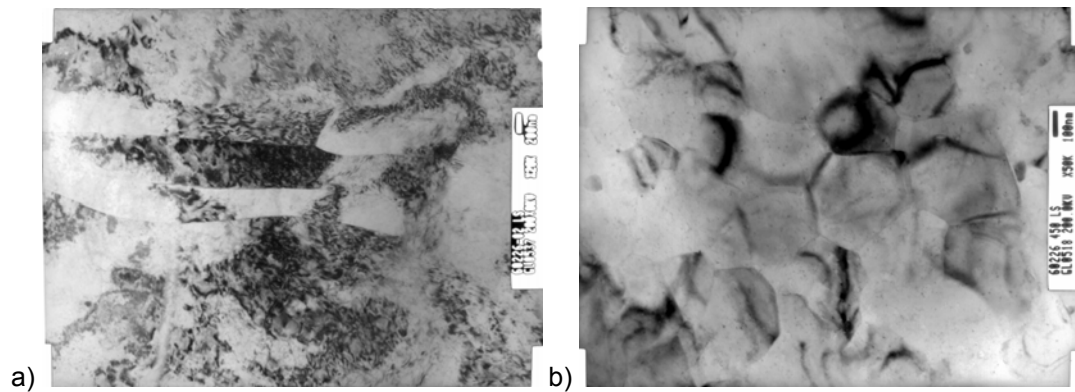


Figure 5.19. TEM images of the AM50+Si+Sn alloy; a) presence of piles up of dislocations and twins (strain rate of  $1.5 \cdot 10^{-4} \text{ s}^{-1}$ ); b) subcells in the matrix (strain rate of  $0.1 \text{ s}^{-1}$ ).

However, further study is needed for making any statement on this issue. The influence of the precipitates and the nature of dislocations and twins may be identified.

Summarising, the analysed cast samples had a random texture before deformation and in the final texture the  $(10\bar{1}0)$  planes were oriented perpendicular to the loading direction. The  $(0001)$  basal plane was oriented parallel to the loading direction as it has already been described in the literature review. However, the measured maximal intensities are inferior to the intensities measured in wrought alloys. As an example, Yi [Y105] measured intensities up to 5 m.r.d. after tensile testing in AZ31B magnesium sheets. In this thesis, the maximal intensities are up to 2.2 m.r.d in the  $(0002)$  pole figure, even at elongations of 26%. It seems that the texture formation in high-pressure die-cast materials is less than in materials having a initial texture like rolled sheets.

## 5.6 Summary and conclusions

The influence of the generated microstructure during casting and subsequent heat treatments is analysed in this chapter.

Optical microscopy and SEM were used for the identification of precipitates. The microstructure of each alloy was described and a trial to quantify the eutectic was performed. Image analysis technique is concluded not to be an accurate system to quantify the precipitates. The influence of the condition of the etchant and the difficulty to obtain the right contrast between the matrix and the eutectic increases the error of the measurement of the eutectic quantity up to 20%. This error is higher than the difference between one sample and another sample, and the values are not significant.

Grain sizes and porosity were also measured to obtain a correlation between grain sizes and the previously measured solidification curves. The grain size of MRI207S after T6 heat treatment increases and the final grain size is more than the double. Grain size of AZ91E instead decreases after heat treatment. The reason of this can be that the high amount of eutectic divides some dendrites in two, at least apparently. However, the same procedure is used in all the measurements, and therefore, the results are comparable. AZ91E grain sizes are above  $100 \mu\text{m}$ , while the grain sizes in MRI207S are around  $20\text{-}30 \mu\text{m}$  in as-cast condition and around  $50\text{-}60 \mu\text{m}$  after heat treatment. When comparing different technologies, it is usually supposed that sand-casting generates the largest grain

size. Nevertheless, it is not the case in this investigation. Other parameters influences the grain size including the mould material, the melt and mould temperature, the usage of freezers, the filling time and the grain refiners. Porosity in the HPDC test parts was around 5-10%. The porosity in the other technologies was less than 4%, being in most of the cases around 0.1% or even less.

Fractography analysis was performed to characterise the effect of the alloy and heat treatment in the fracture behaviour. HPDC alloys show a dimple fracture surface, and cleavage fracture was mainly observed in gravity casting alloys.

Finally, for a better understanding of the deformability of Mg alloys, texture is measured. Texture generation during tensile testing is in accordance with that observed in wrought magnesium alloys. The difference is the smaller intensity obtained in HPDC alloys than that in wrought alloys, even at similar elongations (around 20%). The difference can be due to the effect of a random initial texture of the cast sample or it can also be caused by the inhomogeneous microstructure. The mechanical properties of the high-pressure die-castings are determined by the fine-grain skin, which has a small volume in comparison with the middle zone. However, in this work, the texture is measured in the whole area for having the global behaviour. Then, the texture in the skin area can have a higher intensity than in the middle part but it can not be seen using neutron diffraction method. Other methods should be used in order to measure only the texture of the skin, for example X-rays. Moreover, it is concluded that the alloying elements do not have any effect in the generation of the texture in the two analysed alloys. Therefore, if the texture in the two alloys is equal, other parameters are the responsible of the increase of the mechanical properties of the AM50+Si+Sn alloy, such as the ability of the precipitates to pin dislocations.



## **CHAPTER 6 - ANALYSIS OF MECHANICAL PROPERTIES**



## 6 ANALYSIS OF MECHANICAL PROPERTIES

Once the solidification conditions and microstructures are identified, the third step consists of the measurement of mechanical properties. This is the last step to complete the values required for establishing correlations to predict mechanical properties. Tensile bars and test parts were tested for this reason and the obtained mechanical properties are presented in this chapter.

Another objective of this chapter is to validate the mechanical properties of the newly developed MRI207S and AM50+Si+Sn alloys for aeronautic applications. The intention is to replace components of commercial aircrafts actually made in aluminium with magnesium elements. Hence, results of mechanical properties of the newly developed magnesium alloys are compared with the sand-cast A357 alloy in T6 condition, which is the material actually used in the proposed applications in the IDEA EC project. The proposed applications in this project are a pedal and a housing, shown in Figure 6.1 [ARR07]. The pedal has a new design with a lightened geometry. The housing is a component attached to the pressure bulkhead subjected to cabin pressurization and supporting the flight control rod crank.

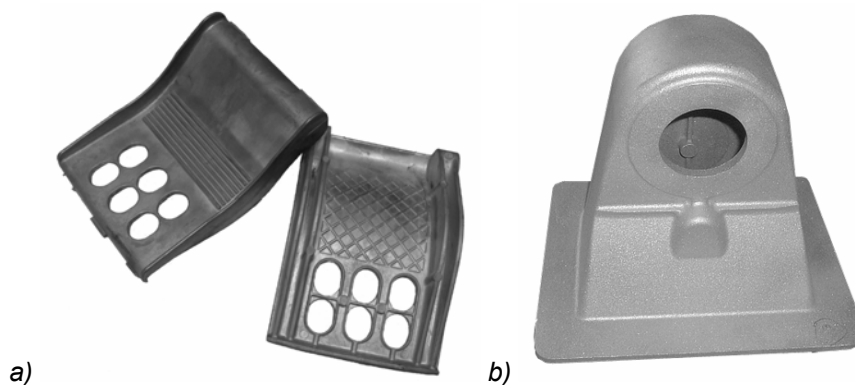


Figure 6.1. Proposed parts for substitution of aluminium components with magnesium in aircraft applications; a) pedals; b) housing [ARR07].

Israel Aerospace Industries (IAI) also defined the required mechanical properties to magnesium alloys for aeronautic applications. These properties are summarised in Table 6.1.

Table 6.1. Required mechanical properties in separately cast specimens for aeronautic applications defined by IAI [WEN05].

	TYS (MPa) <sup>a</sup>	UTS (MPa) <sup>b</sup>	A (%) <sup>c</sup>
<b>Requirement in separate cast specimens for Mg alloys</b>	220	290	3

<sup>a</sup> Tensile yield strength

<sup>b</sup> Ultimate tensile strength

<sup>c</sup> Elongation

The results of the new alloys are not only compared to the A357 aluminium alloy. Tensile properties of the new alloys are also compared to the properties of the commercial AZ91 and AM50 alloys. Then,

the results obtained in different samples and areas are put together with the values of solidification time and microstructure in chapter 7.

In addition to the tensile testing, Vickers microhardness tests were performed on the phases present in the AZ91E alloy. The objective was to analyse and characterise the effect of the precipitates in the mechanical properties.

### 6.1 Mechanical characterisation of the tensile bars

Separately cast tensile bars were produced and tested. Tensile bars give the properties of the material without being affected by the influence that the geometry has on real parts. The results obtained are given in Table 6.2. Figure 6.2 shows the tensile curves of sand-cast magnesium alloys in as-cast and heat treated conditions compared to the aluminium alloy A357 in T6 heat treated condition.

Table 6.2. Mechanical properties of the new alloys vs. commercial alloys of separately cast bars.

	UTS (MPa)	TYS (MPa)	A %
<b>SAND CASTING</b>			
A357-T6	322 ± 5	271 ± 6	4 ± 1.5
AZ91E-T6	287 ± 9	138 ± 8	6.3 ± 1.5
AZ91E-F	150 ± 5	111 ± 4	2.2 ± 0.4
MRI207S-T6	288 ± 11	218 ± 12	4 ± 1
MRI207S-F	216 ± 4	144 ± 5	5.8 ± 1
<b>INVESTMENT CASTING</b>			
AZ91E-T6	235 ± 4	127 ± 4	4 ± 1
AZ91E-F	137 ± 4	94 ± 3	1.25 ± 0.2
MRI207S-T6	285 ± 3	215 ± 3	3 ± 0
MRI207S-F	205±12	132±3	6.3±1.7
<b>GRAVITY DIE-CASTING</b>			
AZ91E-T6	209 ± 14	112 ± 12	3.2 ± 0,8
AZ91E-F	155 ± 7	94 ± 4	1.8 ± 0.4
MRI207S-T6	265 ± 15	203 ± 2	3 ± 1
MRI207S-F	205 ± 13	144 ± 5	5.9 ± 1,7
<b>HIGH PRESSURE DIE-CASTING</b>			
AZ91D	268 ± 10	165 ± 5	7 ± 3
AM50A	252 ± 10	135 ± 1	18 ± 4
AM50+Si+Sn	270 ± 2	145 ± 1	17 ± 1



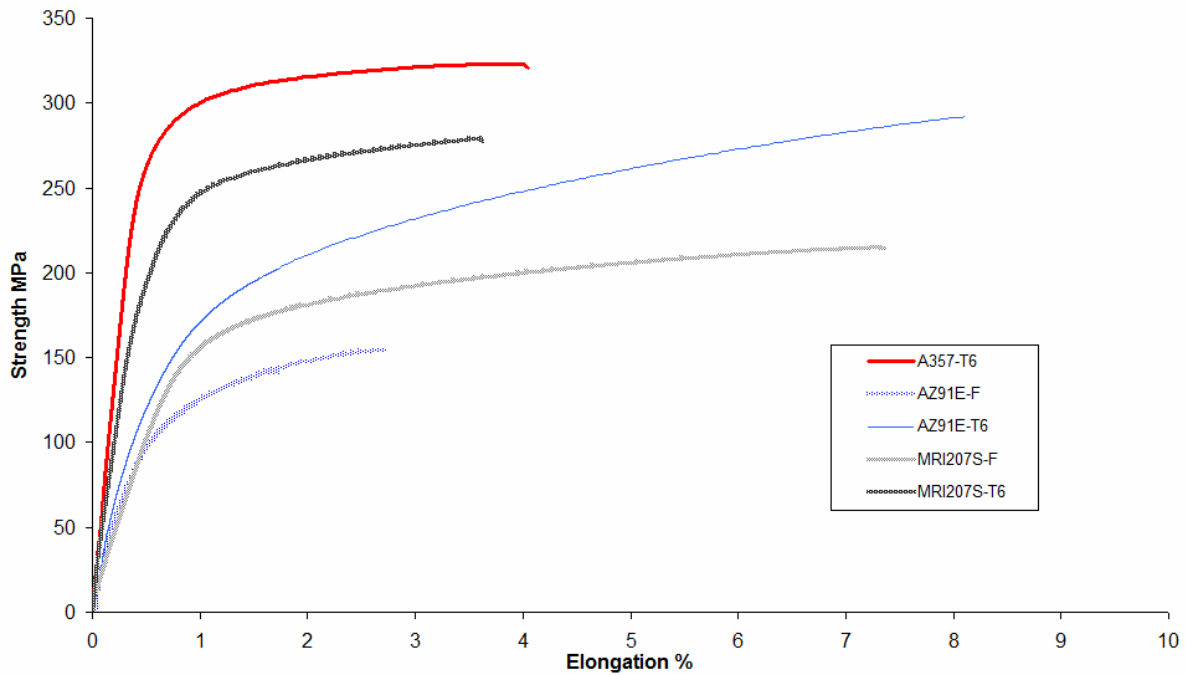


Figure 6.2. Tensile curves in sand cast magnesium alloys compared to aluminium A357 alloy.

Sand-cast aluminium A357 alloy was characterised in order to compare the values of aluminium alloys to magnesium alloys. The mechanical properties of MRI207S alloy are close to the properties of the aluminium alloy after heat treatment if they are compared to the mechanical properties of other magnesium cast alloys. Therefore, it was concluded that it is a promising alloy for substituting for aluminium when strength is an important issue. Moreover, the values of the MRI207S alloy after T6 heat treatment reach the requirements given by IAI (Table 6.1) for aeronautic applications. In comparison, looking at the values given in Table 6.2, it should be noted that the properties of investment-cast and gravity die-cast alloys are lower than these of sand-cast alloys. This is due to a higher presence of defects like oxides, inclusions and porosity. Even if the quality of the investment-cast tensile bars could be considered acceptable, the quality of the gravity die-cast bars is poor. Thus, the mechanical properties presented in this document should only be considered as trends of the behaviour of the alloys. In conclusion, the use of filters and a more adequate metal handling procedure should be employed for achieving good quality castings in gravity die-casting.

In the graphic representation the improvement of mechanical properties of AZ91E after heat treatment can be easily noted. This is due to the dissolution of the brittle continuous  $\gamma$ -Al<sub>12</sub>Mg<sub>17</sub> phase into a less brittle lamellar pearlitic structure. Therefore, the brittleness is reduced giving a higher ductility and the strength is increased due to solid solution and precipitation hardening.

The MRI207S alloy does not have the brittle behaviour of the AZ91E alloy in as-cast condition. The heat treatment leads to an increment in strength despite of a decrease in ductility. T6 heat treatment generates solid solution hardening with a posterior precipitation hardening. Even though, with a lesser strength, the properties of MRI207S-T6 are approaching the values of the aluminium A357 alloy.

Values obtained in HPDC tensile bars are also shown in Table 6.2. The addition of Si and Sn to the AM50 alloy increased the strength and kept the ductility constant. The high ductility and improved strength of this alloy can be interesting for aeronautic and automotive applications. At the end of the IDEA project IAI replaced the pedals made in aluminium for magnesium HPDC pedals. The requirements that they proposed in the separately cast tensile specimens could not be reached by HPDC. IAI established the requirements for the magnesium alloys based on the properties of the actually used aluminium alloys for an easier substitution of the parts from one material to the another. In any case, the magnesium HPDC pedals were tests in service and they passed all the required tests. This way, it was shown that the aluminium pedals were oversized and magnesium HPDC pedals were accepted for the substitution of the ones made in aluminium.

## 6.2 Mechanical characterisation of the test parts

Samples excised from the areas S1 to S4 of the test parts described in chapter 3 were tested. There is a high level of porosity and inclusions in the S1 and S2 areas (see chapter 3), causing a premature fracture of the samples. Therefore, the values obtained in these areas are not reliable and are rejected and only the areas of S3 and S4 considered. The mechanical properties measured in the test parts are influenced by the presence of porosity inside the castings, which is also expected in real castings. For more information about the measured porosity levels see chapter 5. Table 6.3 shows the results obtained in the test parts for different technologies, alloys, and heat treatment conditions in the S3 and S4 areas.

Table 6.3. Mechanical properties of the new alloys vs. commercial alloys of test parts.

	UTS (MPa)	TYS (MPa)	A %
<b>SAND CASTING</b>			
<b>AZ91E-T6</b>	245±5	162±6	4.4±0.5
<b>AZ91E-F</b>	168±5	122±5	4±0,4
<b>MRI207S-T6</b>	290±6	210±2	5.5±1
<b>MRI207S-F</b>	216±8	147±7	4.4±1
<b>INVESTMENT CASTING</b>			
<b>AZ91E-T6</b>	96±6	-	1.4±0.4
<b>MRI207S-T6</b>	249±5	205±10	0.8±0.2
<b>MRI207S-F</b>	172±12	107±12	1.6±0.5
<b>GRAVITY DIE-CASTING</b>			
<b>AZ91E-T6</b>	211±8	165±6	2.7±0.2
<b>MRI207S-T6</b>	292±3	213±2	4.7±0.6
<b>HIGH PRESSURE DIE-CASTING</b>			
<b>AZ91D</b>	129 ± 1	52 ± 0.5	1.6 ± 0.1

The results obtained in the gravity die-cast test parts are promising. The tensile bars produced with this technology did not reach the expected values because of a non-adequate design of the mould and melting procedure. However, the high tensile values obtained in the test part mean that this process is

a promising candidate for magnesium because the test part is a difficult part to cast due to the differences in thickness. Gravity die-casting has some advantages compared with sand-casting. Some of these advantages are a better surface quality and a smaller grain size as a result of a higher cooling rate. By decreasing the grain size in Mg-alloys the mechanical properties are increased following the Hall-Petch relationship.

The investment casting process is interesting due to the better surface quality compared to sand-casting. It also allows us to cast geometries which are not possible to obtain with gravity die-casting. The investment cast MRI207S test parts were on an acceptable level, but the quality of AZ91E castings was poor. There was a high presence of oxides in the investment-cast AZ91E test-parts.

The mechanical properties of test parts produced by HPDC were unacceptable. The reason was the high porosity content generated by the turbulent flow and fast solidification. Furthermore, due to the machining of the samples, the outer surface was removed, which is usually a defect free and small grain sized surface. Therefore, bad mechanical properties were obtained. The specimens were machined out from the thick areas, where the porosity level was highest. The test part is a non-adequate geometry especially for HPDC, with irregular and thick wall thickness, up to 20 mm. The microstructural analysis also showed large porosity areas (Figure 6.3).

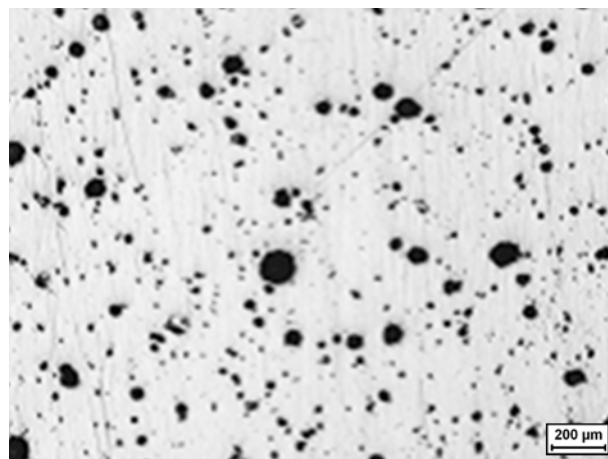


Figure 6.3. Porosity in the HPDC AM50 test part (Position S3).

### 6.3 Hardness measurements

In order to compare the difference in hardness between the  $\alpha$ -Mg and the  $\gamma$ -Al<sub>12</sub>Mg<sub>17</sub> phases, Vickers microhardness measurements were performed in the AZ91E alloy after heat treatment. Four indentations were made in the sand-cast AZ91E alloy. One was in the  $\alpha$ -Mg area. Two indentations were made in the pearlitic  $\alpha$ -Mg with  $\gamma$ -Al<sub>12</sub>Mg<sub>17</sub>. The difference between them was that the lamellar spacing was different. The third indentation was performed in a mixed area with half the indentation in  $\alpha$ -Mg and half in the pearlitic zone. The indentations are listed in Table 6.4. The indentations are shown in Figure 6.4, together with the hardness values measured and the dimensions of the indentations ( $d$  is the average value).

Table 6.4. Description and values of the indentations in the AZ91E alloy.

	Description	HV value	Figure
a	Indentation in $\alpha$ -Mg	27	Figure 6.4a
b	Indentation in pearlitic $\alpha$ -Mg with $\gamma$ -Al <sub>12</sub> Mg <sub>17</sub> where the lamellar spacing was small (the two phases were hardly distinguished at a magnification of x1000)	103	Figure 6.4b
c	Indentation in pearlitic $\alpha$ -Mg with $\gamma$ -Al <sub>12</sub> Mg <sub>17</sub> where lamellar distance was bigger (the lamellar layers were easily distinguished at a magnification of x1000)	96	Figure 6.4c
d	Indentation half in $\alpha$ -Mg and half in pearlitic $\alpha$ -Mg with $\gamma$ -Al <sub>12</sub> Mg <sub>17</sub>	82	Figure 6.4d

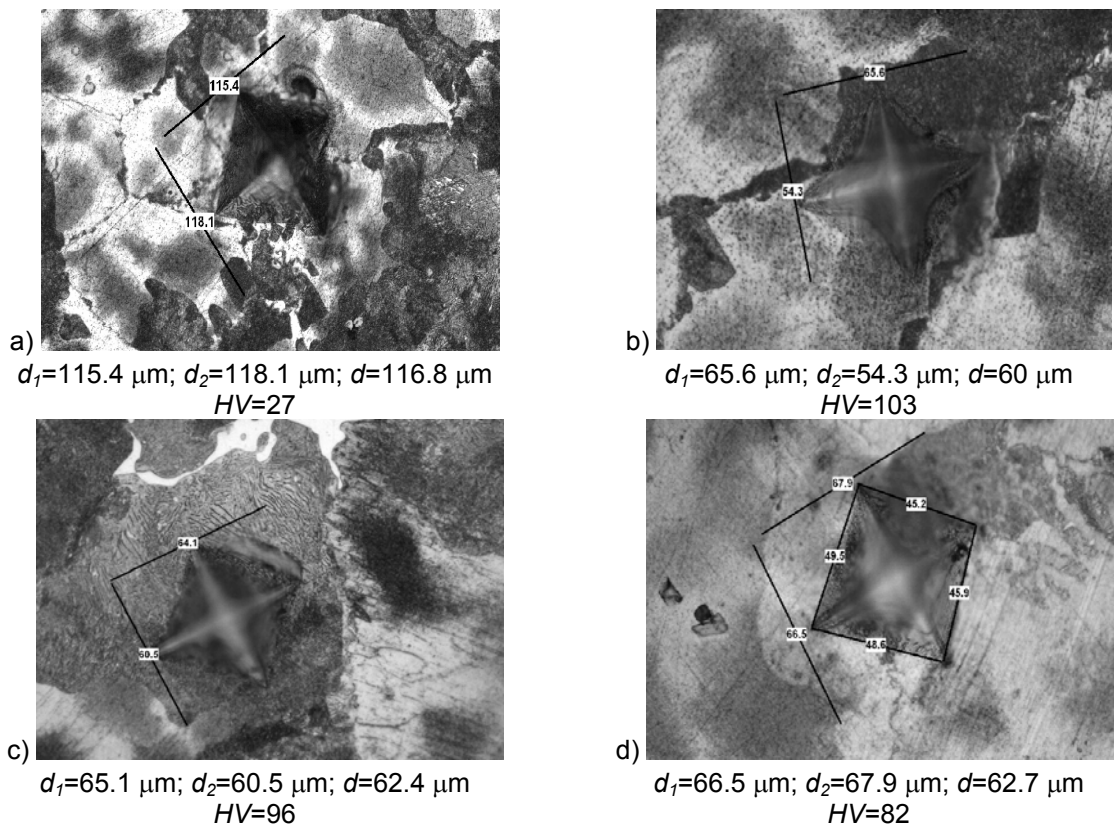


Figure 6.4. Vickers indentation in different areas of the AZ91E alloy.

As expected, the hardness in the  $\alpha$ -Mg matrix is lower than in the pearlitic area. However, one of the main conclusions taken from this analysis is the influence that the distance between layers has in the hardness of the pearlitic area. When the distance between the layers is smaller, the hardness increases. This makes it difficult to establish correlations between the amount of precipitated pearlitic and mechanical properties. The lamellar distance in the microstructure of AZ91E is not constant. Therefore, it is difficult to count the amount of the pearlitic phase with a concrete lamellar thickness in

a casting. In this work, it is suggested that other solutions may be taken for the establishment of correlations between precipitates and mechanical properties, because the amount and morphology of the phases is not constant in one zone.

#### 6.4 Summary and conclusions

Tensile characterisation of tensile bars and test parts is presented and discussed in this chapter.

MRI207S alloy after T6 heat treatment approaches the values of the A357-T6 aluminium alloy. This alloy also fulfils the requirements proposed by IAI to magnesium castings for aeronautic applications. Therefore, this is a promising candidate to be integrated in aeronautic applications. The new AM50+Si+Sn alloy has improved mechanical properties compared to its predecessor AM50 alloy. The strength is higher and the ductility is kept constant. Even if the mechanical properties do not fulfil IAI's requirements in separately cast test parts, Israel Aerospace Industries tested successfully HPDC magnesium pedals in the frame of the IDEA project. They replaced aluminium pedals for magnesium HPDC pedals in business aircrafts as a result.

Looking in more detail, all the castings produced with sand-casting have better values compared to the other technologies. The main reason is the large experience of magnesium sand-casting by the foundry. The magnesium sand-castings analysed in this project are high quality parts, with homogeneous microstructure and mostly free of defects, presenting superior mechanical properties. Values taken from this chapter are used for the establishment of Hall-Petch relationship.

Finally, hardness measurements were performed in order to obtain further information about the material. Microhardness measurements give an idea of the properties of the principal phases. The hardness of the pearlite changes with the lamellar spacing, increasing the hardness when the lamellar spacing decreases. In the pearlitic  $\alpha$ -Mg/ $\gamma$ -Al<sub>12</sub>Mg<sub>17</sub>, the lamellar spacing affects the mechanical properties and the lamellar spacing is not constant in the same area of the sample. This makes it difficult to establish any relationship between the solidification rate and the precipitated eutectic. It was then decided that counting the amounts of the precipitates is not a feasible way for integrating the effect of the precipitates in the mechanical properties for the AZ91E alloy. Other alternatives may be considered for the integration of second phases in the correlations between microstructures and mechanical properties. For future works it is proposed to correlate the microhardness of the matrix instead. The microhardness of the matrix is dependent of the precipitation of intermetallics, which is dependent of the solidification rate and posterior heat treatments. The microhardness of the matrix is a single variable to take into account, which gives an accurate idea of the properties of the material. If this property could be predicted from the solidification curves and posterior heat treatments and integrated in the equations for the prediction of mechanical properties, the effect of the precipitates in the mechanical properties would also be integrated.



**CHAPTER 7 - CORRELATIONS BETWEEN SOLIDIFICATION TIME,  
MICROSTRUCTURE AND MECHANICAL PROPERTIES**





## 7 CORRELATIONS BETWEEN SOLIDIFICATION TIME, MICROSTRUCTURE AND MECHANICAL PROPERTIES

In this chapter the results obtained previously are contrasted and correlations between them are discussed and analysed. Solidification times, microstructures and mechanical properties for magnesium alloys are related as shown in Figure 7.1. The relationships are represented by arrows.

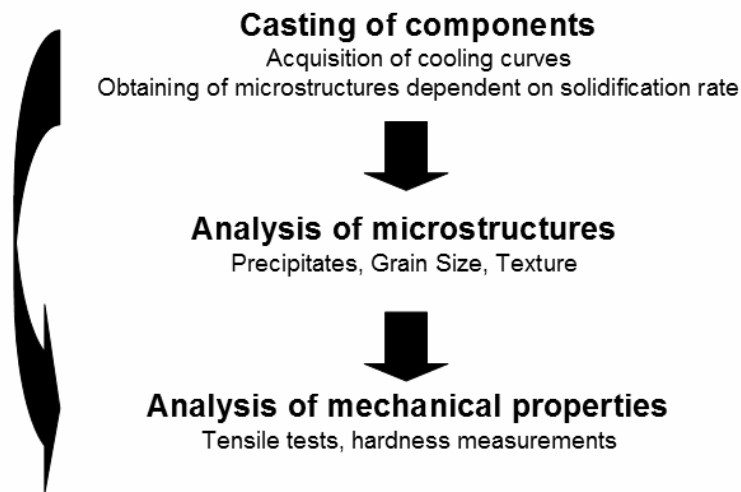


Figure 7.1. Diagram highlighting the steps of the overall work plan.

Correlations proposed by Flemings [Eq. 7.1, FLE74] are employed for the prediction of grain size from local solidification times. In addition, Hall-Petch relationships [Eq. 7.2, HAL51, PET53] are used for the prediction of mechanical properties from grain sizes. The generation of the precipitates and their influence on mechanical properties is not taken into account in these correlations. In previous chapters, it is explained that an accurate measurement of precipitates and their morphology is not obtained in this work. The difficulty resides in the variability of the morphology and the influence of the etchant. The difficulty comparing to binary alloys increases in multicomponents alloys, such as the ones analysed in this work. Nevertheless, the selected equations give accurate values when the solidification and heat treatment conditions are similar. These equations can also be easily integrated in numerical simulation methods for the prediction of mechanical properties in castings, which is the main objective of the equations in this work. These equations are summarised in Table 7.1. The results obtained in AZ91E alloy are compared to the constants taken from literature for the validation of the employed procedure. Furthermore, the constants  $a$ ,  $b$ ,  $n$ ,  $\sigma_0$  and  $k$  are defined for the new MRI207S alloy so they can be integrated in simulation softwares.

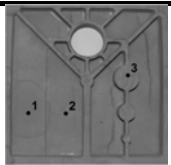
Table 7.1. Equations employed for the prediction of grain size and tensile yield strength.

Prediction of grain size	$d = a \cdot t_s^n = b \left( \frac{\Delta T_s}{t_s} \right)^{-n}$	Eq. 7.1
Prediction of tensile yield strength	$\sigma_y = \sigma_0 + kd^{-1/2}$	Eq. 7.2

### 7.1 Correlation between solidification curves and microstructures

Once the solidification times and the grain sizes were measured, correlations between them were established. The cooling rate was also compared to the grain size. However, the solidification time and the cooling rate are related and the results are equivalent. The definition of the cooling rate is given in the literature review (Eq. 2.5). Table 7.2, Table 7.3 and Table 7.4 summarise the data taken from the cooling curves. The data is put together with the measured grain sizes for the AZ91E and MRI207S tensile bars, test parts and prototypes. As it was explained in chapter 6, grain sizes in some point were not measured. In some test parts, part of the casting was used for other measurements and some of the points were not available. Therefore, some of the grain sizes are missing in the tables below.

Table 7.2. Solidification time, cooling rate and grain size of the sand, investment and gravity die-cast AZ91E test-parts produced in the foundries (average values).

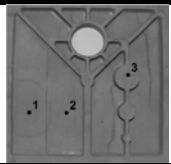
AZ91E alloy Casting of the test part in the foundries		Solidification time $t_s$ (s)	Cooling rate $\left  \frac{\dot{T}}{T} \right $ (°C/s)	Grain size ( $\mu\text{m}$ )	
				As-cast	T6
Sand-casting PSFA	Point 1	86.9	1.82	- <sup>a</sup>	- <sup>a</sup>
	Point 2	77.9	2.17	96	84
	Point 3	45.0	3.6	99	86
Investment-casting PIFA	Point 1	45.7	3.74	- <sup>a</sup>	154
	Point 2	47.5	3.62	- <sup>a</sup>	- <sup>a</sup>
	Point 3	41.7	4.07	- <sup>a</sup>	- <sup>a</sup>
Gravity die-casting PGFA	Point 1	45.7	3.65	- <sup>a</sup>	89
	Point 2	47.5	3.66	- <sup>a</sup>	- <sup>a</sup>

<sup>a</sup> not available

Table 7.3. Solidification temperatures and times of the investment-cast AZ91E tensile bars and components produced in MGEP.

AZ91E alloy	Placement	Solidification time $t_s$ (s)	Cooling rate $\left  \frac{\dot{T}}{T} \right $ ( $^{\circ}\text{C/s}$ )	Grain size ( $\mu\text{m}$ ) As-cast
Investment casting of tensile specimens TIMA10	Point 1	437.5	0.41	118
	Point 2	375.5	0.46	127
	Point 3	316.5	0.54	112
Investment casting of tensile specimens TIMA11	Point 1	364	0.47	133
	Point 2	345	0.51	120
	Point 4	369.5	0.31	127
Investment casting of components CIMA01	Point 1	555	0.31	166
	Point 2	421.5	0.40	154

Table 7.4. Solidification temperatures and times of the sand, investment and gravity die-cast MRI207S test-parts produced in the foundries (average values).

MRI207S alloy		Solidification time $t_s$	Cooling rate $\left  \frac{\dot{T}}{T} \right $ ( $^{\circ}\text{C/s}$ )	Grain Size	
				As-cast	T6
Sand-casting PSFM	Point 1	19.8	5.2	28	- <sup>a</sup>
	Point 2	14.8	7.2	29	- <sup>a</sup>
	Point 3	12.8	8.3	23	- <sup>a</sup>
Investment-casting PIFM	Point 1	34.5	3.1	44	63
	Point 2	36.4	2.9	45	56
	Point 3	23.4	4.5	- <sup>a</sup>	- <sup>a</sup>
Gravity die-casting PGFM	Point 1	24.0	4.4	- <sup>a</sup>	- <sup>a</sup>
	Point 2	24.3	4.5	- <sup>a</sup>	- <sup>a</sup>

<sup>a</sup> not available

From the data above, graphs relating grain size to solidification time or cooling rate were established. Next, potential tendency curves were constructed for each group of values. Potential curves are required because the equation proposed by Flemings (Eq. 7.1) defines a potential relationship between the cooling rate or solidification time and grain size or arm spacing.

Once the tendency curves were constructed, the data obtained was validated with values from literature [CAC02a, DUB98, SEQ97 and LAB97]. Figure 7.2 shows the relationship obtained between the cooling rate and the grain size or secondary arm spacing. The data from literature refers to secondary arm spacing and the measured data in this work to grain size. Most authors use the equation given by Flemings (Eq. 7.1) with secondary arm spacing. The reason is the dendritic structure they obtain. In a dendritic microstructure, the secondary arm spacing is what can easily be measured. However, in this thesis, it was decided to use it with grain sizes because of two reasons. The first reason is that the Hall-Petch equation (Eq. 7.2) relates grain size to the yield strength. Then, it is more adequate to only use one variable in the whole procedure when establishing correlations.

The second and most important reason is that the MRI207S alloy does not show a dendritic structure because its microstructure is globular. Since the equation of Flemings is also valid when grain size is used instead of secondary arm spacing, it was decided to use it with grain sizes for this work. The literature values are only used to validate the tendencies of the two curves. As expected, the SDAS curves from literature go under the values from grain size in this work. More importantly, the tendencies of all the curves are similar, which makes the measured values coherent. The problem found when constructing the potential curves with the measured data was the high dispersion in the values of the AZ91E alloy ( $R^2=0.6$ ). This is due to the fact that all the parts were not cast in the same installations. Some castings were performed in industrial furnaces with high capacity. In contrast, some of them were cast in MGEP, where a laboratory small crucible was used for the melting of the alloy. In small crucibles the mixing of the grain refiner is never as good in big crucibles, where a better homogeneity is obtained. This may lead to a different treatment of the alloy, and to some differences in the generation of grain size for a specific cooling rate. The formula proposed for AZ91E can be discussed because the accuracy of the calculated grain size depends on the employed crucible and the efficiency of the grain refiners. Several grain refiner methods are used for the AZ91E alloy commercially, and therefore, the equation formulated by Flemings should be applied carefully. This equation is valid when the quantity and kind of grain refiners and the procedure are kept constant. The dispersion found in the data taken from literature can also be justified by the same reason. The four cited works [CAC02a, DUB98, SEQ97 and LAB97] differ in the prediction of the secondary arm spacing as can be seen in Figure 7.2. The dispersion of values in the correlations proposed by [DUB98] and [SEQ97] is of about 60%. A considerable dispersion is also found in this study when establishing the correlation between the solidification time and grain size for the AZ91E alloy. The alloys cast in the foundries and the ones cast in the laboratory installations at MGEP show a similar tendency, being the dispersion when plotting a potential curve with the values considerable. The procedure and grain refiners for MRI207S alloy are however well established, and the predictions calculated in this work for the MRI207S alloy are accurate ( $R^2=0.93$ ). Therefore, the equation proposed by Flemings is considered acceptable for the MRI207S alloy. The equation proposed for AZ91E, despite, should be employed with precaution, being the results sensitive to the melting procedure.

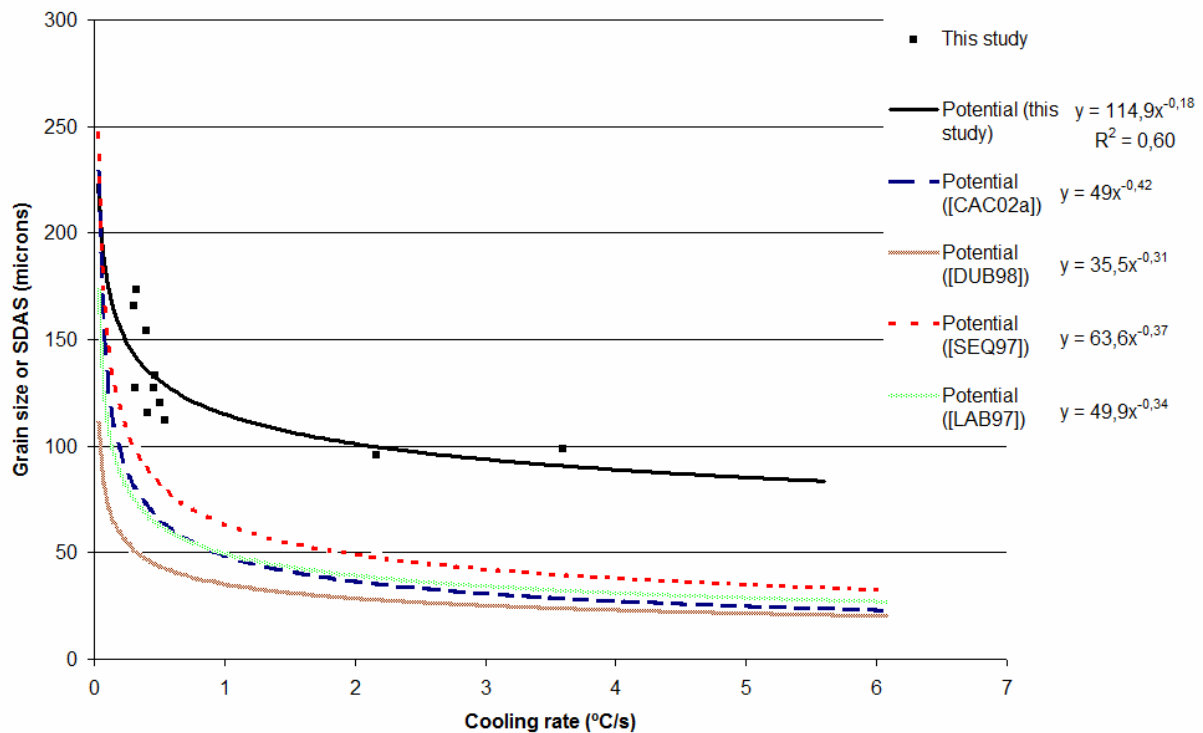


Figure 7.2. Correlation between cooling and grain size or secondary arm spacing for AZ91E. Values taken from literature and from this work show the same tendency. This study refers to grain size and literature [CAC02a, DUB98, SEQ97 and LAB97] refers to secondary arm spacing.

Figure 7.3 and Figure 7.4 show only the curves obtained in this work, which are for the AZ91E and MRI207 alloys. The relationship established for the correlation between solidification time or cooling rate and grain size are also given in those figures. In those equations  $y$  equals to grain size ( $d$ ) and  $x$  is the solidification time ( $t_s$ ) or the cooling rate ( $\dot{T}$ ) in absolute values. The dispersion for the MRI207S is small. All the MRI207S castings were produced in industrial furnaces and consequently, in similar conditions. Therefore, a good coherency of the results is obtained contrary to the case of the AZ91E alloy where the dispersion is bigger.

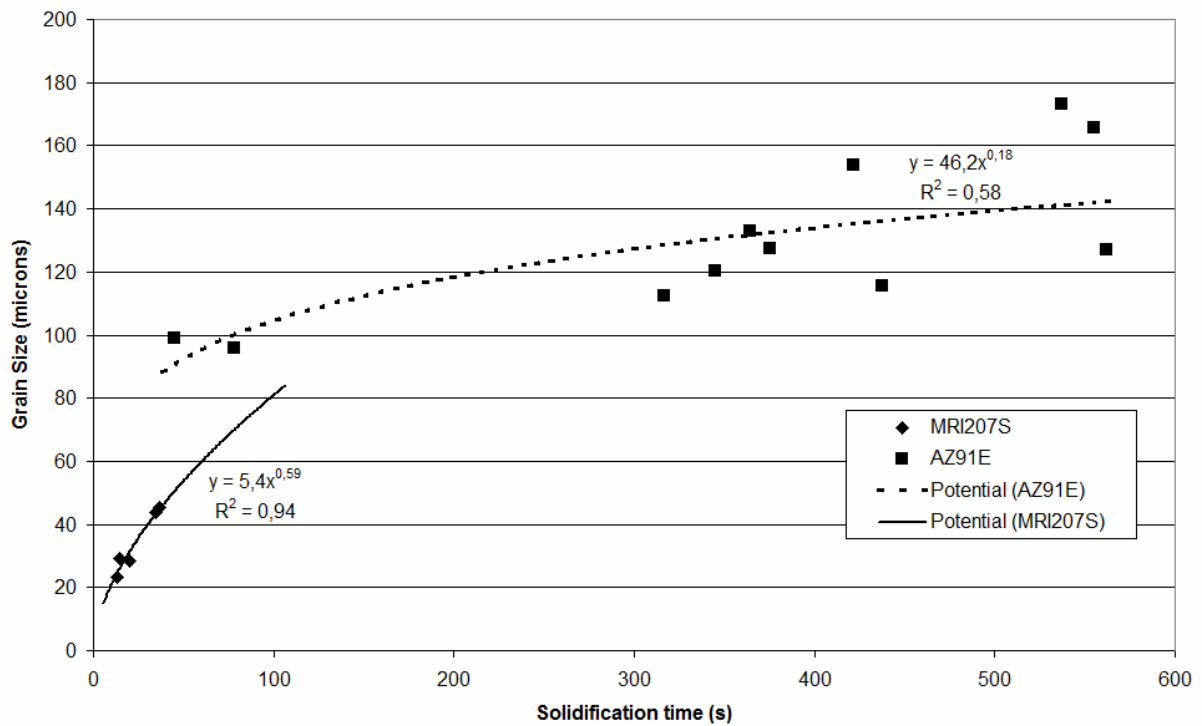


Figure 7.3. Relationship between solidification time and grain size for AZ91E and MRI207S alloys.

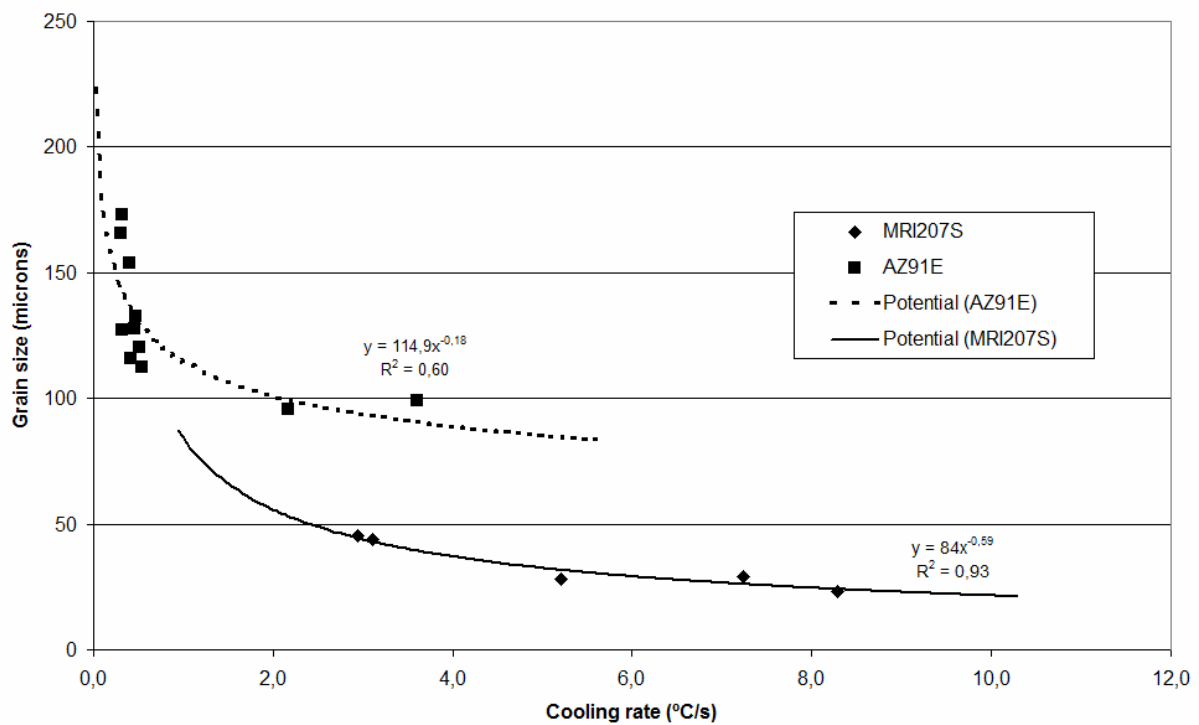


Figure 7.4. Relationship between solidification rate and grain size for AZ91E and MRI207S alloys.

The relationships between solidification time or cooling rate and grain size shown in the above figures are summarised in Eq. 7.3, Eq. 7.4, Eq. 7.5 and Eq. 7.6.

$$d_{AZ91E} = 46.2t_s^{0.18} \quad \text{Eq. 7.3}$$

$$d_{MRI207S} = 5.4t_s^{0.59} \quad \text{Eq. 7.4}$$

$$d_{AZ91E} = 114.9 \left| \dot{T} \right|^{-0.18} \quad \text{Eq. 7.5}$$

$$d_{MRI207S} = 84 \left| \dot{T} \right|^{-0.59} \quad \text{Eq. 7.6}$$

In these equations, the exponent value for AZ91E alloy is lower than the one proposed by Flemings [FLE74]. Flemings proposed a value of about  $\frac{1}{2}$  for primary arm spacing without further explanation or demonstration. He only refers to a study with ferrous alloys. This value is generic and it is not specific for magnesium alloys, even if the value of MRI207S alloy is close to it. Furthermore, the simplicity of this equation should be considered when analysing these differences. In order to have a more accurate relationship, parameters like the thermal gradient, the diffusion coefficient in liquid, the Gibbs-Thomson coefficient, the concentration of the solute, the liquidus slope, the segregation coefficient and the interface velocity for example should be integrated. More information about these relationships can be found in the literature review. The complexity in obtaining all the above mentioned data makes the use of detailed relationship difficult. However, the results obtained by equation such as the one proposed by Flemings and used in this work are good enough to predict the material behaviour.

## 7.2 Correlation between microstructures and mechanical properties

In this section Hall-Petch parameters are defined for the AZ91E and MRI207S alloys in as-cast and heat-treated conditions.

First of all, the data obtained in chapters 5 and 6 is correlated. This data is shown in Table 7.5. Mechanical properties of tensile bars and test parts are shown together with measured grain sizes ( $d$ ) and porosity levels for each area. In addition, the value of  $d^{-1/2}$  is given for establishing Hall-Petch parameters. Some values from the test part are not considered because these had high impurity and/or porosity content which lead to a premature failure.

Table 7.5. Mechanical properties and measured microstructural parameters.

Technology	Geometry	Nom.	Alloy and heat treatment	UTS (MPa)	TYS (MPa)	A (%)	Grain size $d$ ( $\mu\text{m}$ )	Porosity (%)	$d^{1/2}$ ( $\text{m}^{-1/2}$ )
Sand-casting	Tensile bar	TSFA	AZ91E – F	150	111	2.2	121		91
Gravity die-casting		TGFA	AZ91E – F	155	94	1.8	223		67
Sand Casting	Test part	PSFA	AZ91E – F	193	147	4	96	0.1	102
Sand Casting	Tensile bar	TSFA	AZ91E – T6	287	138	6.3	109		96
Investment-casting		TIFA	AZ91E – T6	235	127	4	234		65
Gravity die-casting		TGFA	AZ91E – T6	209	112	3.2	180		75
Sand Casting	Test part	PSFA	AZ91E – T6	245	162	4.4	84	0.1	109
Gravity die-casting		PGFA	AZ91E – T6	211	165	2.7	89	0.4-3	106
Sand-casting	Tensile bar	TSFM	MRI 207S – F	216	144	5.8	29		184
Investment-casting		TIFM	MRI 207S – F	205	132	6.3	33		174
Gravity die-casting		TGFM	MRI 207S – F	205	144	5.9	26		196
Sand Casting	Test part	PSFM	MRI 207S – F	216	147	4.4	28	0.3	188
Investment Casting		PIFM	MRI 207S – F	172	107	1.6	44	0.3	151
Sand-casting	Tensile bar	TSFM	MRI 207S – T6	288	218	4	49		143
Investment-casting		TIFM	MRI 207S – T6	285	215	3	59		130
Gravity die-casting		TGFM	MRI 207S – T6	265	203	3	51		140
Investment Casting	Test part	PIFM	MRI 207S – T6	249	205	0.8	63	0.3	126

Prior to establishing relationships for the MRI207S alloy, the values obtained for the AZ91E are verified. The measured tensile yield strength (TYS) of AZ91E is compared to the data from the literature presented in chapter 2. Hall-Petch parameters from literature [COU66 and SAS96 in CAC02a] for sand and gravity die-cast AZ91E are taken for this comparison. Sand-cast values are applied for investment-cast AZ91E alloy due to the lack of information in literature. Next, the yield strength is calculated using the measured grain size at each sample in this work and applying the Hall-Petch equation to obtain a calculated YYS. These values are compared to the experimentally measured yield strength in tensile tests in Table 7.6. This table shows the calculated tensile yield strength using the Hall-Petch equation with the constants from the literature and the measured values in tensile tests. A good correlation is found between the measured and calculated values.



Table 7.6. Comparison of calculated TYS using Hall-Petch relationships and data collected in the literature with the measured TYS.

Technology	Geometry	Nom.	Alloy	$\sigma_0$ (MPa) <sup>a</sup>	$k$ (MPa m <sup>-1/2</sup> ) <sup>a</sup>	Grain size ( $\mu\text{m}$ )	Calculated TYS (MPa) <sup>b</sup>	Measured TYS (MPa) <sup>c</sup>
Sand Casting	Tensile bar	TSFA	AZ91E-F	66	0.42	121	104	111
Gravity die-casting		TGFA	AZ91E-F	53	0.32	223	74	94
Sand Casting	Test part	PSFA	AZ91E-F	66	0.42	95.7	109	122
Sand Casting	Tensile bar	TSFA	AZ91E-T6	84	0.6	109	141	138
Investment-casting		TIFA	AZ91E-T6	84	0.6	234	123	127
Gravity die-casting		TGFA	AZ91E-T6	77	0.48	180	113	112
Sand Casting	Test part	PSFA	AZ91E-T6	84	0.6	84	149	162

<sup>a</sup> Data taken from [COU66 and SAS96 in CAC02a]

<sup>b</sup> Calculated value with the Hall-Petch equation.  $\sigma_0$  and  $k$  are taken from [COU66 and SAS96 in CAC02a] and the grain size value is the measured value in this work

<sup>c</sup> Measured TYS in tensile tests

Once the measurements were validated, the values were plotted in a chart. Figure 7.5 shows the tensile yield strength (TYS) as a function of  $d^{1/2}$  for AZ91E and MRI207S. The tendencies shown in literature [COU66 and SAS96 in CAC02a] are marked for AZ91E in order to validate the results in this work. For each condition (as-cast and T6), the area is marked by an upper line with the values for sand-cast AZ91 [COU66 in CAC02a] and a lower line with the values for gravity die-cast AZ91 [SAS96 in CAC02a]. The tendency lines obtained for MRI207S are also illustrated. The tendency lines are constructed using different weights for values obtained from tensile bars and values obtained from test parts. The mechanical properties of test parts are influenced by typical defects in components, such as porosity and inclusions. Tensile bars are cast in optimised dies in order to create a defect free tested area. The applied difference of weight was 1/6. This means that the values of tensile bars count 6 times more than the values of the test part when approaching the tendency line.

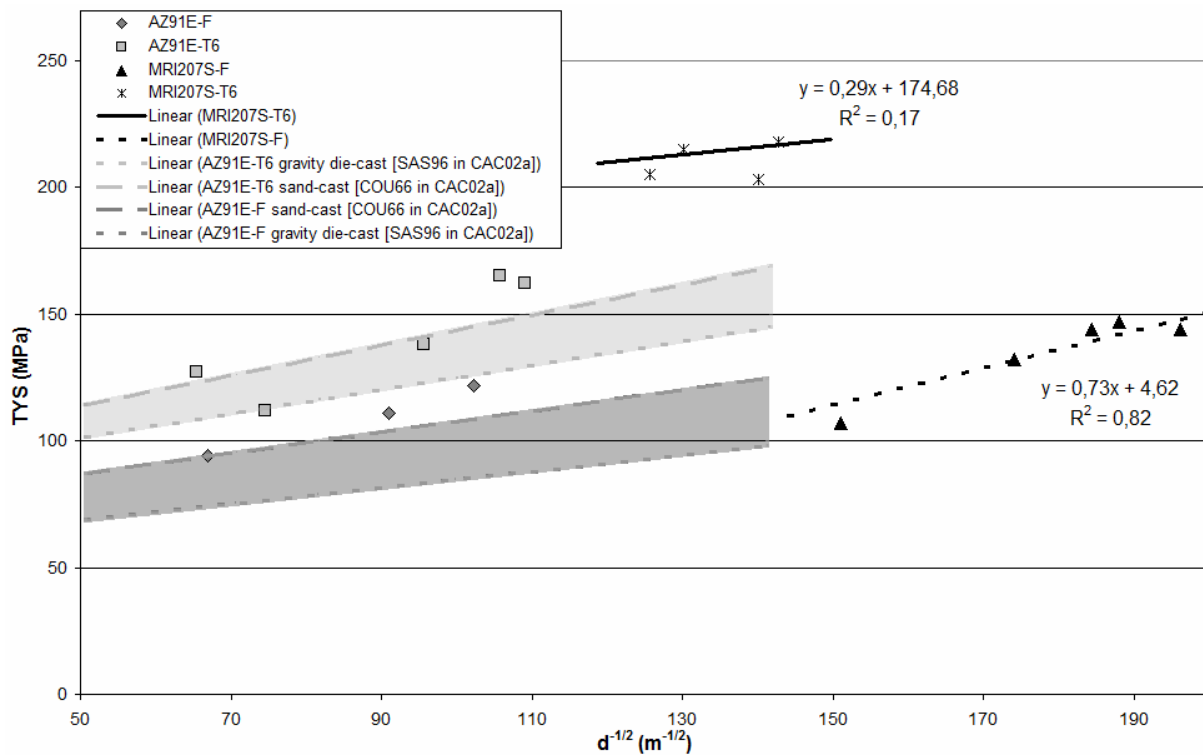


Figure 7.5. The 0.2% proof stress (TYS) as a function of  $d^{-1/2}$  for AZ91E and MRI207S alloys in as-cast and T6 conditions. Tendencies taken from literature [COU66 and SAS96 in CAC02a] are marked for AZ91E and tendency lines for MRI207S are illustrated.

A good correlation of the measured values of AZ91E and the literature is found and the dispersion of values is acceptable. This dispersion relates to the fact that the process parameters used in the literature and the ones employed in this work may differ. Moreover, the grain size measurement using linear intercept method always entails a measuring error. With regard to the MRI207S alloy, the lack of points for the new alloy makes it difficult to assure the right values of the tendencies. More markedly in the T6 condition, there is a lack of enough different grain sizes, because all the values obtained are close to each other. The abnormal grain growth which occurred in sand-cast test parts and is discussed in chapter 5, decreases the amount of available data. Even these values should be used with precaution, the estimated correlations are summarised in Table 7.7. In order to obtain better correlations, MRI207S should not only be analysed changing the solidification times, but also applying different amounts of grain refiners.

Table 7.7. Hall-Petch parameters for the 0.2% proof stress for the MRI207S alloy.

Alloy	$\sigma_0$ (MPa)	$k$ (MPa $m^{-1/2}$ )
MRI207S-F	5	0.73
MRI207S-T6	175	0.29

### 7.3 Correlation between solidification times and mechanical properties

In order to directly relate the mechanical properties with solidification curves, the relationships obtained between the grain size and the solidification times are integrated in the Hall-Petch equation. Therefore, the equations summarised in Table 7.8 for the prediction of mechanical properties from the

solidification times are proposed for the AZ91E and MRI207S alloys in as-cast and T6 heat-treated conditions.

*Table 7.8. Equations relating the solidification time with the tensile yield strength.*

Sand-cast AZ91E-F	$\sigma_{yAZ91E-F_{sand}} = 66 + 0.42(46.2t_s^{0.18})^{-1/2}$
Gravity die-cast AZ91E-F	$\sigma_{yAZ91E-F_{grav.}} = 53 + 0.32(46.2t_s^{0.18})^{-1/2}$
Sand-cast AZ91E-T6	$\sigma_{yAZ91E-T6_{sand}} = 84 + 0.6(46.2t_s^{0.18})^{-1/2}$
Gravity die-cast AZ91E-T6	$\sigma_{yAZ91E-T6_{grav.}} = 77 + 0.48(46.2t_s^{0.18})^{-1/2}$
MRI207S-F	$\sigma_{yMRI207S-F} = 5 + 0.73(5.4t_s^{0.59})^{-1/2}$
MRI207S-T6	$\sigma_{yMRI207S-T6} = 175 + 0.29(5.4t_s^{0.59})^{-1/2}$

The constants of the above equations (Table 7.8) are coherent. When the solidification time is increased, the tensile yield strength decreases, which is logical due to an increase in grain size.

These equations serve to predict directly the tensile yield strength from the solidification times. The solidification times can be predicted using commercial simulation tools and with the application of the above equations.

#### 7.4 Conclusions

The establishment of correlations between solidification times and tensile yield strength was achieved.

Firstly, correlations between solidification time and microstructure are defined in this chapter. A good coherency of results is obtained for the MRI207S alloy. AZ91E alloy shows a high dispersion of the results, which can be due to the differences in the utilised casting procedure. Nevertheless, the tendency of the curve is in accordance with the literature.

Hall-Petch parameters for the prediction of the tensile yield strength are also proposed. A good correlation is found between the measured values for the AZ91E alloy and the data from literature. Conversely, the values obtained for MRI207 are lacking in statistics. However, the presented values give coherent tendencies. To obtain more accurate values, it is advised to vary the amount of grain refiner in order to obtain values with enough different grain sizes.

Finally, solidification times and tensile yield strength are related. The equations relating them are easy to use and the obtained correlations can be integrated in simulation tools for the prediction of TYS. This kind of equation describes correctly the behaviour of the material.

For future trends, as explained in the conclusions of chapter 6, it is suggested to integrate the microhardness of the matrix to the solidification rate, grain size and mechanical properties. The microhardness of the matrix gives an idea of the formed precipitates and it can be the method to quantify and characterise the precipitation in a material. It is a variable easy to measure and it gives information about the kind of precipitates inside the matrix, and consequently, along the microstructure.



## **CHAPTER 8 - SUMMARY AND CONCLUSIONS**



## 8 SUMMARY AND CONCLUSIONS

The present work leads to a better understanding of the relationship between solidification conditions, microstructures and mechanical properties of magnesium cast alloys. The relationships established in this work can be integrated into the numerical simulation of the casting process. The relationships for a new magnesium alloy in as-cast and T6 heat-treat condition were established. This alloy is a newly developed magnesium alloy by MRI, named MRI207S. This will allow for an optimum design of the filling and gating systems in order to obtain the desired mechanical properties. It will also make possible to optimise the geometry of a part avoiding oversized areas, which can only be achieved if the prediction of local mechanical properties is accurate. The results obtained in this thesis will allow this optimisation of the design of the components.

The solidification of four magnesium alloys in four casting technologies is analysed in this work. Furthermore, the microstructure of the castings is characterised and tensile properties determined. Finally, correlations between them are established for the prediction of tensile yield strength.

The texture generation in HPDC is also analysed, for the first time, in order to identify the effect of the alloying elements on deformation mechanisms. It is shown that the alloying elements did not influence the texture creation under uniaxial deformation in the analysed HPDC alloys.

Newly developed alloys with improved strength are compared to commercially used magnesium alloys and to the A357 aluminium alloy. The objective of the new alloys is to have mechanical properties approximate to the values of aluminium alloys. This is achieved with the new MRI207S alloy, which is a promising candidate for the substitution of aluminium in aircrafts.

This work is divided into four principal tasks, and the main results obtained in each of them are summarised below:

### 1. Casting of tensile samples and test parts. Acquisition of cooling curves.

Several parts were cast in this research work and casting parameters were optimised in order to obtain acceptable castings. The influence of the filling time has proved to be essential for avoiding misruns. When the filling time is reduced, filling problems disappear. The importance of grain refiners in the AZ91E alloy is essential to obtain a fine grained microstructure and a continuous precipitation of  $\gamma$ -Al<sub>12</sub>Mg<sub>17</sub> phase. Finally, the influence of temperature to avoid surface and internal oxidation in investment casting is confirmed.

The parts cast in this task have a variety of microstructures depending on the local solidification rate. Cooling curves are acquired for the calculation of the solidification rate. The result is a variety of castings with different microstructures and mechanical properties with registered cooling curves.

## 2. Microstructural characterisation and texture evolution in Mg-alloys.

In order to determine the effect of the precipitates and grain size, microstructures in as-cast and heat treated conditions are characterised by optical microscopy and Scanning Electron Microscopy (SEM).  $\gamma\text{-Al}_{12}\text{Mg}_{17}$  phase is found to be the most important precipitate in Mg-Al alloys. Mg-Al alloys have a two-phase eutectic, consisting of  $\alpha\text{-Mg}$  and  $\gamma\text{-Al}_{12}\text{Mg}_{17}$ . The eutectic can appear in several morphologies. In as-cast condition, it usually appears as divorced or semi-divorced eutectic, while after T6 heat treatment it transforms into a pearlitic structure. MRI207S alloy presents an  $\alpha\text{-Mg}$  matrix with an eutectic  $(\text{Gd,Nd})\text{Mg}_3$  intermetallic. These precipitates form a fine precipitation in the matrix after T6 heat-treatment and are responsible for the precipitation strengthening.

Grain size and porosity are measured to obtain a correlation between grain size and the previously measured solidification curves. The porosity level in HPDC test parts is high (around 5-10%) and thus, the mechanical properties are low. Other technologies obtain acceptable porosity levels.

Fractography analysis is performed to characterise the effect of the alloy and heat treatment on the fracture. HPDC alloys show a dimple fracture surface, and a cleavage fracture is mainly observed in gravity casting alloys.

The texture formation during uniaxial deformation in two HPDC magnesium alloys is analysed during this work in order to determine the influence of the initial texture and the effect of the alloying elements on the final texture. Samples are deformed uniaxially by tensile testing. Texture generation, during tensile testing, is in accordance with that observed in wrought magnesium alloys. The (0001) basal plane is oriented parallel to the loading direction, as has already been described for wrought alloys. The difference is that the intensity obtained is lower in HPDC alloys than in wrought alloys. Contrary to wrought alloys, there is not a preferred orientation before testing in HPDC. The inhomogeneous microstructure of HPDC samples can also cause this lower intensity. With regard to the influence of alloying elements, the two alloys analysed have a similar texture after deformation. Hence, it is concluded that alloying elements do not influence the generation of the texture.

## 3. Mechanical characterisation.

The tensile properties are related to the microstructure. Samples cast by different technologies and geometries are characterised in this subject.

Newly developed alloys (MRI207S and AM50+Si+Sn alloys) show higher mechanical properties compared to AZ91 and AM50 commercial alloys. These higher properties can be attributed to the presence of precipitates containing Si and Sn in the AM50+Si+Sn alloy. In the case of MRI207S, aluminium is completely removed and more stable precipitates are formed. These precipitates increase precipitation strengthening after T6 heat treatment. Yield strength is considerably improved in this alloy compared to AZ91E.



Hardness measurements, on the other hand, lead to the establishment of correlations between hardness and microstructures. In this study the hardness of the precipitates is analysed, specifically the influence of the lamellar spacing of  $\alpha$ -Mg/ $\gamma$ -Al<sub>12</sub>Mg<sub>17</sub>. When the distance between the layers decreases, the hardness of the structure increases. The increase of hardness in this alloy can lead to a premature fracture of the eutectic structure. The reason for this is the brittle behaviour of the  $\gamma$ -Al<sub>12</sub>Mg<sub>17</sub> phase, which in closer lamellar spacing of the pearlitic structure decreases the ductility.

#### **4. Correlation between solidification curves, microstructures and mechanical properties**

Finally, correlations between solidification times, microstructures and mechanical properties are established. On one hand, constants correlating solidification time with grain size are established. On the other hand, Hall-Petch parameters are established in order to relate the grain size to the tensile yield strength. The values obtained in AZ91E are compared to the relations established in literature. Correlations are found for MRI207S alloy in as-cast and T6 heat treated conditions. The influence of second phases is not explicitly integrated in those correlations, leaving this task for future works.

In summary, correlations between solidification time, grain size and tensile yield strength are established for a newly developed magnesium alloy in as-cast and T6 (solution heat treated and artificially aged) conditions. The values of the commercial AZ91E alloy are verified with literature and they are acceptable. Therefore, the procedure is validated and the values of the new alloy established.

The correlations that are currently used do not take into account the existence of several phases, and they are based on the grain size, i.e. Hall-Petch relationship. The effect of the precipitates is not integrated into the defined correlations, but the problems have been identified, and future directions have been defined and explained. It is suggested that the correlation of the microhardness of the matrix with solidification time, grain size and tensile properties be performed in future works. However, the equations defined in this work are easy to apply in numerical casting models. Furthermore, the approximation obtained with such equations is usually enough for a good prediction of the properties obtained in reality.



## **CHAPTER 8 - SCIENTIFIC CONTRIBUTION**



## 9 SCIENTIFIC CONTRIBUTION

In this chapter the scientific contribution in conferences and journals is presented.

### 9.1 Publications in journals

Arruebarrena G., Hurtado I., Väinölä J., Cingi C., Dévényi S., Townsend J., Mahmood S., Wendt A., Weiss K., Ben-Dov A., "Development of Investment-Casting Process of Mg-Alloys for Aerospace Applications", *Advanced Engineering Materials*, 2007, v 9, No. 9, p. 751-756. Impact factor (2007): 1.463.

Sándor L., Arruebarrena G., Sándor B., "Magnéziumöntészeti kutatások - motiváció és első tapasztalatok a Fémalk Rt.-ben", *Bányászati és Kohászati Lapok, Kohászat*, 2006, v 139, issue 3, p. 19-23.

### 9.2 Publications and presentations in conferences

Wendt J., Kainer K.U., Arruebarrena G., Hantzsche K., Bohlen J., Letzig D., "On the Microstructure and Texture Development of Magnesium Alloy ZEK100 During Rolling", *Magnesium Technology, TMS 2009 Annual Meeting & Exhibition*, San Francisco, California, USA, February 2009. Paper and presentation.

Ulacia I., Arruebarrena G., Hurtado I., Spalthoff P., Randau C., "Neutron Diffraction Measurements of AZ31B Magnesium Alloy Sheet Biaxially Deformed at Warm Temperature", *8th German Neutron Scattering Conference*, Garching, Germany, September 2008. Poster.

Arruebarrena G., Hurtado I., Sarriegi H., Herrero-Dorca N., Gorosarri A., Weiss K., Rodríguez P.P., Oyarbide M., "Análisis de Microestructuras y Propiedades Mecánicas en Aleaciones de Mg Coladas a la Cera Perdida", *X Congreso Nacional de Materiales*, Donostia-San Sebastian, Spain, June 2008, p. 121-124. Paper and presentation.

Herrero Dorca N., Gorosarri A., Arruebarrena G., Rodríguez P.P., Oyarbide M., Hurtado I., "Simulación y Experimentación del Proceso de Microfusión para la Aleación de Magnesio AZ91E", *X Congreso Nacional de Materiales*, Donostia-San Sebastian, Spain, June 2008, p. 215-218. Paper and poster.

Arruebarrena G., Hurtado I., Väinölä J., Dévényi S., Townsend J., Mahmood S., Wendt A., Weiss K., Ben-Dov A., Schröder A., Pinkernelle A., "Development of an Investment-Casting Process of Mg-Alloys for Aerospace Applications", *7th International Conference on Magnesium Alloys and their Applications*, Dresden, Germany, November 2006, p. 228-233. Paper and presentation (Highlight mention).

Weiss K., Wendt A., Honsel Ch., Arruebarrena G., Hurtado I., Väinölä J., Mahmood S., Townsend J., Ben-Dov A., Schröder A., Pinkernelle A., "Modelling Microstructure and Mechanical Properties of thin-walled Magnesium castings", *7th International Conference on Magnesium Alloys and their Applications*, Dresden, Germany, November 2006, p. 165-172. Paper and presentation.

Abraham S., Bronfin B., Bamberger M., Arruebarrena G., "Microstructural Stability of Magnesium Alloys for Aerospace Applications", *7th International Conference on Magnesium Alloys and their Applications*, Dresden, Germany, November 2006, p. 473-479. Paper and presentation.

Ramati S., Wendt A., Weiss K., Townsend J., Bamberger M. Lukacs S., Bronfin B., Arruebarrena G., Väinölä J., Juers C., "Magnesium Castings for Aeroplanes", *Aeronautics Days 2006*, Vienna, Austria, June 2006. Abstract of a Parallel Session.

Arruebarrena G., Hurtado I., Arrieta X, Wendt A., Schröder A., Pinkernelle A., "Efecto de la Microestructura en las Propiedades Mecánicas de las Aleaciones de Magnesio", *IX. Congreso Nacional de Materiales*, Vigo, Spain, June 2006, p. 20-22. Paper and presentation.

Wendt A., Honsel Ch., Weiss K., Arruebarrena G., Schröder A., Townsend J., Devenyi S., "Modelling Mechanical Properties of Magnesium Castings for Aircrafts", *Modelling of Casting, Welding, and Advanced Solidification Processes - XI, MCWASP*, Opio, France, May 2006, p. 717-724. Paper and poster.

Arruebarrena G., Hurtado I., Wendt A., Bronfin B., "Weight Reduction in Aircrafts by means of New Magnesium Castings", *Materials Lightweights or Ultralightweights, Materials Science & Technology MS&T'05*, Pittsburgh, USA, September 2005, p. 13-20. Paper and presentation.

Arruebarrena G., Hurtado I., "Influencia del Proceso de Fundición de Aleaciones de Mg aeronáuticas sobre sus Propiedades Mecánicas", *XVI Congreso Nacional de Ingeniería Mecánica*, León, Spain, December 2004. Paper and presentation.

Arruebarrena G., Hurtado I., "Desarrollo y Caracterización de Nuevas Aleaciones de Mg para su Aplicación en Aeronáutica", *VIII Congreso Nacional de Materiales*, Valencia, Spain, June 2004, p. 455-462. Paper and presentation.





## **CHAPTER 10 - REFERENCES**



## 10 REFERENCES

- [AGH98] Aghion E., Bronfin B., "Physical metallurgy of Magnesium alloy ingots and die castings", *Proc. of the 7th Int. Conf. Magnesium Alloys and Their Applications*, (Ed: by Mordike BL, Kainer KU), Werkstoff-Informationsgesellschaft mbH., 1998, p. 295-300.
- [AGH04] Aghion E., Eliezer D., "Magnesium Alloys: Science, Technology and Applications", *published by The Israeli Consortium for the Development of Magnesium Technology*, Haifa, Israel, 2004.
- [AGH08] Aghion E., Gueta Y., Moscovitch N., Bronfin B., "Effect of yttrium additions on the properties of grain-refined Mg-3%Nd alloy", *J. Mater. Sci.*, 2008, **v 43**, p. 4870-4875.
- [AGN05] Agnew S., Duygulu O., "Plastic anisotropy and the role of non-basal slip in magnesium alloy AZ31B", *Internal Journal of Plasticity, Plasticity of Multiphase Materials*, 2005, **v 21**, n6, p. 1161-1193.
- [AKH72] Akhtar A., Teghtsoonian E., *Phil. Mag.*, 1972, **v 25**, p. 897-916, cited in [BLA08].
- [ALU08] aluMATTER. "Materials Science & Engineering; Anisotropy; Representing Texture" <http://aluminium.matter.org.uk/content/html/eng/default.asp?catid=100&pageid=1039432491>, [retrieved: 2008-09-15].
- [AND03] Andersson P., Cáceres C.H., Koike J., "Hall-Petch Parameters for Tension and Compression in Cast Mg", *Materials Science Forum*, 2003, **v 419-422**, p. 123-128.
- [ANY01a] Anyanwu I.A., Kamado S., Kojima Y., *Mater Trans JIM*, 2001, **v 42**, p. 1206, cited in [HON07].
- [ANY01b] Anyanwu I.A., Kamado S., Kojima Y., *Mater Trans JIM*, 2001, **v 42**, p. 1212, cited in [HON07].
- [ARM68] Armstrong R.W., *Acta Metall.*, 1968, **v 2**, p. 9-10, cited in [BLA08]
- [ARM83] Armstrong R.W., "Yield, flow and fracture of polycrystals", *ed. by T.N. Baker, Applied Science Publishers, London*, 1981, p. 1-31, cited in [AND03] and [BLA08].
- [ARR07] Arruebarrena G., Hurtado I., Väinölä J., Cingi C., Dévényi S., Townsend J., Mahmood S., Wendt A., Weiss K., Ben-Dov A., "Development of Investment-Casting Process of Mg-Alloys for Aerospace Applications", *Advanced Engineering Materials*, 2007, **v 9**, No. 9, p. 751-756.
- [ASM85] ASM International, "ASM Handbook Volume 09: Metallography and Microstructures", *Published by ASM International, Materials Park, Ohio*, 1985 (first printing).
- [ASM86] ASM International, "ASM Handbook Volume 10: Materials Characterization", *Published by ASM International, Materials Park, Ohio*, 1986 (first printing).

- [ASM87] ASM International, "ASM Handbook Volume 12: Fractography", *Published by ASM International*, Materials Park, Ohio, 1987 (first printing).
- [ASM88] ASM International, "ASM Handbook Volume 15: Casting", *Published by ASM International*, Materials Park, Ohio, 1988 (first printing).
- [AST96] ASTM, "E-112: Standard Test Method for Determining Average Grain Size", *Annual Book of ASTM Standards*, 1996, **v 03.01**.
- [AST03] ASTM, "E8M-03: Standard Test Methods for Tension Testing of Metallic Materials [Metric]", *Annual Book of ASTM Standards*, 2003, **v 01.02**.
- [AVE99] Avedesian M.M., Baker H., *ASM SPECIALTY HANDBOOK, Magnesium and Magnesium Alloys*, Ed. Avedesian, M.M. and Baker, H., Materials Park, OH, 1999.
- [AVR07] Avraham S., Bronfin B., Arruebarrena G., Bamberger M., "Microstructural Stability of Magnesium Alloys for Aerospace Applications", *Proc. of the 7th Int. Conf. Mg Alloys and their Applications* (Ed: K.U. Kainer), WILEY-VCH, Weinheim, 2007, p. 473-479.
- [BAC04] Bach F.W., Karger A., Pelz Ch., "Environmental Friendly Protection System for Molten Magnesium", *Proc. of the 6th Int. Conf. Mg Alloys and their Applications* (Ed: K.U. Kainer), WILEY-VCH, Weinheim, 2004, p. 1001-1005.
- [BEN08] Benedyk J.C., "Magnesium: Where Have We Been, Where Are We Going? A 65 Year Retrospective on the Use of Magnesium", *introductory article in the cd Magnesium Article Archive, May 1943 - June 2008, Light Metal Age*, 2008.
- [BLA08] Blake A.H., Cáceres C.H., "Solid-solution hardening and softening in Mg-Zn alloys", *Materials Science and Engineering A*, 2008, **v 483-484**, p. 161-163.
- [BRO07] Bronfin B., Ben-Dov A., Townsend J., Mahmood S., Vainola J., Deveneyi S., Moscovitch N., "Advanced Gravity Casting Magnesium Alloys for the Aircraft Industry", *Proc. of the 7th Int. Conf. Mg Alloys and their Applications* (Ed: K.U. Kainer), WILEY-VCH, Weinheim, 2007, p.14-19.
- [BRU08] Bruker AXS, "An Overview of XRF Basics. Fundamental Principles. Diffraction in crystals", [www.bruker-axs.de/fileadmin/user\\_upload/xrfintro/sec1\\_8.html](http://www.bruker-axs.de/fileadmin/user_upload/xrfintro/sec1_8.html), [retrieved: 2008-09-11].
- [BUN89] Bunge H.J., "Advantages of Neutron Diffraction in Texture Analysis", *Textures and Microstructures*, 1989, **v 10**, p. 265-307.
- [BUN93] Bunge H.J., "Texture analysis in materials science", *Cuvillier-Verlag*, Göttingen, 1993, cited in [YI05].
- [BUS45] Busk R.S., Phillips C.W., *Trans AIME*, 1945, **v 161**, p. 266-277.

- [BUS87] Busk R.S., "Magnesium Products Design", *Ed. Marcel Dekker*, NY, 1987, cited in [CAR97].
- [CAC02a] Cáceres C.H., Davidson C.J., Griffiths J.R., Newton C.L., "Effects of solidification rate and ageing on the microstructure and mechanical properties of AZ91 alloy", *Materials Science and Engineering A*, 2002, **v 325**, p. 344–355.
- [CAC02b] Cáceres C.H., Blake A., "The Strength of Concentrated Mg-Zn Solid Solutions", *phys. stat. sol. (a)*, 2002, **v 194**, No. 1, p. 147-158.
- [CAC??] Cáceres C.H., Blake A., Lukác P., *in preparation*, cited in [BLA08].
- [CAO04] Cao H., Wessén M., "Effect of Microstructure on Mechanical Properties of As-Cast Mg-Al Alloys", *Metallurgical and Materials Transactions A*, 2004, **v 35A**, p. 309-319.
- [CAR97] Carlson B.E., "Influence of Processing Variables and Aluminum Content on the Microstructure and Mechanical Properties of Cast Mg-Al Alloys", PhD dissertation, University of Michigan, 1997.
- [CAS04] Cashion S., Ricketts N., Bailey R., "Industrial Application of the AMCover Cover Gas System for Magnesium Melt Protection", *Proc. of the 6th Int. Conf. Mg Alloys and their Applications* (Ed: K.U. Kainer), WILEY-VCH, Weinheim, 2004, p. 995-1000.
- [CHA54] Chalmers B., *Trans. AIME*, 1954, **v 200**, p. 519-32, cited in [PET89].
- [CHA62] Chapman J.A., Wilson D.U., "Room-Temperature Ductility of Fine-Grain Magnesium", *Bull. J. Inst. Met.*, 1962, **v 91**, p. 39, cited in [EML66]
- [CHA64] Chalmers B., "Principles of Solidification", *John Wiley & Sons, Inc.*, New York, NY, 1964, p. 116-20, cited in [FLE74] and [PET89].
- [CIN06] Cingi C., "Mold-Metal Reactions in Magnesium Investment Castings", *PhD dissertation*, Helsinki University of Technology, Espoo, 2006.
- [COM05] Commission of the European Communities, "Communication from the Commission to the Council, the European Parliament, the European Economic and Social Committee and the Committee of the Regions", Brussels, COM(2005) 459 final, 2005, <http://eur-lex.europa.eu/LexUriServ/LexUriServ.do?uri=COM:2005:0459:FIN:EN:PDF> [retrieved: 2008-08-29].
- [COM06] Commission of the European Communities, "Commission Staff Working Document. Summary of the Impact Assessment: Inclusion of Aviation in the EU Greenhouse Gas Emissions Trading Scheme (EU ETS)", Brussels, SEC(2006) 1685, 2006, [http://ec.europa.eu/environment/climat/pdf/aviation/sec\\_2006\\_1685\\_en.pdf](http://ec.europa.eu/environment/climat/pdf/aviation/sec_2006_1685_en.pdf) [retrieved: 2008-08-29].
- [COU66] Couture A., Meier J.W., *AFS Trans.*, 1966, **v 74**, p. 164, cited in [CAC02].

- [DSM08] Dead Sea Magnesium, "Mg Casting Alloy, 6 kg ingot. Typical application: Diecasting", [www.dsmag.co.il/objects/Mg%20Alloy%206%20kg%20Ingot.pdf](http://www.dsmag.co.il/objects/Mg%20Alloy%206%20kg%20Ingot.pdf), [retrieved: 2008-07-16].
- [DUB98] Dubé D., Couture A., Carbonneau Y., Fiset M., Angers R., Tremblay R., *Int. J. Cast Metals Res.*, 1998, **v 11**, p. 139, cited in [CAC02a].
- [DUY03] Duygulu O., Agnew R., "The effect of temperature and strain rate on the tensile properties of textured magnesium alloy AZ31B sheet", *Magnesium Technology 2003* (Ed: Howard I. Kaplan) *TMS (The Minerals, Metals & Materials Society)*, 2003, p. 237-242.
- [EDI75] Edington J.W., "Practical Electron Microscopy in Materials Science. Monograph Two: Electron Diffraction in the Electron Microscope", THE *MACMILLAN PRESS LTD*, London and Basingstoke, 1975.
- [EML66] Emley, E.F., "Principles of Magnesium Technology", *Pergamon Press*, London, 1966.
- [EPA06] EPA (U.S. Environmental Protection Agency), "SF<sub>6</sub> Emission Reduction Partnership for Electric Power Systems. 2006 Annual Report", [www.epa.gov/electricpower-sf6/documents/sf6\\_2006\\_ann\\_report.pdf](http://www.epa.gov/electricpower-sf6/documents/sf6_2006_ann_report.pdf), [retrieved: 2008-08-11].
- [FER06] Ferreira A.F., da Silva A.J., de Castro, J., "Simulation of the solidification of pure nickel via the phase-field method", *Materials Research*, 2006, **v 9**, n 4, p 349-356.
- [FLE74] Flemings M.C., "Solidification Processing", *McGraw-Hill*, Inc., New York, NY, 1974, p. 134-174.
- [FOX43] Fox F.A., Lardner E., "An Investigation of the Effects of Precipitation Treatment of Binary Magnesium-Aluminium Alloys", *J. Inst. Met.*, 1943, **v 67**, p. 373-396.
- [FOX45] Fox F.A., "The Properties of Some Magnesium-Aluminium-Zinc Casting Alloys and the Incidence of Microporosity", *Journal of the Institute of Metals*, 1945, **v 71**, issue 1, p. 415-439.
- [FRM08] Forschungsneutronenquelle Heinz Maier-Leibnitz (FRM II), Stress-Spec Instrument, [www.frm2.tum.de/en/science/diffractometer/stress-spec/instrument/index.html](http://www.frm2.tum.de/en/science/diffractometer/stress-spec/instrument/index.html), [retrieved 2008-09-02].
- [GAR04] Gärtnerová V., Trojanová Z., Jäger A., Palček P., "Deformation behaviour of Mg-0.7 wt.% Nd alloy", *J. Alloys Compd.*, 2007, **v 427**, p. 115-123.
- [GEH05] Gehrman R., Frommert M.M., Gottstein G., "Texture effect on plastic deformation of magnesium", *Materials Science and Engineering A*, 2005, **v 395**, p. 338-349.
- [GIL04] Gill L., Lorimer G.W., Lyon P., "Microstructure/Property Relationship of Three Mg-RE-Zn-Zr Alloys", *Proc. of the 6th Int. Conf. Mg Alloys and their Applications* (Ed: K.U. Kainer), WILEY-VCH, Weinheim, 2004, p. 421-426.
- [HAL51] Hall E.O., *PROC. Phys. Soc. B*, 1951, **v 64**, p. 747, cited in [MAN04]

- [HAU56] Hauser F.E., Landon P.R., Dorn J.E., *AIME Trans.*, 1956, **v 206**, p. 589, cited in [AND03].
- [HER36] Herenguel J., Lacombe P., *Meteaux*, 1936, **v 11**, p. 185, cited in [EML66].
- [HON07] Honma T., Ohkubo T., Kamado S., Hono K., "Effect of Zn additions on the age-hardening of Mg-2.0Gd-1.2Y-0.2Zr alloys", *Acta Materialia*, 2007, **v 55**, p. 4137-4150.
- [HYD06] Hydro Magnesium, "Safety in Magnesium Die Casting", [www.hydomagnesium.com](http://www.hydomagnesium.com), [retrieved: 2006-12-07].
- [JAI07] Jain A., Agnew S.R., "Modeling the temperature dependence effect of twinning on the behaviour of magnesium alloy AZ31B sheet", *Materials Science and Engineering A*, 2007, **v 462**, p. 29-36.
- [JEN35] Jenkins C.H.M., Bucknall E.H., *J. Inst. Metals*, 1935, **v 57**, p. 141 cited in [FOX43], p. 151 cited in [EML66].
- [JIA07] Jiang L., Jonas J.J., Mishra R.K., Luo A.A., Sachdev A.K., Godet S., "Twinning and texture development in two Mg alloys subjected to loading along three different strain paths", *Acta Materialia*, 2007, **v 55**, p. 3899-3910.
- [KAI03] Kainer, K.U., "Magnesium Alloys and Technology", *Wiley-VCH Verlag GmbH & Co. KG aA*, Weinheim, Germany, 2003.
- [KAM87] Kamado S., Tsukuda M., Tokutomi I., Hirose K., *J Jpn Inst Light Met*, 1987, **v 37**, n.11, p. 714-720, cited in [CAR97].
- [KAW01] Kawamura Y., Hayashi K., Inoue A., Masumoto T., *Mater Trans JIM*, 2001, **v 42**, n7, p. 1172-1176, cited in [HON07]
- [KAT67] Kattamis T.Z., Coughlin J.C., Flemings M.C., *Trans AIME*, 1967, **v 239**, p. 1504-1511, cited in [CAR97].
- [KOC03] Koch T.A., Gharghoury M.A., "Fatigue properties of die-cast magnesium alloy AM60B", *Magnesium Technology 2003* (Ed: Howard I. Kaplan) *TMS (The Minerals, Metals & Materials Society)*, 2003, p 71-76.
- [KUR98] Kurz A., Fisher, D.J., "Fundamentals of Solidification", 4<sup>th</sup> revised ed., Trans Tech Publications Ltd., Aedermannsdorf, Switzerland, 1998.
- [LAB97] Labrecque C., Angers R., Tremblay R., Dubé D., *Can. Metall. Q.*, 1997, **v 36**, p. 169, cited in [CAC02a].
- [LEE00] Lee Y.C., Dahle A.K., St John, D.H., "The Role of Solute in Grain Refinement of Magnesium", *Metall. Mater. Trans. A, Phys. Metall. Mater. Sci. (USA)*, 2000, **v 31A**, issue 11, p. 2895-2905.

- [LI07] Li Q., Wang Q., Wang Y., Zeng X., Ding W., "Effect of Nd and Y addition on microstructure and mechanical properties of as-cast Mg-Zn-Zr alloy", *Journal of Alloys and Compounds*, 2007, **v 427**, p. 115-123.
- [LIU06] Liu Y., Wu X., "An Electron-Backscattered Diffraction Study of the Texture Evolution in a Coarse-Grained AZ31 Magnesium Alloy Deformed in Tension at Elevated Temperatures", *Metallurgical and Materials Transactions A*, 2007, **v 37A**, p. 7-17.
- [LUO94] Luo A, *Scripta Metall*, 1994, **v 31**, issue 9, p. 1253-1258, cited in [CAR97].
- [MAB00] Mabuchi M., Yamada Y., Shimojima K., Wen C.E., Chino Y., Nakamura M., Asahina T., Iwasaki H., Aizawa T., Higashi K., *Magnesium Alloys and Their Applications* (Ed. K.U. Kainer, Wiley-VCH, New York, 2000, p. 280-284, cited in [CAC02].
- [MAN04] Mann G., Griffiths J.R., Cáceres C.H., "Hall-Petch parameters in tension and compression in cast Mg-2Zn alloys", *Journal of Alloys and Compounds*, 2004, **v 378**, p. 188-191.
- [MUK97] Mukhina I.Y., Lebedev M., Kim K.H., Kim D.K., *Metal science and heat treatment*, 1997, **v 39**, n 5-6, p. 202-206, Translated from *Metallovedenie i termicheskaya obrabotka metallov*, Plenum Publishing, 1997, **v 5**, p. 21-25, cited in [GIL04].
- [NAV04] Nave M.D., Barnett M.R., "Microstructures and textures of pure magnesium deformed in plane-strain compression", *Scripta Materialia*, 2004, **v 51**, p. 881-885.
- [NUS89] Nussbaum B., Sainfort P., Regazzoni G., Gjestland H., *Scr Metall*, 1989, **v 23**, p. 1079-1084, cited in [CAC02] and [CAR97].
- [OST07] Ostrovsky I., Henn Y., "Present State and Future of Magnesium Application in Aerospace Industry", *proceedings of the New Challenges in Aeronautics Conference*, Moscow 2007, [www.magnesium-technologies.com/var/249/76510-PAPER%20-%20PRESENT%20STATE%20AND%20FUTURE%20OF%20MAGNESIUM%20APPLICATION%20IN%20AEROSPACE%20INDUSTRY.pdf](http://www.magnesium-technologies.com/var/249/76510-PAPER%20-%20PRESENT%20STATE%20AND%20FUTURE%20OF%20MAGNESIUM%20APPLICATION%20IN%20AEROSPACE%20INDUSTRY.pdf), [retrieved: 2008-09-02]
- [PEK03] Pekguleryuz M.O., Kaya A.A., "Creep resistant magnesium alloys for powertrain applications", *Advanced-Engineering-Materials*. 2003, **v 5**, n 12, p 866-878.
- [PEN08] Penghuai F., Liming P., Haiyan J., Jianwei C., Chunquan Z., "Effect of heat treatments on the microstructures and mechanical properties of Mg-3Nd-0.2Zn-0.4Zr (wt.%) alloy", *Materials Science and Engineering A*, 2008, **v 486**, p. 183-192.
- [PER04a] Pérez-Prado M.T., del Valle J.A., Ruano O.A., "Superplastic Behavior of a Fine Grained AZ61 Alloy Processed by Large Strain Hot Rolling", *Materials Science Forum*, 2004, **v 447-448**, p. 221-226.
- [PER04b] Pérez-Prado M.T., del Valle J.A., Contreras J.M., Ruano O.A., "Microstructural evolution during large strain hot rolling of an AM60 Mg alloy", *Scripta Materialia*, 2004, **v 50**, p. 661-665.



- [PET53] Petch N.J., *J. Iron Steel Inst. (London)*, 1953, **v 174**, p. 25, cited in [MAN04].
- [PET89] Pettersen K., Ryum N., "Crystallography of Directionally Solidified Magnesium Alloy AZ91", *Metallurgical Transactions A*, 1989, **v 20A**, p. 847-852.
- [PET90] Pettersen K., Lohne O., Ryum N., "Dendritic Solidification of Magnesium Alloy AZ91", *Metallurgical Transactions A*, 1990, **v 21A**, p. 221-230.
- [PFE07] Pfeiler W., "Alloy Physics. A Comprehensive Reference", 1<sup>st</sup> edition, Wiley-VCH, Weinheim, 2007.
- [PIK73] Pike T.J., Noble B., *J. Less-Common Met.*, 1973, **v 30**, p. 63, cited in [GAR04].
- [POR81] Porter D.A., Easterling K.E., "Phase Transformations in Metals and Alloys", *Published by Van Nostrand Reinhold (International) Co. Ltd.*, England, 1981.
- [RAO06] Rao J.C., Song M, Furuya K, Yoshimoto S, Yamasaki M, Kawamura Y, "TEM study of Mg-Zn precipitates in Mg-Zn-Y alloys", *J Mater Sci*, 2006, **v 41**, p. 2573-2576.
- [REE64] Reed-Hill R.E., "Physical Metallurgy Principles", *van Nostrand Company*, Princeton, NJ, 1964, p. 378-85, cited in [PET89].
- [REV08] Revankar V., Baker P., Schultz A.H., Brandt H., "A Replacement for SF<sub>6</sub>: The Magshield System", [www.hatch.ca/Light\\_Metals/Articles/Replacement\\_SF6\\_%20Magshield.pdf](http://www.hatch.ca/Light_Metals/Articles/Replacement_SF6_%20Magshield.pdf) [retrieved: 2008-08-11].
- [SAS96] Sasaki H., Adachi M., Sakamoto T., Takimoto A., *Proc. of the IMA-53, International Magnesium Association, June 2-4, Ube City, Yamaguchi, Japan*, 1996, p. 86-92, cited in [CAC02].
- [SCH68] Schäfer D., "Die Anwendung des Zuverlässigkeitskriteriums für Polfiguren kubischer Metalle", *Kristall u. Technik*, 1968, **3**, p. 473-476, cited in [BUN89].
- [SEQ97] Sequeira W.P., Murray M.T., Dunlop G.L., StJohn D.H., *Proc. TMS Symposium on automotive alloys*, (February 9–13, Orlando, FA.), The Minerals Metals and Materials Society (TMS), Warrendale, PA, 1997, p. 169–183, cited in [CAC02a].
- [SEQ04] Sequeira W., Dunlop G., "Microstructure, mechanical properties and fractography of high pressure die cast magnesium alloy AZ91D", *Die-Casting-Engineer*. 2004, **v 48**, n 2, p 62-74.
- [SOM06] Somekawa H., Mukai T., "Fracture toughness in a rolled AZ31 magnesium alloy", *Journal of Alloys and Compounds*, 2006, **v 417**, p. 209-213.
- [STA01] Stalman A., Sebastian W., Friedrich H., Schumann S., "Properties and Processing of Magnesium Wrought Products for Automotive Applications", *Advanced-Engineering-Materials* . 2001, **v 3**, n 12, p. 969-974.

- [STA03] Staroselsky A., Anand L., "A constitutive model for hcp materials deforming by slip and twinning: application to magnesium alloy AZ31B", *International Journal of Plasticity*, 2003, **v 19**, p. 1843-1864.
- [STJ03] StJohn D.H., Dahle A.K., Abbott T., Nave M.D., Qian M., "Solidification of cast magnesium alloys", *Magnesium Technology 2003* (Ed: Howard I. Kaplan) *TMS (The Minerals, Metals & Materials Society)*, 2003, p 95-100.
- [STR35] Straumanis M., *Z. Phys. Chem.*, 1935, **v 30**, p. 132-138, cited in [PET90].
- [SUZ03] Suzuki M., Kimura T., Koike J., Maruyama K., "Strengthening effect of Zn in heat resistant Mg-Y-Zn solid solution alloys", *Scripta Materialia*, 2003, **v 48**, p. 997-1002.
- [SWI04] Swift G.A., "Neutron Diffraction Study of *In Situ*-Reinforced Silicon Nitride during Creep", *PhD dissertation*, California Institute of Technology, Pasadena, California, 2004.
- [TAY38] Taylor, G., "Plastic Strain in Metals", *J. Inst. Met.*, 1928, **v 62**, p. 307-338, cited in [AGN05]
- [TEN80] Tenckhoff E., "Verformungsmechanismen Textur un Anisotropie in Zirkonium und Zirkaloy", *Gebrüder Borntraeger Berlin-Stuttgart*, 1980, cited in [YI05]
- [TEN92] Tensi H.M., Rosch R., "Unidirectional Solidification of the Mg-alloys AZ91hp and AM50hp with quenching of the solidification front", *DGM Conference on Magnesium Alloys and Their Applications*, Garmisch-Partenkirchen, Germany, 1992, p.283-289, cited in [CAR97].
- [TIK71] Tikhova N.M., Blokhina V.A., Antipova A.P., Vasil'eva T.P., Solov'eva G.G., *All union institute of aviation materials* Translated from *Metallovedenie I termicheskaya obrabotka metallov*, Plenum Publishing, 1971, **v 10**, p. 73-76, cited in [GIL04]
- [VAL03] del Valle J.A., Pérez-Prado M.T., Ruano O.A., "Microstructural Evolution During Hot Rolling of an AZ31 Mg Alloy", *Materials Science Forum*, 2003, **v 426-432**, p. 637-642.
- [VAN71] Van der Planken J., Deruyttere A., *J. Crys. Growth*, 1971, **v 11**, p. 273-279, cited in [PET90].
- [WAG06] Wagoner R.H., Lou X.Y., Li M., Agnew S.R., "Forming behavior of magnesium sheet", *Journal of Materials Processing Technology*, 2006, **v 177**, p. 483-485.
- [WAL03] Wallace J.F., Schwam D., Zhu Y., "The Influence of Potential Grain Refiners on Magnesium Foundry Alloys", *AFS Transactions*, 2003, **v 111**, p. 1061-1075.
- [WEI52] Weinberg F., Chalmers B., *Can. J. Phys.*, 1952, **v 30**, p. 488-502, cited in [PET89].
- [WEI97] Wei L.Y., Dunlop G.L., Westengen H., "Solidification behaviour and phase constituents of cast Mg-Zn-misch metal alloys", *J. Mater. Sci.*, 1997, **v 32**, p. 3335-3340.

- [WEN05] Wendt A., Weiss K., Ben-Dov A., Bamberger M., Bronfin B., "Magnesium castings in aeronautics applications - Special requirements", *Magnesium Technology 2005, TMS annual meeting*, 2005, p. 269-273.
- [WEN06] Wendt A., Honsel Ch., Weiss K., Arruebarrena G., Schröder A., Townsend J., Devenyi S., "Modelling Mechanical Properties of Magnesium Castings for Aircrafts", *MCWASP, Modelling of Casting, Welding and Advanced Solidification Process-XI*, 2006, **v 2**, p. 717-724.
- [YAN04] Yan C., Ye L., Mai Y.W., "Effect of constraint on tensile behavior of an AZ91 magnesium alloy", *Materials-Letters*. 2004, **v 58**, n 25, p 3219-3221.
- [YAN08] Yang J., Jianli W., Lidong W., Wu Y., Wang L., Hongjie Z., "Microstructure and mechanical properties of Mg-4.5-xNd (x=0, 1 and 2 wt%) alloys", *Materials Science and Engineering A*, 2008, **v 479**, p. 339-344.
- [YI05] Yi S.B., "Investigation on the Deformation Behavior and the Texture Evolution in Magnesium Wrought Alloy AZ31", *PhD dissertation*, Fakultät für Natur- und Materialwissenschaften der Technischen Universität Clausthal, Clausthal, Germany, 2005.
- [YI06] Yi S.B., Zaefferer S., Brokmeier H.-G., "Mechanical behaviour and microstructural evolution of magnesium alloy AZ31 in tension at different temperatures", *Materials Science and Engineering A*, 2006, **v 424**, p. 275-281.
- [YUE95] Yue T.M., Ha H.U., Musson N.J., "Grain size effects on the mechanical properties of some squeeze cast light alloys", *Journal of Materials Science*, 1995, **v 30**, n 9, p. 2277-2283.

